

New insights into structural changes of LiNiO₂

Zur Erlangung des akademischen Grades eines
DOKTORS DER NATURWISSENSCHAFTEN
(Dr. rer. nat.)

von der KIT-Fakultät für Chemie und Biowissenschaften
des Karlsruher Instituts für Technologie (KIT)

genehmigte

DISSERTATION

von
M. Sc. Hang Li

KIT-Dekan: Prof. Dr. Reinhard Fischer

Referent: Prof. Dr. Helmut Ehrenberg

Korreferent: Prof. Dr. Stefano Passerini

Tag der mündlichen Prüfung: 21.07.2022

Die vorliegende Arbeit wurde im Zeitraum vom 1. September 2019 bis 19. Juni 2022 am Institut für Anorganische Chemie der Fakultät für Chemie und Biowissenschaften am Karlsruher Institut für Technologie (KIT) unter der Leitung von Prof. Dr. Helmut Ehrenberg angefertigt.

Hiermit versichere ich, die vorliegende Arbeit selbstständig verfasst und keine anderen als die angegebenen Quellen und Hilfsmittel verwendet sowie Zitate kenntlich gemacht zu haben. Die Dissertation wurde bisher an keiner anderen Hochschule oder Universität eingereicht.

Karlsruhe

Anlage 5b

Versicherung gemäß § 13 Absatz 2 Satz 2 Ziffer 5 der Promotionsordnung des Karlsruher Instituts für Technologie (KIT) für die KIT-Fakultät für Chemie und Biowissenschaften

1. Einen erheblichen Verstoß gegen die Grundsätze guter wissenschaftlicher Praxis habe ich bislang nicht begangen.

2. Es gab bisher keine Promotionseignungsprüfung oder gleichwertige Prüfung an einer Universität oder dieser gleichgestellten Hochschule, an der ich erfolglos teilgenommen habe.

3. Diesem Promotionsverfahren gingen keine anderen Promotionsverfahren voran und ich bin in keinen weiteren Promotionsverfahren Kandidat/-in.

5. Ein entgeltliches Vertragsverhältnis, das eine gewerbliche Promotionsberatung zum Gegenstand hat und zur Unselbstständigkeit zumindest einer Promotionsleistung führen kann, besteht bzw. bestand nicht.

6. Die „Regeln zur Sicherung guter wissenschaftlicher Praxis am Karlsruher Institut für Technologie (KIT)“ habe ich beachtet.

7. In die Dissertation wurden Vorveröffentlichungen einbezogen, bei denen ich im Rahmen einer Mitautorenschaft jeweils einen signifikanten Teil selbstständig erbracht habe. Eine Aufstellung mit den Angaben:

Autoren/Autorinnen:

Titel der Vorveröffentlichung:

Veröffentlicht in:

Ausführliche Darlegung des selbstständig erbrachten, signifikanten Beitrages der Vorveröffentlichung oder der zur Veröffentlichung eingereichten Arbeit:

ist dieser Erklärung beigelegt. Die Aufstellung ist Bestandteil dieser Erklärung.

8. Die Dissertation oder Teile davon wurden nicht bei einer anderen Fakultät als Dissertation eingereicht.

9. Die Richtigkeit der vorstehenden Erklärungen bestätige ich.

Ort und Datum

Unterschrift

Manuscript 1 – (Results and Discussion in Chapter 3)

Authors: Hang Li, Weibo Hua, Xinyang Liu-Théato, Qiang Fu, Morgane Desmau, Alexander Missyul, Michael Knapp, Helmut Ehrenberg, Sylvio Indris

Publication title: New insights into lithium hopping and ordering in LiNiO₂ cathodes during Li (de)intercalation

Published in: *Chem. Mater.* **2021**, 33, 9546-9559

The co-authors listed in Table 1 were involved in the implementation and evaluation of some measurements.

Table 1: Statement of co-author contributions

co-authors	measurement method
Weibo Hua, Michael Knapp, and Alexander Missyul	<i>in situ</i> Synchrotron Radiation Diffraction
Morgane Desmau and Qiang Fu	<i>in situ</i> X-ray Absorption Spectroscopy
Xinyang Liu-Théato	Morphological Study by Scanning Electron Microscopy

Other co-authors:

Helmut Ehrenberg supervised the work and contributed to the completion of the manuscript.

Description of the contribution made independently:

Practical work:

This publication is based on investigations on LiNiO₂ cathodes during Li (de)intercalation. Material synthesis, battery assembly and galvanostatic cycling were all finished by myself. The extensive work on the investigation of structural variations was prepared and organized by me.

Measurements:

Galvanostatic intermittent titration technique measurement was conducted by me. *In situ* synchrotron radiation diffraction experiments were carried out by me, with the help of Weibo Hua, Michael Knapp, and Alexander Missyul. I performed all the Solid-state Nuclear Magnetic Resonance Spectroscopy measurements. Xinyang Liu-Théato carried out the Scanning Electron Microscopy experiment. Morgane Desmau and Qiang Fu conducted the *in situ* X-ray Absorption Spectroscopy measurement. Michael Knapp provided help for the Rietveld refinement. The evaluation and analysis of the measurements listed in Table 1 were coordinated by me and discussed together.

Creating the manuscript:

Essentially, I conceived the idea and wrote the manuscript. Qiang Fu (XPS) and Sylvio Indris (NMR) further contributed to my manuscript. Finally, the manuscript was finalized by Sylvio Indris, Michael Knapp, and Helmut Ehrenberg.

Manuscript 2 – (Results and Discussion in Chapter 4)

Authors: Hang Li, Weibo Hua, Björn Schwarz, Martin Etter, Stefan Mangold, Georgian Melinte, Nicola Pietro Maria Casati, Helmut Ehrenberg, Sylvio Indris

Publication title: Investigation of Structural and Electronic Changes Induced by Post-Synthesis Thermal Treatment of LiNiO₂

Published in: *Chem. Mater.* 2022 accepted

Table 2: Presentation of the co-author contributions

co-authors	measurement method
Weibo Hua, Nicola Pietro Maria Casati	<i>in situ</i> high-temperature Synchrotron Radiation Diffraction
Weibo Hua, Martin Etter	<i>ex situ</i> Synchrotron Radiation Diffraction
Stefan Mangold	<i>ex situ</i> X-ray Absorption Spectroscopy
Björn Schwarz	Magnetization Measurement
Georgian Melinte	Transition Electron Microscopy

Other co-authors:

H. Ehrenberg supervised the work and contributed to the completion of the manuscript.

Description of the contribution made independently:

Practical work:

This manuscript is based on the post-synthesis thermal treatment of LiNiO_2 . The thermal treatment was conducted by me, obtaining a series of samples. I finished the electrochemical characterization, including battery assembly and galvanostatic cycling. All other measurements were either carried out or organized and prepared by myself.

Measurements:

I selected the measurements so that a systematic investigation of the structure could be carried out on different time and length scales. *In situ* high-temperature Synchrotron Radiation Diffraction measurement was conducted by me, with the help of Weibo Hua, and Nicola Pietro Maria Casati. Weibo Hua, Martin Etter and I performed the *ex situ* synchrotron radiation diffraction. I performed the *ex situ* ^7Li Solid-state Nuclear Magnetic Resonance Spectroscopy measurements. Björn Schwarz carried out the magnetization measurement. Stefan Mangold conducted the *ex situ* X-ray absorption spectroscopy measurement. Georgian Melinte performed the transition electron microscopy measurement. Christina Odemer conducted the thermogravimetric analysis measurement. The evaluation and analysis of the measurements listed in Table 2 were coordinated by me and discussed together.

Creating the manuscript:

The framework of the manuscript was completed after in-depth discussion between me, Indris Sylvio, and Björn Schwarz. The manuscript was essentially written by me. Additional contributions are by Björn Schwarz (magnetization measurement), Sylvio Indris (Nuclear Magnetic Resonance Spectroscopy), and Georgian Melinte (transition electron microscopy).

Abstract

Nowadays, the electric automotive market requires an increase in the capacity of Li-ion batteries to allow longer driving ranges, and also faster charging capability. The requirement has fueled the development of Ni-rich $\text{LiNi}_{1-x-y}\text{Co}_x\text{Al}_y\text{O}_2$ (NCA) and $\text{LiNi}_{1-x-y}\text{Co}_x\text{Mn}_y\text{O}_2$ (NCM) cathode materials, in which the Ni content is beyond 80% (with respect to the overall transition metal content). Academia and industry have the same interest in enriching these materials in Ni, pushing the cathode systems toward LiNiO_2 . However, this effort is hindered by the trade-off between capacity and stability. Approaching LiNiO_2 (high Ni content) results in intrinsic stability issues from this classic layered material. Hence, there is huge interest in refocusing on LiNiO_2 , which has been investigated for almost three decades. Much of our understanding of the structure and property is based on excellent but relatively old studies. With the improvements in advanced characterization methods, fresh perspectives on poorly understood behaviors can be provided, and some theoretical assumptions have chances to be checked. Therefore, in this Ph.D. work, some new insights are provided, highlighting the Li/vacancy ordering structures and thermal stabilities at low temperatures. These new perspectives are believed to facilitate the understanding of remaining challenges, in the hope that they can be overcome someday. The thesis on the LiNiO_2 is organized in two sections as described below:

(I) *New insights into lithium hopping and ordering in LiNiO_2 during Li (de)intercalation.*

Ex situ ^6Li and *in situ* ^7Li nuclear magnetic resonance (NMR) spectroscopy is applied to monitor lithium mobility of LiNiO_2 during Li-ion (de)intercalation. Experimental NMR shifts are compared with the calculated shifts based on the theoretical Li/vacancy ordering models. The observed shifts are somehow close to estimated values. A considerable line broadening is first observed at a state of charge (SoC) of 20% (in this thesis, 100% belongs to the hypothetical full delithiation of the material). The movement of Li hopping slows down just before the ordering structure $\text{Li}_{0.75}\text{NiO}_2$ appears. This first Li/vacancy ordering structure can strengthen the Jahn-Teller effect, thus distorting the layered structure. The distortion further hinders the Li diffusion and broadens the NMR signal. For the last three SoC states (75%, 80%, and 85%), the NMR peaks remain at higher ppm positions. This suggests that the remaining Ni^{3+} is located

preferentially in the vicinity of the remaining Li ions, fitting well with the calculation model of $\text{Li}_{0.25}\text{NiO}_2$: each Li ion is surrounded by six Ni^{3+} with the 180° configuration ($\text{Li}_A\text{-O-Ni}^{3+}\text{-O-Li}_B$). Such a special Li-ordered and $\text{Ni}^{3+}/\text{Ni}^{4+}$ -ordered structure corresponds to the single H2 phase and appears to be the necessary preparation step for the H2 to the H3 phase transition. Galvanostatic intermittent titration (GITT) and *in situ* X-ray absorption spectroscopy (XAS) were also conducted to monitor changes in Li mobility and the oxidation state of Ni.

(II) Investigation of structural and electronic changes induced by post-synthesis thermal treatment of LiNiO_2

LiNiO_2 is investigated with respect to the subtle structural and electronic changes induced by a thermal treatment in air after synthesis in pure oxygen. These structure evolutions can also be regarded as the reflection of thermal instabilities of LiNiO_2 at low temperatures. A combination of thermogravimetry (TG), synchrotron radiation diffraction (SRD)/ X-ray absorption spectroscopy (XAS), ^7Li magic-angle spinning (MAS) NMR spectroscopy, magnetic measurements, and transmission electron microscopy (TEM) were applied to identify such subtle changes. These measurements reveal that Ni migration to the Li layers already starts at 200°C , later followed by reactions between LiNiO_2 and CO_2 . With the heat treatment temperature increasing, strongly off-stoichiometric $\text{Li}_{1-z}\text{Ni}_{1+z}\text{O}_2$ phases and products of Li_2CO_3 have been obtained. At 700°C , bulk decomposition occurs at a sluggish rate, suppressing the reactions with CO_2 . The decomposition corresponds to the increasing rate of Ni reduction and preference of Ni^{2+} for occupying the Ni sites. The extent of both reactions may not be homogeneous through the material, a larger reaction rate is instead found at the surface. The changes in Ni oxidation state and local Li environments are also monitored during the whole process. In addition, mild thermal treatment at $360\text{-}380^\circ\text{C}$ can improve the electrochemical performance of LiNiO_2 since a ferromagnetic cubic phase in the surface region can serve as a protection layer.

Zusammenfassung

Heutzutage erfordert der Markt für Elektroautos eine Erhöhung der Kapazität von Li-Ionen-Batterien, um größere Reichweiten zu ermöglichen. Diese Anforderung hat die Entwicklung von Ni-reichen $\text{LiNi}_{1-x-y}\text{Co}_x\text{Al}_y\text{O}_2$ (NCA) und $\text{LiNi}_{1-x-y}\text{Co}_x\text{Mn}_y\text{O}_2$ (NCM) Kathodenmaterialien vorangetrieben, in denen der Ni-Gehalt über 80% beträgt (in Bezug auf den Übergangsmetallgehalt). Wissenschaft und Industrie haben das gleiche Interesse daran, diese Materialien mit Ni anzureichern und die Kathodensysteme in Richtung LiNiO_2 zu treiben. Diese Bemühungen werden jedoch durch den Kompromiss zwischen Kapazität und Stabilität behindert. Die Annäherung an LiNiO_2 (hoher Ni-Gehalt) führt zu intrinsischen Stabilitätsproblemen dieser klassischen Schichtstruktur. Daher besteht großes Interesse, sich wieder auf LiNiO_2 zu konzentrieren, das seit fast drei Jahrzehnten erforscht wird. Ein Großteil unseres Verständnisses seiner Struktur und Eigenschaften basiert auf hervorragenden, aber relativ alten Studien. Mit den Verbesserungen bei fortschrittlichen Charakterisierungsmethoden können neue Perspektiven auf wenig verstandene Verhaltensweisen bereitgestellt werden, und einige theoretische Annahmen können so überprüft werden. In dieser Dissertation werden daher einige neue Erkenntnisse geliefert, die die Li/Fehlstellen-Ordnungsstrukturen und die thermische Stabilität bei niedrigen Temperaturen hervorheben. Es wird angenommen, dass diese neuen Perspektiven das Verständnis der verbleibenden Herausforderungen erleichtern werden, in der Hoffnung, dass sie eines Tages überwunden werden können. Diese Doktorarbeit zu LiNiO_2 gliedert sich wie folgt in zwei Abschnitte:

(I) Neue Einblicke in Lithium-Hopping und Ordnung in LiNiO_2 während der Li-(De)Interkalation.

Ex situ ^6Li und *in situ* ^7Li Kernspinresonanz (NMR)-Spektroskopie werden angewendet, um die Lithiummobilität von LiNiO_2 während der (De)Interkalation von Li-Ionen zu überwachen. Experimentelle NMR-Verschiebungen werden mit den berechneten Verschiebungen basierend auf den theoretischen Li/Leerstellen-Ordnungsmodellen verglichen. Die beobachteten Verschiebungen liegen nahe an berechneten Werten. Eine deutliche Linienverbreiterung ist erst bei einem Ladezustand (SoC) von 20 % zu beobachten. Die Li-Hüpfbewegung verlangsamt sich kurz bevor die geordnete $\text{Li}_{0.75}\text{NiO}_2$ -Struktur erscheint. Diese Struktur der ersten Li/Leerstellen-Ordnung kann den Jahn-Teller-Effekt verstärken und somit die Schichtstruktur verzerren. Die Verzerrung behindert die Li-Diffusion weiter und verbreitert das NMR-Signal. Für die letzten drei SoC-Zustände (75%, 80% und 85%) verbleiben die NMR-Peaks bei höheren

ppm-Positionen. Dies weist darauf hin, dass sich das verbleibende Ni^{3+} vorzugsweise in der Nähe der verbleibenden Li-Ionen befindet, was gut zum Rechenmodell von $\text{Li}_{0.25}\text{NiO}_2$ passt: Jedes Li-Ion ist umgeben von sechs Ni^{3+} mit der 180° -Konfiguration ($\text{Li}_A\text{-O-Ni}^{3+}\text{-O-Li}_B$). Eine solche spezielle Li/Leerstellen- und $\text{Ni}^{3+}/\text{Ni}^{4+}$ -geordnete Struktur entspricht der einzelnen H2-Phase und scheint der notwendige vorbereitende Schritt für den Übergang von der H2 in H3 Phase zu sein. Galvanostatische intermittierende Titration (GITT) und in-situ-Röntgenabsorptionsspektroskopie (XAS) wurden ebenfalls durchgeführt, um Änderungen der Li-Mobilität und des Ni-Oxidationszustands zu überwachen.

(II) Untersuchung struktureller und elektronischer Veränderungen, die durch die thermische Behandlung von LiNiO_2 nach der Synthese induziert werden

LiNiO_2 wird auf subtile strukturelle und elektronische Änderungen untersucht, die durch thermische Behandlung in Luft nach der Synthese in reinem Sauerstoff induziert werden. Diese Strukturentwicklungen können auch als Ausdruck der thermischen Instabilität von LiNiO_2 bei niedrigen Temperaturen angesehen werden. Eine Kombination aus Thermogravimetrie (TG), Synchrotronstrahlungsbeugung (SRD)/ Röntgenabsorptionsspektroskopie (XAS), ^7Li Magic Angle Spinning (MAS) NMR-Spektroskopie, magnetischen Messungen und Transmissionselektronenmikroskopie (TEM) werden angewendet, um solche subtilen Veränderungen zu identifizieren. Diese Messungen zeigen, dass die Ni-Migration in die Li-Schichten bereits bei 200°C beginnt, gefolgt von Reaktionen zwischen LiNiO_2 und CO_2 . Mit zunehmender Wärmebehandlungstemperatur wurden stark nichtstöchiometrische $\text{Li}_{1-z}\text{Ni}_{1+z}\text{O}_2$ -Phasen und Produkte von Li_2CO_3 erhalten. Bei 700°C ist die Zersetzung der Hauptphase langsam und unterdrückt Reaktionen mit CO_2 . Die Zersetzung entspricht der zunehmenden Geschwindigkeit der Ni-Reduktion und der Präferenz für Ni^{2+} , die Ni-Plätze zu besetzen. Das Ausmaß beider Reaktionen ist möglicherweise nicht im gesamten Material homogen, stattdessen wird an der Oberfläche eine größere Reaktionsgeschwindigkeit festgestellt. Die Änderungen des Ni-Oxidationszustands und der lokalen Li-Umgebungen werden ebenfalls während des gesamten Prozesses überwacht. Darüber hinaus kann eine milde Wärmebehandlung bei $360\text{-}380^\circ\text{C}$ die elektrochemischen Kenndaten von LiNiO_2 verbessern.

Acknowledgments

Time flies and seasons vary, almost three years have passed since I first arrived in Germany in 2019. A large number of scenes, including happiness, enjoyment, and achievability, make up this unforgettable experience in my life. During this short period, although novel coronavirus (2019-nCoV) and wars have influenced the world and normal life profoundly, we still manage to conduct the research with sheer delight. The study was performed at the Department of Chemistry and Biosciences (Karlsruhe Institute of Technology, KIT), Institute for Applied Materials - Energy Storage Systems (IAM-ESS). I received financial support from the China Scholarship Council (CSC, No. 201906200016). Many thanks go to people who kindly offered guidance and encouragement to me.

Firstly, I am grateful to my supervisor Prof. Dr. Helmut Ehrenberg, who gave me the opportunity to work in IAM-ESS, for his great support, valuable guidance, and thoughtful comments. I also want to thank Prof. Dr. Stefano Passerini for being my co-referee, Prof. Dr. Jan-Dierk Grunwaldt, and Prof. Dr. Annie Powell for being my examiners.

Next, I would like to express my sincere thanks and appreciation to my co-supervisor Dr. Sylvio Indris. He builds a relaxed environment in our group to perform the research. His encouragement, understanding, guidance, and personal character benefit me a lot. I really enjoy the time when we performed the NMR measurement together. I also cannot forget the experience that we went jogging after the synchrotron experiment in Hamburg and Villigen. It is really my fortune to work with him. I also wish to express my appreciation to Dr. Björn Schwarz for his kind support and help. His deep insights and strictness toward research inspire me a lot. Many thanks are also given to Dr. Weibo Hua, who was my colleague in the past and now works at Xi'an Jiaotong University. I am also grateful to Valeriu Mereacre and Liuda Mereacre for providing essential support in the lab.

I would like to express much thankfulness to Dr. Michael Knapp for his support and for giving useful comments on this thesis. The help from my colleagues at IAM-ESS, Dr. Qiang Fu, Dr. Xinyang Liu-Théato, Dr. Xianlin Luo, Lydia Gehrlein, Ahmad Ghamlouche, Anna Khudyshkina, Tianzhu Liu, Hannes Radinger, etc., are gratefully acknowledged. In addition, the kind assistance from former Chinese colleagues at IAM-ESS, Dr. Guiying Tian, Dr. Lihua Zhu, Dr. Zijian Zhao, Dr. Jiangong Zhu, Dr. Jiarong He, and Dr. Chengping Li, etc., are highly appreciated.

I would like to thank Dr. Martin Etter (P02.1 beamline at PETRA III, Hamburg), Dr. Nicola Pietro Maria Casati (MS beamline Paul Scherer Institute (PSI)), and Dr. Aleksandr Missiul (MSPD beamline at ALBA, Barcelona) for SRD experiments; Dr. Stefan Mangold (XAS beamline of the KIT Light Source (Karlsruhe)), and Dr. Morgane Desmau (P65 beamline at PETRA III, Hamburg) for the XAS measurements; Dr. Georgian Melinte (Karlsruhe Nano Micro Facility) for the TEM experiments, and Christina Odemer for Thermogravimetry (TG) measurements. All colleagues working on this topic in IAM-ESS are gratefully acknowledged for their support and help during this research.

Finally, I would like to thank my parents. During these three years of study abroad, it is a great regret for me that I cannot take good care of them. They always support and understand me throughout the whole period. It is their love that makes me live happily, not fearing any challenges and difficulties. May joy and health be with my dear mother and father always. I also wish to express my deep gratitude to my girlfriend. We create an incredible and shining life together in Germany, which will become our unforgettable memories in life.

Dedication

*To my parent Jinfeng Wang and Chunpeng Li
and my girlfriend Meijun Zhou
their company makes me realize my tremendous potential*

Content

Abstract.....	i
Zusammenfassung	iii
Acknowledgments	v
Dedication.....	vii
Content	viii
Symbols and Abbreviations.....	x
List of Figures.....	xi
List of Tables	xvii
Chapter 1 Introduction.....	1
1.1 Li-Ion Batteries	1
1.2 Fundamentals of Batteries	2
1.3 Intercalation Chemistry.....	3
1.4 The Crystal Chemistry of LiNiO ₂	5
1.5 The Structural Evolution during Cycling of LiNiO ₂	8
1.6 The Synthesis and decomposition of LiNiO ₂	11
1.7 Motivation and objectives of the thesis	14
Chapter 2 Solid State Nuclear Magnetic Resonance	15
2.1 The Basics of NMR	15
2.2 The Hahn-Echo	16
2.3 Magic Angle Spinning	17
2.4 Paramagnetic NMR.....	19
2.5 Fermi Contact Interaction	19
2.6 Bond Pathway Approach	20
Chapter 3 New Insights into Lithium Hopping and Ordering in LiNiO ₂ Cathodes	23
3.1 Introduction.....	23
3.2 Experimental.....	25
3.3 Results and discussion	30
3.3.1 Structural and morphological characterization	30
3.3.2 <i>In situ</i> XRD	34
3.3.3 <i>Ex situ</i> NMR.....	37
3.3.4 <i>In situ</i> NMR.....	49
3.3.5 <i>Ex situ</i> XAS.....	54

3.3.6 GITT.....	56
3.4 Conclusion	58
Chapter 4 Investigation of Structural and Electronic Changes Induced by Post-Synthesis Thermal Treatment of LiNiO ₂	59
4.1 Introduction.....	59
4.2 Experimental.....	61
4.3 Results and Discussion:	64
4.3.1 Electrochemical performance.....	66
4.3.2 <i>Ex situ</i> XRD	71
4.3.3 <i>In situ</i> high-temperature XRD.....	83
4.3.4 <i>Ex situ</i> NMR.....	87
4.3.5 <i>Ex situ</i> XAS.....	92
4.3.6 Magnetic measurements.....	94
4.3.7 TEM	105
4.4 Conclusion	112
Chapter 5 Conclusion and outlook	114
Reference	116
Publications	124

Symbols and Abbreviations

XRD	X-ray powder diffraction
SRD	Synchrotron radiation diffraction
SEM	Scanning electron microscopy
TEM	Transmission electron microscopy
XAS	X-ray absorption spectroscopy
EXAFS	Extended X-ray absorption fine structure
LIBs	Lithium-ion batteries
NMR	Nuclear magnetic resonance
MAS	Magic-angle spinning
SoC/D	State of charge/discharge
GITT	Galvanostatic intermittent titration
RF	Radio Frequency
FID	Free induction decay
CSA	Chemical shift anisotropy
JT	Jahn-Teller

List of Figures

Figure 1.1 Schematic open-circuit energy diagram of an electrolyte. $-e[E_{Reduction}]$ and $-e[E_{Oxidation}]$ are the reduction and oxidation energies of the electrolyte. E_g is the electrochemical stability window of the electrolyte. $\mu_{e^-, Anode}$ and $\mu_{e^-, Cathode}$ are the electrochemical potentials of anode and cathode, respectively. V_{oc} is the open-circuit voltage. Figure adopted from Hubert H. Girault et al.¹⁰ 3

Figure 1.2 Schematic diagram of intercalation of guest species into host structures via or solid-solution reaction or two-phase reaction. The corresponding response of the potential in the potential profile is also displayed. The newly formed second phase during a two-phase reaction can be ordered or disordered. 5

Figure 1.3 Illustration of crystal structures relevant to layered LiNiO_2 . They are labelled using the crystallographic family they belong to ((a) hexagonal and (b) monoclinic) and Delmas's notation (in brackets). The stacking sequences are indicated by labelling the oxygen planes. Unit cells are displayed in orange (hexagonal) and blue (monoclinic). Li, Ni, and O atoms are shown in yellow, light green, and red, respectively. 7

Figure 1.4 Contour maps of in situ synchrotron diffraction of LNO collected during the first cycle. (a) Cell voltage as a function of state of charge or discharge of the 1st cycle, which is aligned with the diffraction patterns; XRD patterns of selected scattering angle regions: (b) 4.68° - 5.48° , (c) 9.59° - 10.45° and (d) 11.36° - 12.26° . The phases in each region are labelled in (a). The peak splitting for phase M is also indicated in (c) and (d). Reprinted from my own publication.³¹ 9

Figure 1.5 Li/vacancy ordering structures with Li ions and vacancies labelled as yellow and grey spheres, respectively. Unit cells are outlined with solid black lines. Figure adapted from Mock.³⁶ ... 10

Figure 2.1 "Grapefruit" diagram displaying the evolution of the bulk magnetization M during a one-pulse NMR experiment. (a) the equilibrium magnetization M (red arrow) is aligned along the direction of the B_0 field z . (b) a $\pi/2$ pulse is applied along B_1 (x) and the magnetization is rotated into the xy -plane. (c) the Magnetization precesses in xy -plane (purple arrows) and this precessing magnetization induces a voltage signal in the RF coil. Adapted from reference.⁵⁴ 16

Figure 2.2 The magic-angle spinning experiment.⁵⁵ The sample is spun fast in a cylindrical rotor around a spinning axis orientated at the magic angle ($\theta_R = 54.74^\circ$) with respect to the applied magnetic field B_0 . The spin interaction tensor is represented by an ellipsoid and it is fixed with respect to the corresponding molecule/crystal and thus rotates with the sample. The angle is the angle between B_0 and the principal z -axis of the spin interaction tensor; β is the angle between the z -axis of the spin interaction tensor principal axis and the spinning axis. 18

Figure 2.3 (a) Illustration of the coordination environment of a Li in the Li layer in LiNiO_2 . There are 6 nearest cation neighbours (3 above and 3 below) which can transfer unpaired spin density to Li

via Ni-O-Li 90° bonds (sky blue arrows). There are 6 next nearest cation neighbours (3 above and 3 below) which can transfer unpaired spin density to Li via Ni-O-Li 180° bonds (dark blue arrows). **(b)** shows the view perpendicular to the layer. 21

Figure 3.1 (a) The Li-vacancy arrangements in $\text{Li}_{0.25}\text{NiO}_2$ (based on the theoretical model in Reference).⁶⁶ The yellow spheres denote the lithium orderings and the blue and red spheres represent Ni and O atoms, respectively. Three 180° $\text{Li}_A\text{-O-Ni}^{3+}\text{-O-Li}_B$ configurations are labelled by numbers on atoms from 1 to 5 (for example, Ni^{3+} located in the centre of the chain are denoted by number 3). **(b)** The view of 180° $\text{Li}_A\text{-O-Ni}^{3+}\text{-O-Li}_B$ configurations from a direction. 24

Figure 3.2 ²⁰⁷Pb MAS NMR spectra of $\text{Pb}(\text{NO}_3)_2$ as a function of spinning speed..... 27

Figure 3.3 (a) The voltage-time profile obtained from GITT on LNO/Li half-cells. **(b)** Voltage and current as a function of time for a typical pulse-rest step acquired during GITT. **(c)** Open circuit potential (U^0) of LNO as a function of Li content determined from GITT with several polynomial fits. **(d)** Derivative of equilibrium potential as a function of Li content, derived from GITT. **(e)** Voltage as a function of square root of time for a single pulse duration with the corresponding linear fit. R^2 is 0.99943 for this fit and for most of the fitting R^2 values are larger than 0.99. 29

Figure 3.4 SEM image of LiNiO_2 30

Figure 3.5 Rietveld refinement of LNO based on synchrotron diffraction pattern..... 31

Figure 3.6 (a) Voltage profiles for the first and second galvanostatic charge and discharge cycles of an LNO/Li half -cell and **(b)** the corresponding differential capacity (dQ/dV) plot with phase compositions being labelled. 33

Figure 3.7 The cycling performance of LNO half-cell at a rate of 0.5 C 33

Figure 3.8 Contour maps of in situ synchrotron diffraction of LNO collected during the first cycle. **(a)** Cell voltage as a function of state of charge or discharge of the 1st cycle, which is aligned with the diffraction patterns; XRD patterns of selected scattering angle regions: **(b)** 4.68°-5.48°, **(c)** 9.59°-10.45° and **(d)** 11.36°-12.26°. Based on the refinement results, the phases in each region are labelled in **(a)**. The peak splitting for phase M is also indicated in **(c)** and **(d)**. 34

Figure 3.9 (a) Lattice parameters a_h , b_m , $a_m/\sqrt{3}$ and **(b)** c_h , $3\sin\beta\text{-}c_m$ as a function of state of charge and discharge. The parameters belonging to the M phase are transformed to the hexagonal cell's system in order to evaluate the degree of distortion. 35

Figure 3.10 Illustration of the coordination environment of a Li-layer Li in LNO. There are 6 nearest cation neighbours which can transfer unpaired spin density to Li via Ni-O-Li 90° bonds. There are also 6 neighbouring cations which can transfer density via Ni-O-Li 180° bonds. 37

Figure 3.11 (a) STEM image of an LNO particle, **(b)** Ni L-edge chemical shift mapping of the green area in **(a)** and **(c)** corresponding EELS signals from different locations revealing a reduced oxidation state of Ni at the surface.³¹ 38

Figure 3.12 (a) Li/vacancy ordering schemes in Li_xNiO_2 at x values of 0.25, 0.33, 0.4, and 0.75. Only lithium and Ni^{3+} are shown without oxygen atoms and bonds. Models of $\text{Li}_{0.5}\text{NiO}_2$ and $\text{Li}_{0.6}\text{NiO}_2$ are shown in Table 3.2, 3.3. (b) Li layers of each composition with Li ordering along c axis direction. ³¹	39
Figure 3.13 Li/vacancy orderings in Li_xNiO_2 at x values of 0.60 (a)(b) and 0.50 (c)(d) . Oxygen atoms and bonds are not shown. In (a) and (c) the $\text{Ni}^{3.5+}$ ions are considered to be Ni^{3+} and in (b) and (d) the $\text{Ni}^{3.5+}$ ions are considered to be Ni^{4+} and are not shown in the figure. ³¹	40
Figure 3.14 Ex situ ^6Li MAS NMR spectra. Cell voltage as a function of state of charge and discharge for the first galvanostatic cycle of an LNO half-cell, dashed lines indicate points where cells were disassembled for NMR experiments (a) . ^6Li MAS NMR spectra of ex situ LNO cathode samples (b) . Two regions of interest are labelled with coloured lines in both figures. ³¹	43
Figure 3.15 Variable temperature ^7Li solid-state NMR spectra of LNO at three different states: (a) pristine LNO, (b) $\text{Li}_{0.80}\text{NiO}_2$, and (c) $\text{Li}_{0.50}\text{NiO}_2$. Asterisks (*) and plus (+) signs indicate the position of spinning sidebands. Note that for $\text{Li}_{0.80}\text{NiO}_2$ two signals were detected in contrast to the single signal in ex situ NMR data. (cf. Figure 3.14 ; this might be caused by the faster spinning used in the ex situ measurements associated with a slightly enhanced temperature), but the broadening and position of the signal look the same.	45
Figure 3.16 (a) Voltage profile and (b) contour plots of in situ ^7Li NMR data recorded on an LNO/Li half-cell during cycling between 2.8 to 4.7 V at a rate of 0.05 C. LNO, Li metal and electrolyte are separately labelled. The same behaviour of signal left shifting as in ex situ ^6Li NMR (Figure 3.14) is also found in the highly charged region which is also indicated in the voltage profile. (c) A magnified view of the range 330 - (-60) ppm is used to monitor the evolution of Li metal and electrolyte signals.....	49
Figure 3.17 The static ^7Li NMR spectra of Li metal, electrolyte, and LNO measured separately by putting each part into the pouch cell.....	50
Figure 3.18 Selected static ^7Li NMR spectra extracted from the in situ NMR measurements for charging steps of 5 h. The small peak located close to the electrolyte signal (at 10 ppm) gradually disappears as described in the text.....	52
Figure 3.19 The comparison of the first in situ ^7Li NMR spectrum of the complete battery in comparison to the spectrum obtained after the complete first cycle. Attention should be paid to the increasing area of the small peak located at 10 ppm.	53
Figure 3.20 (a) Ni K-edge XAS spectra of the in situ LNO/Li half-cell. Cell voltage as a function of state of charge for the first cycle; (b) The in situ XAS spectra in the energy range between 8300 and 8700 eV; (c) An expanded view of the region of the pre-edge peak; (d) the edge region of 19 XAS spectra is enlarged to analyse the change of oxidation state and (e) Experimental Fourier transforms for Ni K-edge spectra as a function of state of charge. ³¹	54
Figure 3.21 Li mobility calculated from GITT of LNO/Li half-cells.	56

Figure 3.22 Repeated GITT measurement of LNO/Li half-cells.....	57
Figure 4.1 (a) full temperature region and (b) enlarged region of TGA measurement on LNO in air from room temperature to 1000 °C (750°C for (b)). The green numbers correspond to the mass loss of denoted regions.	64
Figure 4.2 (a) Full temperature region and (b) enlarged region of the repeated TGA measurement of as-prepared LNO in air from room temperature to 1000 °C.	65
Figure 4.3 Electrochemical performance during galvanostatic cycling at 0.5 C in the voltage range of 2.5-4.5 V: (a) pristine LNO, LNO-200, LNO-300, and LNO-400, (b) long-term cycling performance of LNO-400, (c) comparison between LNO-350, LNO-360, LNO-370, LNO-380, and LNO-390 and (d) long-term cycling performance of LNO-380 and LNO-390. (e) Cell voltages as a function of specific capacities during the 1 st cycle of all cathodes and (f) differential capacity as a function of cell voltage (dQ/dV vs. V) of selected cathodes. The red dashed arrows show the changes with increasing heating temperature.	66
Figure 4.4 Electrochemical performance during galvanostatic cycling at 0.5 C: (a) Cycling performance of LNO-360 and LNO-370 in the voltage range between 2.5-4.3 V, (b) the difference between pristine LNO and the reheated LNO-400, (c) cell voltages as a function of specific capacities during the 1 st cycle of LNO-500 and LNO-600, (d) cell voltages as a function of specific capacities during the 1 st cycle of LNO-700, and (e) Cell voltages as a function of specific capacities during the 1 st cycle of LNO-850.....	69
Figure 4.5 The XRD Rietveld refinement pattern of LNO with Li/Ni antisite mixing.....	71
Figure 4.6 The XRD Rietveld refinement pattern of LNO with excess Ni in Li layers.	72
Figure 4.7 The XRD Rietveld refinement pattern of LNO with Li/Ni exchanging with different composition on the Li and Ni sites.	73
Figure 4.8 The XRD Rietveld refinement pattern of LNO with vacancies in Ni layers.	74
Figure 4.9 (a) The change of Ni occupancy on Li sites (%) from the Rietveld refinement results. 25 °C represents the pristine state. Three regions are labelled I, II, and III. (b) The change of phase composition with increasing heat-treatment temperatures.	75
Figure 4.10 XRD Rietveld refinement pattern of LNO-600.	76
Figure 4.11 (a) XRD Rietveld refinement pattern of LNO-750 and (b) the enlarged view showing the tiny reflections from Li ₃ Ni ₁₋₃ O cubic phase.	78
Figure 4.12 XRD Rietveld refinement pattern of (a) LNO-800 and (b) LNO-850.....	79
Figure 4.13 The XRD Rietveld refinement pattern of LNO-1000.	80
Figure 4.14 The comparison of refinement against XRD patterns of (a) LNO-1000 and (b) Ni(OH) ₂ -1000 using a molybdenum source.	81
Figure 4.15 The electrochemical performance of LNO-400, 600, and 800 °C samples reheated at 700°C.....	82

Figure 4.16 In situ high temperature SRD of LNO in air from room temperature to 900 °C.	83
Figure 4.17 The change of phase composition obtained from the refinement against in situ XRD patterns acquired during heating.	84
Figure 4.18 The value of Ni occupancy on Li sites obtained from refinement against in situ XRD patterns acquired during heating.	84
Figure 4.19 (a) Enlarged regions of in situ XRD pattern focusing on the impurities and (b) the change of 101, 006, 012, and 104 reflections during heat treatment. The temperature regions showing impurity formation and phase transition are marked with red color in (a) and (b) , respectively.....	85
Figure 4.20 The refinement against the XRD pattern of LNO-900 acquired during heating. Five phases are added to fit the pattern.	86
Figure 4.21 ⁷ Li NMR spectra of pristine LNO and some thermally treated samples. (a) The spectra are stacked with original intensities. The small peak at 425 ppm is labelled with the red heart. (b) The intensity is normalized via the maximum value of the main peak. Asterisks and plus signs indicate the position of spinning sidebands.	87
Figure 4.22 The extended range of ⁷ Li MAS NMR spectra including all sidebands. The plus sign denotes the sidebands belonging to the isotropic peak at 700 ppm and the asterisk labels the sidebands belonging to the peak at 0 ppm associated with diamagnetic lithium salts on the surface.	88
Figure 4.23 (a) NMR spectra of pristine LNO and all thermally treated samples. (b) LNO-700 and LNO-1000 are separately further replotted to show the details. The small peak located at 425 ppm is labelled with a heart. Two different sets of spinning sidebands are labelled with plus and asterisks in the spectra, separately.....	91
Figure 4.24 Ni K-edge XAS spectra of the pristine and heat-treated LNO samples and (b) the enlarged view of the edge region. (c) the edge position as defined by the energy where the edge crosses the value 0.55.....	92
Figure 4.25 ZFC/FC curves of pristine and heat-treated samples measured at 5000 Oe.....	95
Figure 4.26 (a) FC curves and (b) the change of parameter T_B of the pristine and heat-treated samples. (c) The field scans measured at 300 K up to $7 \cdot 10^4$ Oe and (d) the corresponding z-component magnetization $M_z(300K)$. (e) The field scans measured at 2 K up to $7 \cdot 10^4$ Oe and (f) the corresponding z-component magnetization $M_z(2K)$. (g) The high-temperature inverse susceptibility χ^{-1} measured at 5000 Oe where the part from 340 K to 390 K was used for Curie-Weiss fits and (h) the effective paramagnetic moments μ_{eff} in units of Bohr's magneton μ_B , and Weiss constant θ	96
Figure 4.27 Individual field scans at 2 K to illustrate more clearly the evolution of the coercivity fields.	97
Figure 4.28 The coercivity field CF(2K) extracted from the field scans at 2 K.	99
Figure 4.29 Hysteresis measurements at 300 K and 390 K with maximum fields of 5000 Oe.	101
Figure 4.30 Magnetization vs. temperature measurement at high temperature from 270 K to 390 K measured at a field of 5000 Oe.	101

Figure 4.31 Curie-Weiss fits to the 340 K to 390 K temperature region of the inverse susceptibility χ^{-1}	102
Figure 4.32 The inverse susceptibility curves χ^{-1} obtained at 5000 Oe.....	102
Figure 4.33 (a) low-magnification TEM image of LNO particles with the corresponding electron diffraction pattern shown as the inset; (b) high-magnification TEM image of LNO with interplanar spacing of (003) being labelled; HAADF image of LNO-200 with the strongly off-stoichiometric $\text{Li}_{1-z}\text{Ni}_{1+z}\text{O}_2$ region (c) parallel and (d) normal to (003) direction marked by the yellow boxes; The blue dots denote the Ni^{2+} migrating to Li sites with increased intensity on Li column. HAADF image of LNO-400 with (e) the strongly off-stoichiometric $\text{Li}_{1-x}\text{Ni}_{1+x}\text{O}_2$ region and (f) thin cubic phase on particle surface.....	106
Figure 4.34 (a) STEM image of an LNO particle, (b) Ni L-edge chemical shift mapping of the yellow area in (a) and (c) corresponding EELS spectra from different locations revealing a reduced oxidation state of Ni at the surface.....	107
Figure 4.35 (a) low-magnification TEM image of LNO-400, (b) the corresponding EEL spectra-based Ni L-edge chemical shift, (c) Ni oxidation state mapping marked with the green rectangle in (a) and (d) the profile of the bulk and surface fitting, revealing the concentration of $\text{Ni}^{2+}/\text{Ni}^{3+}$. EEL spectra-based analyses on LNO-700: (e) High-magnification TEM image, (f) Ni M-edge/Li K-edge ratio mapping, (g) Ni L-edge chemical shift mapping and (h) the mapping of $\text{Ni}^{2+}/\text{Ni}^{3+}$ distribution. (i) shows the relative concentration of $\text{Ni}^{2+}/\text{Ni}^{3+}$	108
Figure 4.36 Corresponding spectra of O K-edge and Ni L-edge on surface and bulk from the green area in Figure 4.35a	109
Figure 4.37 Corresponding to the spectra of O K-edge and Ni M/L-edge on surface and bulk as shown in Figure 4.35f, g	110

List of Tables

Table 3.1 Detailed information about the refinement against the XRD data.....	31
Table 3.2 Different Li environments in two models of $\text{Li}_{0.6}\text{NiO}_2$ when considering $\text{Ni}^{3.5+}$ ions as Ni^{3+} and Ni^{4+} separately. ³¹	40
Table 3.3 Different Li environments in two models of $\text{Li}_{0.5}\text{NiO}_2$ when considering $\text{Ni}^{3.5+}$ ions as Ni^{3+} and Ni^{4+} separately. ³¹	41
Table 3.4 Comparison between the experimental and calculated shifts for the Li_xNiO_2 phases.	41
Table 3.5 Parameters of ^6Li NMR peaks in the ex situ measurement.	42
Table 3.6 Comparison of peak positions between in situ ^7Li NMR and ex situ ^6Li MAS NMR spectra.	50
.....	
Table 4.1 Summary of the electrochemical performance of all mentioned materials.....	69
Table 4.2 Detailed information about the refinement in Figure 4.5	71
Table 4.3 Detailed information about the refinement in Figure 4.6	72
Table 4.4 Detailed information about the refinement in Figure 4.7	73
Table 4.5 Detailed information about the refinement in Figure 4.8	74
Table 4.6 Summary of relevant information of thermally treated samples. The decrease of edge position in XPS corresponds to the continuous reduction of Ni. The temperature T_B in PPMS indicates the number of Ni^{2+} ions located in the Li layers, corresponding to the value in the fourth column, i.e. the value of Ni located in the Li layers obtained by Rietveld refinement. The last column shows the values of capacity retention when cells containing corresponding materials as cathodes were cycled between 2.5-4.5 V at 0.1 C.	113

Chapter 1 Introduction

1.1 Li-Ion Batteries

Stimulated by the projects of net-zero carbon emissions and an urgent switch from fossil fuels to sustainable “green” energy sources, rechargeable lithium-ion batteries (LIBs) have gained enormous interest from both academia and industry. Since the first commercialization by Sony in 1991, market opportunities for LIBs have grown beyond consumer electronics to electric vehicles (EVs). In the last decades, the number of EVs has increased substantially from 17 000 to 7.2 million, and, with an annual growth rate of ~30%, near 140 million EVs will be on the road by the end of the next decade.¹ Ni-based layered transition metal oxides have played vital roles in chosen cathode materials in LIBs for EVs powering.^{2,3} In the early days of 2012, all batteries used to power EVs are based on $\text{LiNi}_{1/3}\text{Co}_{1/3}\text{Mn}_{1/3}\text{O}_2$ (NCM111) cathode materials. However, the growing demand for higher specific energy motivates the development towards cathodes with higher Ni-content, i.e. Ni-rich cathodes. Enriching Ni in the compositions can increase the specific energy, hopefully approaching the goal of 350 Wh kg^{-1} at a cell level by 2025.⁴ In addition, cobalt is a key ingredient in the present cathode chemistry and its price has tripled in recent years because of the supply chain constraints.⁵ With millions of EVs being manufactured by 2050, the global cobalt reserves will not satisfy the Co demand for battery production before 2045.⁶ Therefore, a transition to Co-free or low-Co cathodes is necessary to reduce LIB cost and to make the growth of the EVs market sustainable.^{1,5} Considering the issues of cobalt price and high-energy-density batteries, academic and industrial attention is paid to the adoption of Co-free Ni-rich cathodes, such as $\text{LiNi}_x\text{Mn}_y\text{Al}_{1-x-y}\text{O}_2$ and $\text{LiNi}_x\text{Fe}_y\text{Al}_{1-x-y}\text{O}_2$. The substitution content should be kept at a low level as the redox-inactive nature of Mn and Al ions decreases the specific capacity. Clearly, compositions enriched in Ni are equivalent to approaching their parent material, LiNiO_2 . A capacity/stability tradeoff is then established since LiNiO_2 suffers from severe intrinsic stability issues.^{3,4,7-9} Therefore, the structure-property relationship of LiNiO_2 needs to be revisited, with the aim of pointing out challenges of this “old” material to be addressed. The stability problem can be overcome or mitigated hopefully by using as little modification as possible, without much sacrifice on capacity. Adoption of such “ LiNiO_2 analogs” will significantly reduce battery costs for EVs (\$8500 total pack cost, \$3500 material cost) in comparison to battery systems using NCM cathodes (\$10 000 total pack cost, \$5000 material cost).⁵

1.2 Fundamentals of Batteries

A battery, consisting of an array of electrochemical cells, is a device converting chemical energy into electrical energy during discharge. Regarding a rechargeable or secondary battery, this energy conversion process is reversible. A cell can be regarded as two separate reactions of chemical species, in which the ions and electrons move separately. The chemical species are named electrodes, which must be conductive or coated onto a conductive substrate. The electrical potential produced by the cell is determined by the different chemical potentials of the electrodes.

$$\Delta G_r^\circ = -zFV_{oc} \quad (1.1)$$

Equation (1.1) describes the present balanced energy for batteries under open-circuit conditions (there is no external circuit and no flowing current). ΔG_r° is the standard Gibbs free energy, describing how much energy would be liberated when the two electrodes react together under standard conditions. The equation is balanced by electrostatic energy, where V_{oc} corresponds to the open-circuit voltage of the battery, F is the Faraday constant, and z represents the charge number of the ions transported in the reaction.

The mediation process of the flow of ions between the two electrodes is conducted by an electrolyte. Acting as a separator, the electrolyte must be electronically insulating, driving the electrons to flow through an external circuit. In addition, the electrolyte must not be reactive with either electrode. **Figure 1.1** presents a schematic of the energy levels in the electrodes and the electrolyte of an electrochemical cell.¹⁰ The energy separation E_g between the reduction and oxidation potential is the thermodynamic stability window of the electrolyte. The two electrodes are electronic conductors with electrochemical potentials $\tilde{\mu}_{e^-, \text{Anode}}$ and $\tilde{\mu}_{e^-, \text{Cathode}}$. An anode with $\tilde{\mu}_{e^-, \text{Anode}}$ above the reduction potential will reduce the electrolyte unless a passivation layer creates a barrier to electron transfer from the anode to the electrolyte. On the other hand, a cathode with $\tilde{\mu}_{e^-, \text{Cathode}}$ below the oxidation potential will oxidize the electrolyte unless a passivation layer blocks electron transfer from the electrolyte to the cathode.

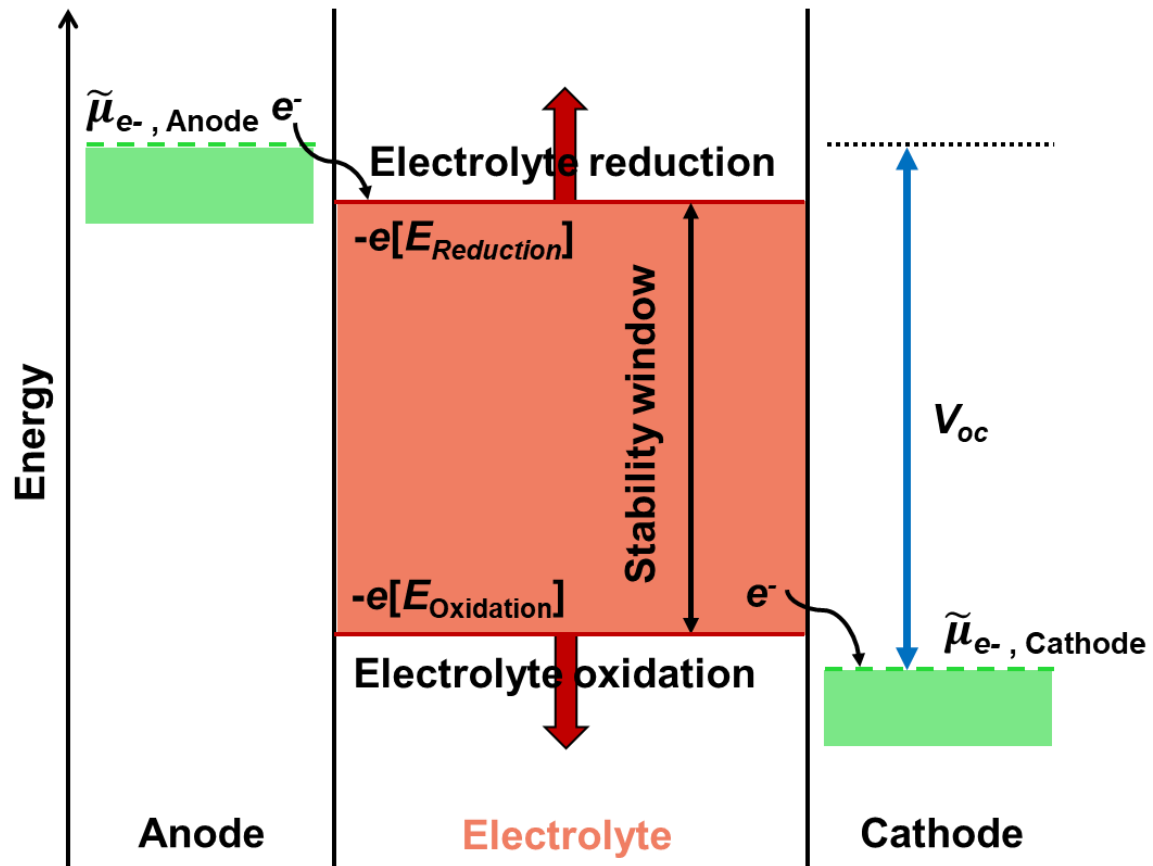


Figure 1.1 Schematic open-circuit energy diagram of an electrolyte. $-e[E_{Reduction}]$ and $-e[E_{Oxidation}]$ are the reduction and oxidation energies of the electrolyte. E_g is the electrochemical stability window of the electrolyte. $\tilde{\mu}_{e^-, Anode}$ and $\tilde{\mu}_{e^-, Cathode}$ are the electrochemical potentials of anode and cathode, respectively. V_{oc} is the open-circuit voltage. Figure adopted from Hubert H. Girault et al.¹⁰

1.3 Intercalation Chemistry

An open framework structure is possessed by most electrode materials for rechargeable batteries. The mobile guest species (for example, Li^+) can be inserted or extracted into such frameworks. These stable hosts, such as the aforementioned LiNiO_2 , often have a layered structure with interlayer space, which can be occupied by the guest species. Removal (or insertion) of the guest species can occur by two diverse thermodynamic mechanisms: a solid-solution reaction, corresponding to the smooth increase of the guest concentration in the host structure. No interface or phase separation can be caused throughout the whole structure. On

the other hand, a second phase may be formed by the insertion of the chemical species. When more guest species are intercalated, this phase (ordered or disordered) nucleates and gradually replaces the original one by phase transformations (**Figure 1.2**). These two mechanisms correspond to the different electrochemical responses. The chemical potential of the products of reactions between the two electrodes determines the potential of the cell: for a solid solution, the continuously changed compositions result in a monotonic variation in the electrochemical potential. Hence, a sloped response is expected. However, a voltage plateau with constant potential reflects a two-phase transition process since the composition of the structure, which accepts chemical species, does not change. Only the relative fraction of two phases changes, until the phase transition process comes to an end.

There is a free-energy barrier in two-phase reactions as a result of the coherency strain energy and interfacial energy between the two phases.¹¹ Therefore, a voltage hysteresis is observed (more obvious on a faster lithiation/delithiation process), causing a reduction in the reversible capacity (voltage window is fixed) and energy efficiency.¹² The free-energy barrier can also induce the inhomogeneous distribution of the current on different electrode particles, leading to the over-charge of individual particles. The mechanical stability of the particles is also influenced by the insertion/extraction mechanism. Regarding a solid solution, a Li concentration gradient inside a particle can induce stress and strain, sometimes even the formation of cracks. The situation is getting even worse when a sharp lattice expansion or contraction occurs during Li insertion/removal. Such stress and strain are thought to be larger at the interface in two-phase reactions, giving rise to more pronounced mechanical degradation. The rate of the two-phase reaction is determined by the rate of nucleation and movement of the phase boundary inside the particles.

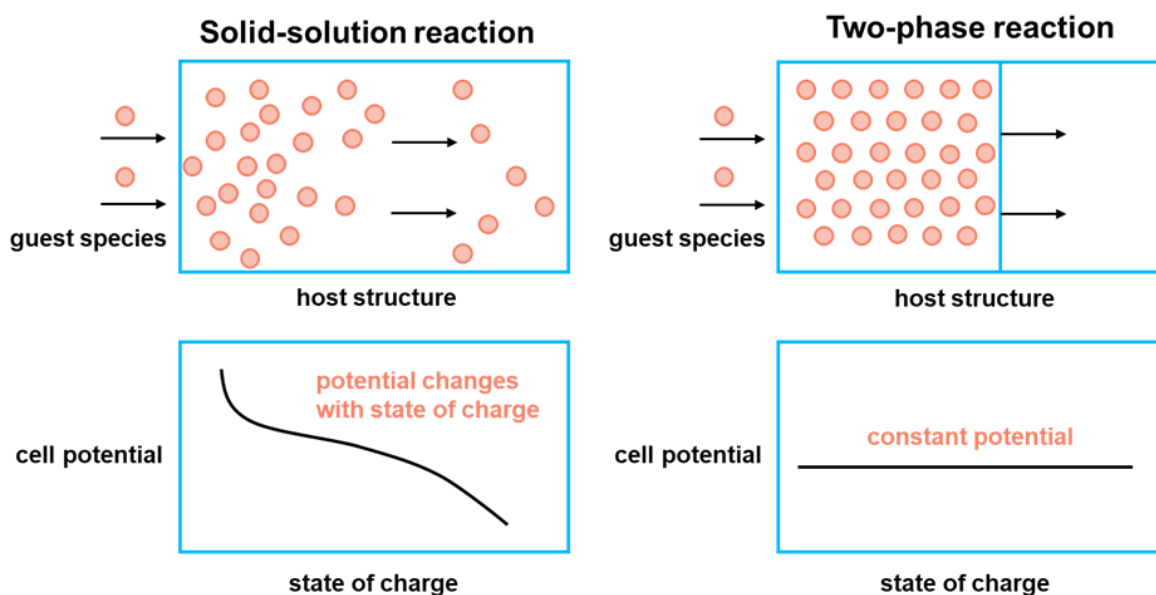


Figure 1.2 Schematic diagram of intercalation of guest species into host structures via or solid-solution reaction or two-phase reaction. The corresponding response of the potential in the potential profile is also displayed. The newly formed second phase during a two-phase reaction can be ordered or disordered.

1.4 The Crystal Chemistry of LiNiO_2

The structure of LiNiO_2 was first reported in 1954 with a typical O3 structure (space group $R\bar{3}m$).¹³ The layered structure contain an *fcc* array of oxygen anions with *AB CA BC* stacking sequence, and alternating layers are occupied by the TM ions and Li ions.¹⁴ The “O” in O3 represents the octahedral coordination environment of the lithium, and the number 3 denotes how many slabs of TMO_2 are stacked along the (hexagonal) *c* axis in the unit cell. A symmetry reduction from $R\bar{3}m$ to $C2/m$ is often observed for LiNiO_2 with a distorted O3 structure. The symbol of O’3 is used to denote such monoclinic phases (M) and to distinguish them from the O3 structure, while emphasizing that the stacking of O3 is remained (**Figure 1.3**). Upon charge and discharge, most phase transitions in LiNiO_2 occur with this stacking sequence being preserved. A second notation system, therefore, is used to describe such phase transformations. The phases are labelled by a letter, which represents the symmetry of the unit cell, and a number that gives information about the sequence in which each phase of certain symmetry appears on charge. In this system, structures are typically denoted as “H” (hexagonal) rather than “R” (rhombohedral), since hexagonal lattice settings are usually adopted to describe structures in the rhombohedral lattice system: the layers are perpendicular to the *c* direction and parallel to

the *ab* plane. The pristine state of LiNiO₂ is labelled as “H1” and the next phase appearing in the O3 structure on charging is “H2”, etc. The observed order of phases for LiNiO₂ is H1 → M → H2 → H3, which will be discussed in the next section below in detail.

During the synthesis, LiNiO₂ always exhibits a deviation from ideal stoichiometry with a formula of Li_{1-z}Ni_{1+z}O₂, in which *z* denotes the amount of Ni located in the Li layer.¹⁵ A *z* value of 0.01-0.02 is usually observed, although the synthetic conditions are well controlled. The crystallization with ideal stoichiometry is challenging partly due to the harsh conditions of the oxidation environment needed to stabilize Ni³⁺. On the other hand, the decomposition already occurs towards Li_{1-z}Ni_{1+z}O₂ during synthesis due to the loss of Li, and because the annealing times are too long or the temperature is higher than the value for decomposition.¹⁶ The decomposition reaction will be introduced in the section below. The actual value of *z* can be obtained by a Rietveld refinements in a reproducible way.¹⁵ For the off-stoichiometry Li_{1-z}Ni_{1+z}O₂, a negative value for the isotropic thermal displacement parameter at the lithium site (*B*(Li)) is obtained, because the electronic density is larger in the material than in the actual 2D-structural hypothesis. Therefore, when *B*(Li) is fixed, the amount of Ni at the Li site can be refined. For charge compensation, the average oxidation state of Ni in Li_{1-z}Ni_{1+z}O₂ is 3-2*z*, which indicates the presence of 2*z* Ni²⁺ within the material. Half of the Ni²⁺ ions are located in the Li layers, while the other half are also formed in the Ni slab, yielding the formula [Li_{1-z}Ni²⁺]_{3b}[Ni²⁺_zNi³⁺_{1-z}]_{3a}[O₂]_{6c}.¹² Another possible model for Li/Ni arrangement is the formation of paired anti-site defects, i.e., an amount of *z* Li per formula unit occupying Ni sites and vice versa. Notice that, it is challenging to get results about the absence of Ni ions in the Ni slab by XRD. However, neutron diffraction experiments show that the Li/Ni mixing only appears in the most off-stoichiometry phase (*z* = 0.25 in Li_{1-z}Ni_{1+z}O₂).¹⁷ For Mn-substituted LiNi_{1-y}Mn_yO₂, increasing the *y* value also induces Li/Ni cation mixing with Li[Li_{1/3}Mn_{2/3}]O₂ being formed.¹⁸ In this thesis, the model of Li_{1-z}Ni_{1+z}O₂ is used to facilitate discussion. The amount of *z* Ni²⁺ in the Li layers strongly influences almost all of the properties of LiNiO₂, including magnetic behavior, phase transformation route, electrochemical performance, and overall stability, as discussed in the following sections.

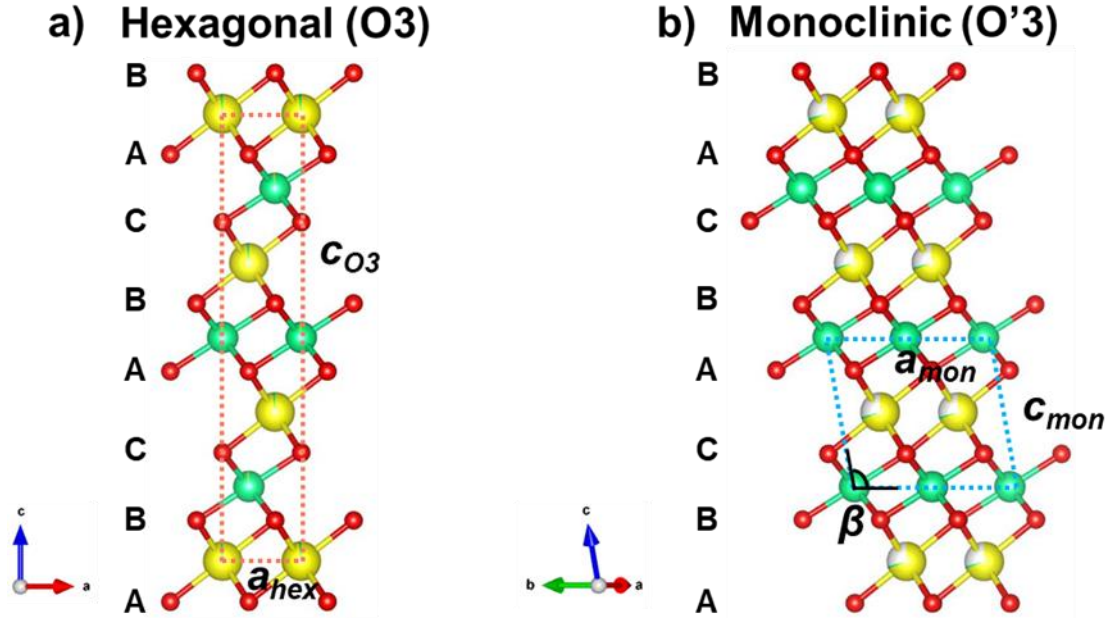


Figure 1.3 Illustration of crystal structures relevant to layered LiNiO_2 . They are labelled using the crystallographic family they belong to ((a) hexagonal and (b) monoclinic) and Delmas's notation (in brackets). The stacking sequences are indicated by labelling the oxygen planes. Unit cells are displayed in orange (hexagonal) and blue (monoclinic). Li, Ni, and O atoms are shown in yellow, light green, and red, respectively.

The off-stoichiometry z has a strong influence on the magnetic properties of LiNiO_2 .^{19,20} The electron configuration of Ni^{3+} is $3d^7$ and the crystal field splitting in octahedral coordination induces $(t_{2g})^6(e_g)^1$ occupation with a doublet electronic configuration ($S = 1/2$). An effective paramagnetic spin-only magnetic moment of $\mu_{\text{eff}}^{\text{Ni}^{3+}} = 2\sqrt{S(S+1)}\mu_B = 1.73\mu_B$ is therefore expected. For Ni located on a triangular lattice in ideal LiNiO_2 , a paramagnetic behavior rather than long-range order arises, because of the quantum mechanical frustration of the antiferromagnetic coupling.²¹ However, when Ni^{2+} with the configuration of $S = 1$ is placed on the Li sites, a transition to a long-range magnetic ordering occurs, together with a rapid increase of the magnetic susceptibility.²² The Ni^{2+} in the Li layers couple antiferromagnetically with the Ni in the neighbouring Ni slabs and, as a result, locally ordered magnetic clusters (possibly ferrimagnetic) are formed. Thus, the temperature, where the magnetic transition happens, increases with increasing amount z of Ni^{2+} on the Li sites. This characteristic has also been used as the reliable tool to determine the stoichiometry of LiNiO_2 .

1.5 The Structural Evolution during Cycling of LiNiO₂

The phase behavior of LiNiO₂ has been investigated by many authors, particularly by means of operando X-ray diffraction (**Figure 1.4**).^{23–25} As lithium is extracted from the material, phase transitions follow a sequence of H1 → M → H2 → H3. These can also be associated with the multiple plateaus in the corresponding voltage profiles, indicating behaviors of two-phase reactions.²⁶ In detail, the pristine Li_xNiO₂ (H1) exhibits a solid-solution behavior until $x \approx 0.8$, after which a phase transition from H1 to a monoclinic structure (M) is observed. This M phase is evidenced by a splitting of the 101 and 104 Bragg reflections, giving rise to $20\bar{1},110$ and $20\bar{2},111$ reflection pairs, respectively. The monoclinic symmetry extends to $x \approx 0.4$, where a second phase transformation named M to H2 occurs between $x \approx 0.4$ and 0.36. H2 is stable up to high states of charge ($x \approx 0.25$), where a first-order H2-H3 transition is observed in the range of $x \approx 0.25$ -0.16. The H3 phase, having a much smaller c parameter, is characterized by a new 003 reflection at around 8° (not shown in the figure). The stacking sequence of O3 is maintained in H3, while stacking faults have been observed from the broadening of 018 reflections.¹⁴ Up to now, the driving force for the H2/H3 phase separation is under discussion, because the biphasic process induces a highly strained interface. Notice that, some discrepancies about the Li content where the transitions occur, exist in the literature. This is attributed to the different off-stoichiometry of LiNiO₂ and cycling conditions.^{27–29}

The evolution of cell parameters can be obtained by the Rietveld refinement against operando X-ray diffraction patterns. The hexagonal lattice setting is typically adopted for convenience. The a_{hex} keeps decreasing monotonically through the delithiation as the oxidation of Ni³⁺ to Ni⁴⁺ induces a contraction in the NiO₆ octahedra. The variation of c_{hex} follows a two-section behavior. During the process of the H1 → M → H2 transitions, an increase is observed as a result of the increased O-O electrostatic repulsion. When Li is continuously removed from the lattice, the screening effect is less effective. In the H2-H3 biphasic region, c_{hex} sharply decreases since the structure becomes more covalent, behaving like transition-metal sulfides. The O anions are less electronegative with less electrostatic repulsion between each other. The steric effect causes the contraction of the Li layers. A significant strain is induced at the interface when shrinkage of the unit cell is introduced during the H2/H3 two-phase reactions.³⁰ This makes the transition less reversible as well as introduces the formation of cracks during cycling.

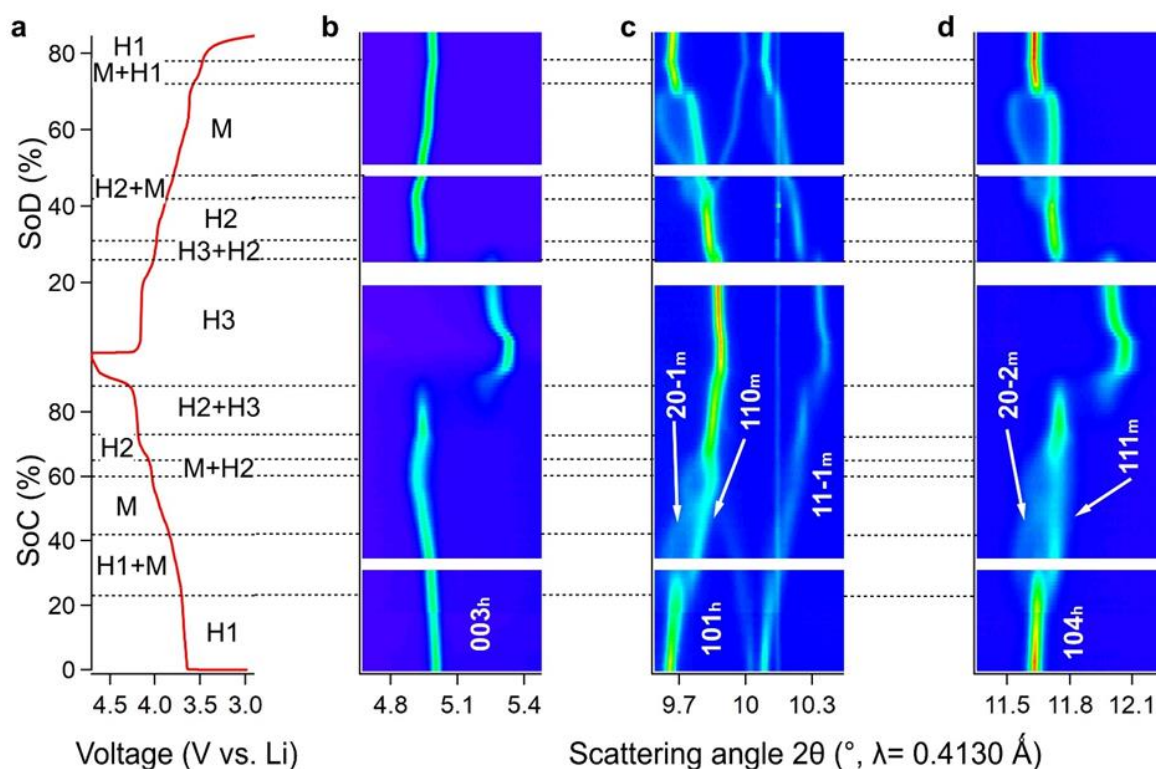


Figure 1.4 Contour maps of in situ synchrotron diffraction of LNO collected during the first cycle. (a) Cell voltage as a function of state of charge or discharge of the 1st cycle, which is aligned with the diffraction patterns; XRD patterns of selected scattering angle regions: (b) 4.68°-5.48°, (c) 9.59°-10.45° and (d) 11.36°-12.26°. The phases in each region are labelled in (a). The peak splitting for phase M is also indicated in (c) and (d). Reprinted from my own publication.³¹

The origin of lowering in symmetry from hexagonal to monoclinic has been the subject of substantial investigation. The nature of the monoclinic phase has been associated with various domains, where Li-vacancy orderings are stabilized. These structures (**Figure 1.5**), at compositions of $x = 3/4, 5/8, 1/2, 2/5,$ and $1/4$ in Li_xNiO_2 , can be experimentally observed as the minima in dQ/dV curves.¹⁴ Such Li-vacancy ordering structures are possibly stabilized by both the in-plane Li-Li repulsion and interplane $180^\circ \text{Li}_A\text{-O-TM-O-Li}_B$ chains with a Jahn-Teller (JT)-active Ni^{3+} centre.³² The structure of $x = 1/2$ is extensively reported with alternating rows of fully occupied and vacant Li sites.^{33,34} $x = 3/4$ has a similar ordering, where now the Li sites of the empty row are alternatively vacant and occupied.³⁵ Another stable structure

appearing between the above-mentioned orderings is $x = 5/8$. It can be regarded as a filled row of Li alternating with another row with one out of three occupied Li sites.¹⁴ An enlarged unit cell needs to be constructed to describe such an ordering, matching the discovery from electron diffraction.³³ Other ordering structures, such as $x = 2/5$ and $x = 1/4$, have never been proved experimentally. However, they correspond to the end of the monoclinic and the H2 phase region, respectively. The Li ordering can be disrupted by the local disorder, including off-stoichiometry and Ni substitution. A smoother voltage profile will also replace the one with multiple voltage plateaus.

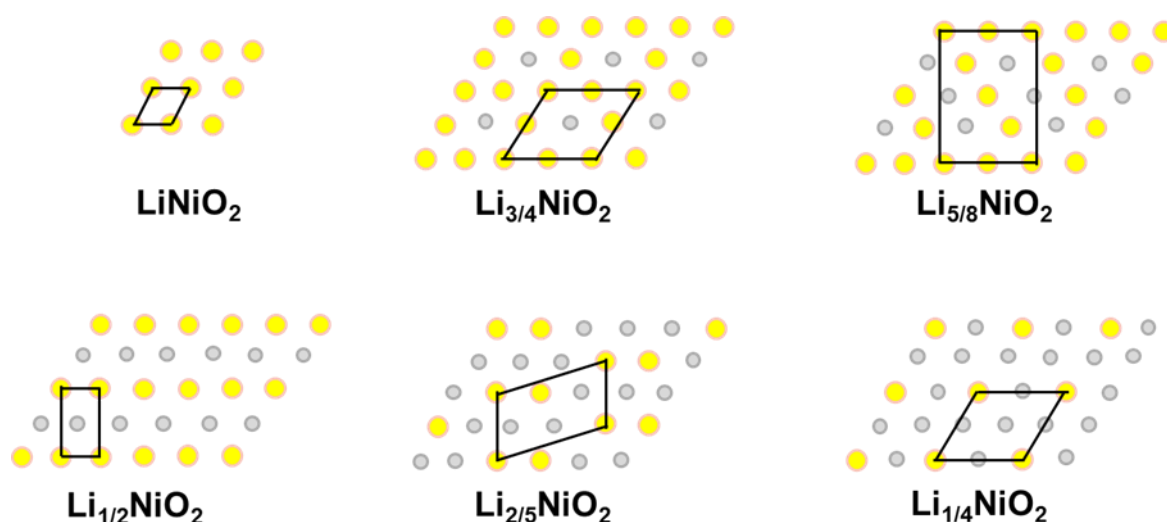


Figure 1.5 Li/vacancy ordering structures with Li ions and vacancies labelled as yellow and grey spheres, respectively. Unit cells are outlined with solid black lines. Figure adapted from Mock.³⁶

z Ni^{2+} ions located on Li sites in $\text{Li}_{1-z}\text{Ni}_{1+z}\text{O}_2$ have a profound influence on the initial Coulombic efficiency, i.e. they result in a large difference in the initial charge and discharge capacity (10-15%). Upon the first charge, Ni^{2+} in the Li layers can be oxidized to Ni^{3+} , causing a local collapse of the interlayer. The six lithium sites around each of these Ni^{3+} ions are difficult to be occupied by Li^+ on lithiation¹⁵ because the local smaller interlayer space causes poor Li diffusion kinetics. Although at a very low rate these sites can still be activated, the reversibility of the material is strongly affected, resulting in an inhomogeneous distribution of Li, i.e. lithiation gradients (a small number of phases are over-lithiated). Notice that, except for the hindrance from $z\text{Ni}^{2+}$ in the Li layers, LiNiO_2 suffers from slow kinetics at high Li concentrations.³⁷ It can be recognized from the voltage plateau close to 3.5 V. Two factors

contribute to the increase of the activation barrier for Li diffusion. Firstly, there are not enough di-vacancies in the Li layers allowing for fast Li diffusion at higher Li content because the lowest energy barrier corresponds to the diffusion via di-vacancies³⁸ Secondly, Li diffusion between adjacent octahedral sites is via an intermediate tetrahedral site.³⁹ Ni²⁺ in the Li layers and the high Li concentration upon discharge induce a smaller interlayer spacing, therefore decreasing the tetrahedron height and increasing the activation barrier for Li diffusion.⁴⁰

1.6 The Synthesis and Decomposition of LiNiO₂

Different methods have been adopted to synthesize LiNiO₂ with high quality. The solid-state reaction is the typical and commonly employed method over the years. Precursors of solid nickel and lithium salts are mixed and calcined. The formation of LiNiO₂ from rock salt NiO occurs in two steps.⁴¹ Firstly, there is a random distribution of Ni and Li in the Ni sublattice up to a composition of Li_{0.3}Ni_{0.7}O.⁴² The lithium amount is increasing and Ni is oxidized in this process. The unit cell volume decreases to a point, where the octahedral sites are so small that further random distribution of Li and Ni is not possible any more. To reduce the steric effect, segregation of Li⁺ and Ni³⁺ occurs with alternating Li and Ni planes along the cubic [111] direction, causing a rhombohedral distortion of the original cubic lattice system.⁴¹ As a result, the newly formed LiNiO₂ has an increasing amount of vacancies in the Ni layers. In the next step, Ni migrates to these empty sites and a fast Li diffusion and occupation occur at the sites where vacancies are formed in Li layers by migrated Ni. As the annealing temperature increases, local layered domains grow into a long-range crystalline LiNiO₂ with reduced amount of defects. Throughout the synthesis, oxygen must be incorporated into the lattice and the O stacking ((006)_R replaces (111)_c) is preserved upon LiNiO₂ crystallization. The steric effect is the driving force for the transition in LiNiO₂ synthesis, i.e. from cubic to hexagonal. The size difference between Li and Ni is increasing as Ni is oxidized from divalent to trivalent ($r(\text{Li}^+) = 0.76 \text{ \AA}$, $r(\text{Ni}^{2+}) = 0.69 \text{ \AA}$, $r(\text{Ni}^{3+}_{\text{LS}}) = 0.56 \text{ \AA}$ based on Shannon⁴³ LS = low spin). Ni³⁺ and Li⁺ are better placed in small slabs (thickness $S = (2/3 - 2z_{\text{ox}}) c \approx 2.11 \text{ \AA}$) and larger slabs (thickness $I = (c/3 - S) \approx 2.62 \text{ \AA}$), respectively, i.e. Li/Ni layering. When the amount of $2z \text{ Ni}^{2+}$ in Li_{1- z} Ni_{1+ z} O₂ increases (as discussed, half of them are located in the Ni slabs and half in the Li slabs), the larger ionic radius of Ni²⁺ increases the slab thickness (S). However, the interslab thickness (I) is decreased because of the smaller Ni²⁺ (vs Li⁺).¹⁵

Controlling some key factors is essential for obtaining LiNiO₂ with ideal stoichiometry. An air or O₂ flow is necessary for transporting the decomposition products of precursors and removing H₂O and CO₂. The choice for the annealing temperature is extremely important. Using high temperatures (not smaller than 800°C) is beneficial for obtaining a well-crystallized sample, as well as full oxidation to Ni³⁺. However, decomposition may already happen at a high calcination temperature, leading to an off-stoichiometric Li_{1-z}Ni_{1+z}O₂.⁴⁴ On the other hand, low temperatures are also possible for synthesis, but give rise to products with impurities and poor crystallization. Long calcination time is also necessary as a result of the sluggish crystallinity process. Trade-offs at temperatures of 600 and 700°C are then frequently employed as optimum.^{45,46} The choice for Li precursors is also of importance. The decomposition temperature of the precursor must be lower than the temperature, where Li₂O loss occurs. That way lithium can incorporate into the NiO lattice promptly. Lithium hydroxides, oxides/peroxides, and nitrides are preferred under such a consideration. Li loss is a vital issue because of the high vapor pressure of Li₂O. The product from the reaction between Li₂O and O₂, e.g. Li₂O₂, is more prone to vaporization at high temperatures. Hence, it is typical to use an excess of Li precursor to compensate for the Li loss and to obtain a close-to-ideal stoichiometric product.

Coprecipitation is another method to produce LiNiO₂ and has the advantage of homogeneity and scalability. An aqueous solution containing nickel (sulfate or nitrate) is pumped into a continuously stirred tank reactor (CSTR). NaOH is subsequently added to obtain a precipitate of Ni(OH)₂. An NH₄OH solution can be used as a chelating agent (particularly important to allow co-precipitation of other metal hydroxides for doped LiNiO₂). The temperature, stirring speed, pH value, and solution concentration need to be carefully controlled to allow homogeneous coprecipitation. The hydroxide precursors are mixed with Li precursors and calcined in a way similar to the solid-state method. By using such a modern method with better-controlled synthesis conditions, LiNiO₂ with superior quality can be obtained. The first charge capacity is close to the theoretical value (255 mAh g⁻¹) with a much smaller irreversible capacity.⁴⁷ Other synthesis ways, including sol-gel, combustion, and hydrothermal method, are seldom used.⁴⁸⁻⁵⁰

As discussed before, the decomposition of LiNiO₂ can occur even during synthesis if high annealing temperatures are adopted. LiNiO₂ decomposes in a way opposite to the synthesis process, i.e. a hexagonal to cubic phase transition. A group of factors, including annealing temperature, atmosphere, and duration, can influence the pace and extent of such a

transformation.⁴¹ Based on the observation by TG,⁵¹ the decomposition has occurred at 700°C and proceeds at a large rate at 800°C. Moreover, the decomposition rate is increased in an atmosphere of Ar but it occurs slower in air or O₂. The lattice parameter a increases during decomposition, while c barely varies. The reduction of Ni³⁺ to Ni²⁺ in the Ni slabs decreases a . The change of c is an interplay between Li loss, Ni reduction, and thermal expansion. Li loss can cause Ni²⁺ occupying vacant sites in the Li layers (decrease in c), while Ni reduction and thermal expansion exhibit an opposite effect. These three factors compete with each other, resulting in a small variation in total.

1.7 Motivation and objectives of the thesis

Lithium-ion batteries (LIBs) are still the most reliable, widely-used, cost-effective, and convenient candidates for decades to enable electromobility, although substantial efforts have been made to develop “beyond-lithium” rechargeable batteries.⁵² The state-of-the-art cathodes for electric vehicles (EVs) are layered solid solutions derived from LiNiO_2 through the substitution of Ni with other elements. Common representatives are called nickel-cobalt-manganese (NCM) and nickel-cobalt-aluminum (NCA), respectively. Al and Mn ions enhance the structural and thermal stability of the material, while it comes at the expense of their gravimetric capacity.⁵³ Recently, the need for batteries with higher energy densities for the automotive market has stimulated efforts to increase the Ni content in NCA and NMC materials.^{47,54} Some aggressive strategies even suggest compositions of Ni above 95%. Clearly, enriching in Ni is equal to approaching their parent material, LiNiO_2 . As discussed above, LiNiO_2 suffers from substantial intrinsic stability issues. Hence, under the background of pushing cathode materials in the direction of LiNiO_2 chemistry, the necessity to reinvestigate the structure issues of LiNiO_2 with modern characterization methods appears. This essay only aims to revisit some points, especially the one (Li/vacancy ordering structures) requiring experimental pieces of evidence. A fresh perspective is also placed on an overlooked topic (thermal stability of LiNiO_2 at low temperatures). The same points can be regarded as starting points for further investigations on Ni-rich compositions of practical interests.

The research objectives of the thesis are the following:

- 1) To investigate the existence of Li/vacancy ordering structures during Li-ion (de)intercalation of LiNiO_2 cathodes, through *in situ* ^7Li and *ex situ* ^6Li NMR spectroscopy. In addition, *in situ* XAS, GITT, and *in situ* XRD are also used to jointly capture changes during the Li-ion deintercalation process.

- 2) To uncover the structural and electronic changes caused by the post-synthesis thermal treatment of LiNiO_2 , i.e. the thermal stability in the pristine state at low temperatures. A combination of characterization methods is used, including *in situ* and *ex situ* XRD, *ex situ* measurements of magnetic properties, and *ex situ* ^7Li NMR spectroscopy.

Chapter 2 Solid State Nuclear Magnetic Resonance

2.1 The Basics of NMR

Nuclear Magnetic Resonance (NMR) spectroscopy is based on transitions between nuclear spin energy levels. For a nucleus with a spin quantum number I , there will be $2I + 1$ spin states and each state has a certain magnetic quantum number $m_I = (-I, -I+1 \dots +I)$. When an external field B_0 is applied to a nucleus, the nuclear Zeeman interaction induces energy separation:

$$\Delta E = -\hbar\gamma_I B_0 \quad (2.1)$$

Where \hbar denotes the reduced Planck's constant and γ_I represents the gyromagnetic ratio of the nucleus. The Larmor frequency ω_0 is given by the combination of B_0 and γ_I , defining the energy of transitions between certain Zeeman states ($\Delta m_I = \pm 1$)

$$-\gamma_I B_0 = \omega_0 \quad (2.2)$$

At thermal equilibrium, the nuclear spins are distributed over the energy levels based on Boltzmann's distribution law. Lower levels are preferentially occupied, giving rise to an equilibrium magnetization M parallel to the applied field B_0 . M is typically labelled in the z direction (**Figure 2.1a**). During an NMR experiment, the equilibrium in the nuclear populations is disrupted by applying an alternating magnetic field perpendicular to the B_0 field via a radio frequency (RF) pulse. A nutation of M about the B_1 field is then induced by the pulse and the flip angle can be adjusted by controlling the duration and field strength of the applied pulse. The RF pulse is arranged to produce an oscillating field perpendicular to z and B_0 . Such an oscillating field can be regarded as two components rotating clockwise and counter-clockwise around B_0 . The two components have frequencies of $\pm\omega_{rf}$. Only the component ($B_1(t)$) which rotates in the same direction as the precession of M has a significant effect on the magnetization. The effect of such a component can be better understood when a rotating frame of reference is created. The new reference rotates at frequency ω_{rf} around B_0 . In this frame B_1 appears as a static field with no time dependence and the apparent Larmor frequency is given by $\Omega = \omega_0 - \omega_{rf}$. We can infer that the effective static field along z is Ω/γ_I . If the value of Ω is small and hence the effective static field is small, the B_1 field can induce the precession of the nuclear magnetization. Regarding the simplest NMR experiment, i.e. one-pulse experiment, the magnetization M is rotated by 90° into the xy -plane by applying a 90° RF pulse and

subsequently the magnetization M relaxes back to the equilibrium state, i.e. along the z direction (**Figure 2.1b**). The free induction decay (FID) measured in the time domain by the RF coil is transformed into the frequency domain, giving the NMR spectrum (**Figure 2.1c**). Two time constants describe the process in which M returns to equilibrium. T_1 corresponds to the return of M in z direction, while T_2 corresponds the decay of the xy -components.

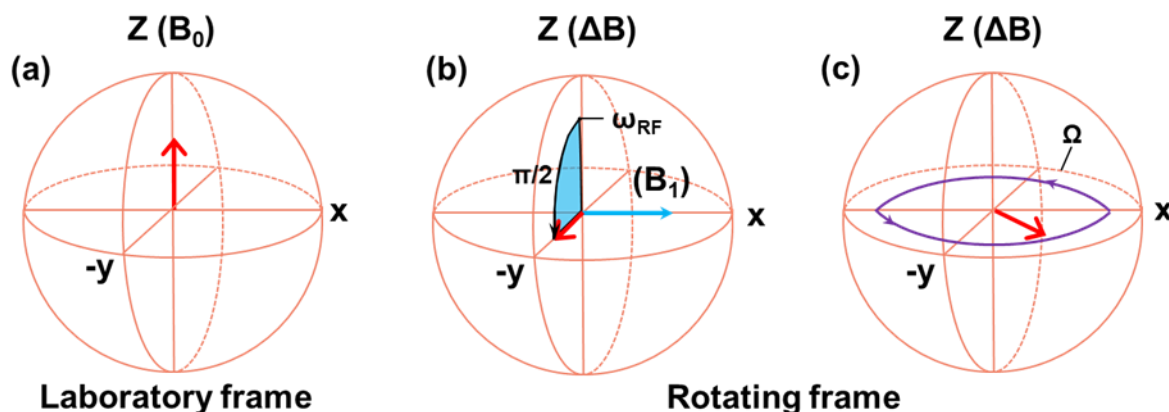


Figure 2.1 “Grapefruit” diagram displaying the evolution of the bulk magnetization M during a one-pulse NMR experiment. (a) the equilibrium magnetization M (red arrow) is aligned along the direction of the B_0 field z . (b) a $\pi/2$ pulse is applied along B_1 (x) and the magnetization is rotated into the xy -plane. (c) the Magnetization precesses in xy -plane (purple arrows) and this precessing magnetization induce a voltage signal in the RF coil. Adapted from reference.⁵⁵

2.2 The Hahn-Echo

As the simplest NMR experiment, the one-pulse sequence has several drawbacks. The coil is used for both sending the RF pulse and acquiring the induced signal. A dead time of few μs exists when the electronics needs to be switched from the application of the pulse to acquisition mode. Therefore, part of the signal is obviously lost during this period. In addition, after switching off the RF pulse some ringing can cause distortions of the acquired signal and thus distortions of the baseline of the Fourier transformed spectrum. A so-called Hahn-echo pulse sequence can mitigate the aforementioned problems of signal loss and baseline distortions. The sequence begins with a 90° pulse followed by a delay τ . A 180° pulse is then applied, flipping the spins around the B_1 axis. After another delay τ , M is refocused in the xy -plane and the coil starts acquiring the signal. In the period of the first τ , the individual spins start to dephase in the xy -plane, resulting from their precessions with slightly different Larmor frequencies as a result

of inhomogeneities in the local fields. These phases are inverted when the 180° pulse inverts the spin ensemble. In the period of the second τ , the relative phases of all spins are decreasing, although each of the spins precesses at their own frequencies. When the signal is detected after the second delay period, the inverted phases have been canceled out and all precessions occur with similar phase. No signals is lost if the dead time for the data acquisition is shorter than τ . The distortion of the baseline is also avoided. In addition, background signals from the probe are suppressed because the 180° pulse mostly affects signals origination from within the signal. The Hahn-Echo sequence is widely applied for the measurement of fast relaxing samples since the initial points of the FID which are highly important must not be lost. This method is also useful for acquiring signals with poor signal/noise ratios owing to the suppression of baseline distortion and background signals. Therefore, all spectra in this thesis were measured using the Hahn-echo pulse sequence.

2.3 Magic-Angle Spinning

In solution-state NMR, most of the orientation-dependent interactions (dipolar, chemical shift anisotropy, and quadrupolar) are averaged out as a result of the rapid time-averaged molecular motion owing to the thermal energy. For the case of the solid-state NMR, crystallites have a fixed orientation with respect to the applied field and such interactions still take effect. Hence the total shift for an individual nucleus depends on the relative orientation of its crystallite. Regarding a powder, crystallites exist in all orientations leading to broad line shapes. The broadening makes it difficult to distinguish even single chemical environments in the crystal. Many anisotropic interactions have a $3\cos^2\theta-1$ dependence, where θ is the angle between the applied B_0 and the main axis of the spin interaction tensor. Although θ takes any values between 0° and 180° , there is a certain relation between θ_R (the angle between the rotation axis and the external field) and θ ⁵⁶:

$$3\cos^2\theta-1 = \frac{1}{2} (3\cos^2\theta_R-1) (3\cos^2\beta - 1) \quad (2.3)$$

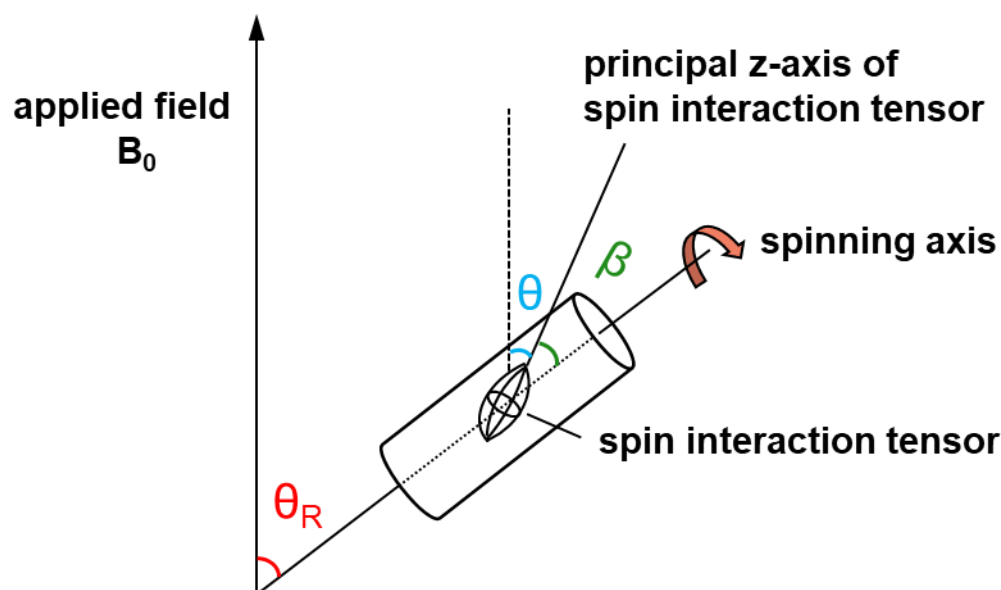


Figure 2.2 The magic-angle spinning experiment.⁵⁶ The sample is spun fast in a cylindrical rotor around a spinning axis orientated at the magic angle ($\theta_R = 54.74^\circ$) with respect to the applied magnetic field B_0 . The spin interaction tensor is represented by an ellipsoid and it is fixed with respect to the corresponding molecule/crystal and thus rotates with the sample. The angle θ is the angle between B_0 and the principal z-axis of the spin interaction tensor; β is the angle between the z-axis of the spin interaction tensor principal axis and the spinning axis.

where β denotes the orientation of the spin interaction tensor with respect to θ_R . Similar to θ , there is no certain value for β . However, if the sample is spun at an angle (θ_R) of 54.74° (magic angle), the time-averaged orientation dependence equals zero (**Figure 2.2**). It means that rotating the sample at the magic angle, as long as the frequency is comparable to or higher than the anisotropy spin interaction, can remove the anisotropy. Three interactions, including nuclear dipolar interaction, the chemical shift anisotropy (CSA), and the 1st order quadrupolar coupling can be averaged by magic-angle spinning (MAS). One condition is that the spinning rate is three or four times larger than the anisotropic interaction frequency.⁵⁶ Furthermore, a set of spinning sidebands appears in the spectra. These are sharp lines separated from the isotropic resonance frequency by a multiple of the spinning rate.

2.4 Paramagnetic NMR

All battery cathodes are based on the redox activities of transition metals. It means that at some specific states paramagnetic ions exist in the sample. The localized unpaired electrons of these paramagnetic ions can couple to nuclear spins (“hyperfine” coupling), giving rise to paramagnetic effects in NMR spectra, leading to both shift and broadening. This can be “spin only” case, however, the coupling of the spin angular momentum (S) and the orbital angular momentum (L) may exist if it is not quenched. The induced “pseudo-contact” NMR shift is typically much smaller than the shift caused by the Fermi-contact shift (discussed below) and will not be considered in this work.⁵⁷ The hyperfine coupling can be described by the Hamiltonian \hat{H}_{IS} .

$$\hat{H}_{IS} = \hat{I} \cdot A \cdot \hat{S} \quad (2.4)$$

Where \hat{I} and \hat{S} correspond to the nuclear spin and electron spin operators, respectively. A represents the hyperfine coupling tensor, which can be divided into two components: the electron-nuclear (e-n) dipolar interaction and the Fermi-contact interaction. The relaxation times of electrons (10^{-8} to 10^{-12} s) are much shorter than the NMR (T_1) relaxation times (ca. 10^{-3} s).⁵⁸ Hence, the nuclear spins couple to the z -component of the time-averaged electron spins (S_z). In addition, the gyromagnetic ratio of the electronic spins is much higher than that of any nuclear spin. Consequently, the effects of hyperfine coupling are typically large.

2.5 Fermi Contact Interaction

Fermi contact interaction is the magnetic interaction between the orbitals having unpaired electrons and the nucleus of interest. The s-orbitals of the nucleus accept the transferred unpaired electron spin density through the intervening orbitals because only s-orbitals have a finite probability at the nucleus.⁵⁹ Such transferred electron spin density at the nucleus causes an additional magnetic field and a variation in the nuclear energy levels. The shift is determined by the isotropic hyperfine coupling constant A_{iso} .

$$A_{iso} = \frac{\mu_0 \mu_B g_e \hbar \gamma_I}{3S} \rho^{\alpha-\beta}(\mathbf{R}_N) \quad (2.5)$$

Where μ_0 is the permeability of free space, μ_B is the Bohr magneton, g_e represents the electron g-factor, γ_I represents the gyromagnetic ratio of the nucleus, S represents the formal electron spin and $\rho^{\alpha-\beta}$ is the unpaired spin density at the nuclear position \mathbf{R}_N . The Fermi contact shift contribution δ_{iso} (ppm) is

$$\delta_{\text{iso}} = \frac{10^6 A_{\text{iso}} \langle S_z \rangle}{\hbar \omega_0} \quad (2.6)$$

The NMR spectra of LiNiO₂ containing paramagnetic centres are dominated by the Fermi-contact shift. The size and sign can be understood owing to the through bond mediation of the unpaired spin density. Local coordination and geometry of the nucleus of interest are considered to explain the exact size and sign of the interaction.

The hyperfine interaction can also occur through space contribution between the nuclear spins and $\langle S_z \rangle$, known as the electron-nuclear (e-n) dipolar interaction. Regarding paramagnetic ions without orbital angular momentum contribution, the interaction is traceless and the isotropic shift δ_{iso} cannot be affected. However, it is the major cause for the broadening in the NMR spectra. When the spinning frequency under MAS is sufficiently high, the e-n dipolar interaction can be averaged, but often it cannot be realized based on currently available hardware. Hence, broad manifolds of spinning sidebands commonly appear on both sides of the isotropic peak. The appearance of such sidebands sometimes makes the assignments more complex.

Both the Fermi-contact and the e-n dipolar interactions are dependent on $\langle S_z \rangle$ (the time average of the z component of the electron spin), which is in proportion to the B_0 field and inversely correlated with temperature. Therefore, lower fields are commonly used for strongly paramagnetic samples to help mitigate the influence from the e-n dipolar interaction. The Fermi-contact shift and e-n dipolar broadening can also be reduced at higher temperatures.

2.6 Bond Pathway Approach

The interpretation of the Fermi-contact shift is essential since it dominates the spectra of samples containing paramagnetic ions. To a very good approximation, the Fermi-contact shift contributions for an ion with each paramagnetic ion in the vicinity can be considered separately, meaning that the overall shift is additive.⁶⁰ The sign and magnitude of the spin density

transferred to the nucleus ($\rho^{\alpha\beta}(\mathbf{R}_N)$) is determined by the symmetry of the transition metal (TM) orbital, where the unpaired spins are located and also the angle of TM-O-Li bond. LiNiO_2 possesses a layered structure that can be regarded as a cation-ordered rocksalt structure and all the atoms are in an environment of octahedral coordination. Therefore, two main spin transfer pathways exist for Li: a nearest cation neighbor pathway (via a ca 90° TM-O-Li bond) and a next-nearest cation neighbor pathway (via a ca. 180° TM-O-Li bond) (**Figure 2.3**). The bond angle is determined by the bridging oxygen atoms. The 90° pathway occurs via two different oxygens, but they are typically treated as a single pathway for convenience. In the layered structure of LiNiO_2 , each lithium ion in Li layers is surrounded by a total of six 90° TM neighbours and six 180° TM neighbours. Although Li has also neighbours within the Li layer with 90° pathways, it is believed that all these Li-Li bonds contain no unpaired spins and can typically be ignored.

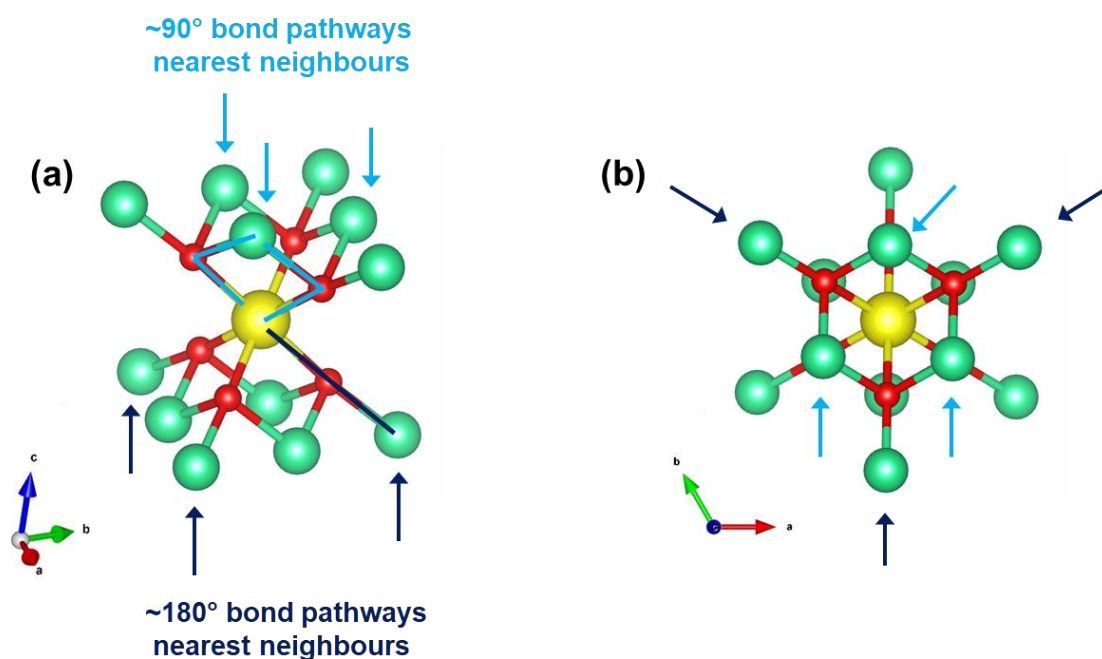


Figure 2.3 (a) Illustration of the coordination environment of a Li in the Li layer in LiNiO_2 . There are 6 nearest cation neighbours (3 above and 3 below) which can transfer unpaired spin density to Li via Ni-O-Li 90° bonds (sky blue arrows). There are 6 next nearest cation neighbours (3 above and 3 below) which can transfer unpaired spin density to Li via Ni-O-Li 180° bonds (dark blue arrows). (b) shows the view perpendicular to the layer.

The size and sign of the spin transfer from the TM centres can be understood from the effect of unpaired spins on the TM-O-Li hybrid orbitals. Two main mechanisms exist: delocalization

and polarization. Regarding delocalization, the orbital containing the unpaired spin belongs to the TM-O-Li hybrid orbital, hence the alignment with the B_0 field is delocalized over the entire orbital. Net positive spin transfer is experienced for the probed nucleus. For polarization, the unpaired spin polarizes the TM-O-Li hybrid orbital rather than being part of it and the B_0 field is orthogonal to the unpaired spins via exchange interaction. Compared to the delocalization, for the same spin, the electron takes more time in the TM-O-Li hybrid orbital in order to interact with the TM nucleus. A net negative spin is experienced by the rest of the orbital.⁵⁹ Polarization mechanism induces small negative shifts, while delocalization often leads to larger positive shifts. The TM species, including its electron configuration and the bonding geometry, determine which mechanism takes effect. The bond pathway contribution has been measured experimentally⁶¹ and can be determined by first principle calculation.⁶²

Chapter 3 New Insights into Lithium Hopping and Ordering in LiNiO₂ Cathodes

3.1 Introduction

As introduced in the 1st chapter, there is a symmetry reduction, i.e. from hexagonal (H) to monoclinic (M), which occurs for LiNiO₂ at compositions from $x \approx 0.75$ -0.4. The formation of such a phase was firstly attributed to the presence of JT active Ni³⁺ (electronic configuration of $t_{2g}^6 e_g^1$).⁶³ However, it is puzzling that the pristine LiNiO₂, which contains more JT active Ni³⁺ than partially delithiated materials, does not exhibit such a monoclinic distortion (different from NaNiO₂).²⁷ Such a distortion was also not observed in a XAS measurement.⁶⁴ Some Li/vacancy orderings were later discovered by electron diffraction. Some of these orderings were described for the monoclinic region.^{15,65} Theoretical calculations were also performed by Arroyo and Ceder.^{32,66,67} Their results reveal that the synergistic effects of a lithium/vacancy ordering and a cooperative JT distortion are driving the monoclinic distortion. In partially delithiated LiNiO₂ phases, non-negligible attractions occur between Li ions in different planes, especially between Li ions that are on the extensions of linear O-Ni-O bonds.^{68,69} Except for the short-ranged, repulsive, in-plane Li-Li interactions, such 180° Li_A-O-Ni³⁺-O-Li_B configurations provide extra stability (lower energy) (**Figure 3.1**). They are found in all calculated Li/vacancy ordering models. In addition, there is a JT-active Ni³⁺ centre in the long-ranged interplane 180° chains. The energy of anti-orbitals is lowered by the Li_A-O-Ni³⁺-O-Li_B configuration owing to the hybridization of Li-2s and O-2p orbitals. Such a decrease makes the orbitals to be preferentially filled, causing charge localization and therefore enhanced JT effects.^{32,59} Furthermore, the lining up of Li along one or two octahedral axes around Ni³⁺, but with vacancies along with the other one, provides a tremendously stable and JT distorted configuration.⁶⁶

Ordered Li/vacancy phases are found by Arroyo for $x = 1/4, 1/3, 2/5, 1/2,$ and $3/4$ in partially delithiated Li_xNiO₂. Orderings for $1/2$ and $3/4$ are well-investigated experimentally. $1/2$ corresponds to the structure with alternating rows of full and vacant Li sites, while for $3/4$ the foregoing empty row has alternating vacant and occupied Li sites.⁷⁰ Recently a stable structure of $5/8$ is discovered computationally, featuring a filled row of Li alternating with another row with one out of three occupied Li sites.³⁶ An interesting sequence $4/8 - 5/8 - 6/8$ can then be built for these three ordered phases. Stable structures of $1/4$ and $1/3$ were also observed by

electron diffraction. Although $2/5$ has never been reported experimentally, it marks the end of the monoclinic region and appears as a minimum in the dQ/dV curve. Interestingly, $1/4$ marks the end of the H2 phase region.

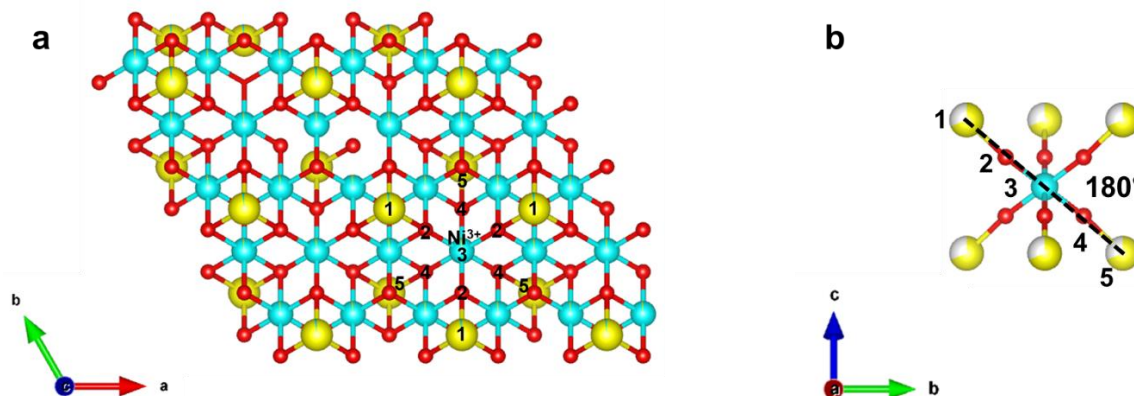


Figure 3.1 (a) The Li-vacancy arrangements in $\text{Li}_{0.25}\text{NiO}_2$ (based on the theoretical model in Reference).⁶⁶ The yellow spheres denote the lithium orderings and the blue and red spheres represent Ni and O atoms, respectively. Three $180^\circ \text{Li}_A\text{-O-Ni}^{3+}\text{-O-Li}_B$ configurations are labelled by numbers on atoms from 1 to 5 (for example, Ni^{3+} located in the centre of the chain are denoted by number 3). **(b)** The view of $180^\circ \text{Li}_A\text{-O-Ni}^{3+}\text{-O-Li}_B$ configurations from a direction.

Electron diffraction was frequently used to investigate the Li/vacancy ordering structure in early times because of its higher sensitivity to lithium. The Li/vacancy ordering can also be probed by solid-state nuclear magnetic resonance (ss-NMR) spectroscopy. As discussed in the last chapter, the Li NMR shift is dominated by the Fermi-contact interaction: the unpaired electron spin density of Ni^{3+} is transferred to the nuclear spin of interest (${}^6/{}^7\text{Li}$) through the intervening orbitals. The value of NMR shift can be interpreted through the bond pathway approach and connected to specific ordering structures. In this chapter, *ex situ* ${}^6\text{Li}$ and *in situ* ${}^7\text{Li}$ ss-NMR are performed to investigate the whole electrochemical delithiation/relithiation process of LiNiO_2 , focusing on the confirmation of the ordering structures. Other *in situ* characterization methods, such as XRD and XAS were also performed to investigate the correlation between phase transitions, ordering structures and electron/ionic hopping. The highly charged states are highlighted from the perspective of the Li/vacancy ordering.

3.2 Experimental

Synthesis of LiNiO₂: The precursor Ni(OH)₂ was obtained by the traditional precipitation process. Three solutions were prepared one by one: aqueous solution (A) 0.3 L of 2 M NiSO₄; (B) 0.3 L of 2 M NH₃ with 2 M NaOH; (C) 0.2 L of 2 M NaOH. 200 ml deionized water was first added to the 1.2 L reactor with 2 ml NH₃ in H₂O. Then the pH value was automatically adjusted to 10.7 by adding solution C. As soon as the pH value is steady, solutions A and B are added. The pumping speed was calculated so that the reaction could be finished in 18 h. The sediment was washed thoroughly with deionized water and dried in an oven at 80 °C overnight. Subsequently, LNO was synthesized by calcining the mixture of Ni(OH)₂ and LiOH·H₂O. The two components were ground using a mortar for 30 min and transferred to the oven. In pure oxygen atmosphere, the annealing temperature was firstly increased to 500 °C, kept constant for 6 hours, then further increased to 700 °C, and maintained for another 12 h. The sample was cooled down freely in the oven, which normally took 8-10 hours.

Electrochemical Characterization: The composite electrode was prepared by coating 92 wt% LNO, 4wt% C65 carbon black, and 4wt% polyvinylidene fluoride (PVdF) onto the Al foil with a thickness of 150 μm. The N-methylpyrrolidone (NMP) solvent was removed using the method introduced by J.R. Dahn (drying at 120 °C for 3 hours in air).⁷¹ The electrode was rolled and then cut into pellets with 1.2 cm diameter. The active material loading for each electrode was typically 12 mg cm⁻². Before testing, the electrodes were dried in vacuum at 120 °C overnight. The electrochemical performance was performed with coin-type half cells (CR2025). For battery assembly, lithium metal was used as anode and 50 μL 1.2 M LiPF₆ in ethylene carbonate-ethyl methyl carbonate (EC: EMC =3:7 by Vol %) with 2 wt% vinylene carbonate (VC) as electrolyte. For galvanostatic cycling, an electrochemical window between 2.8-4.3 V was chosen. The cells were firstly cycled at a rate of 0.1 C for 3 cycles and then at 0.5 C (1 C = 180 mA g⁻¹) for long-term cycling. All cells were tested using a VMP3 multi-channel potentiostat (Bio-Logic, France).

Morphological study: The morphology of the materials was characterized by a Zeiss Merlin scanning electron microscope using an acceleration voltage of 8 kV.

Ex situ NMR Sample Preparation: LNO/Li half cells were charged and discharged at 0.1 C rate. For the charged samples, certain states of charge (SoC) were reached by controlling the charging time, according to the specific capacity and current. Regarding the electrodes with

certain states of discharge (SoD), half cells were firstly charged to SoC of 85% and then discharged for a certain time (also calculated by the current and desired capacity). Once the cycling was finished, the cells were disassembled to take the cathodes out. Dimethyl carbonate (DMC) was used to wash the electrodes three times. Then LNO electrodes were dried naturally in the glovebox for 24 h and scraped from the Al current collectors and filled into the 1.3 mm diameter magic-angle spinning (MAS) NMR rotors.

In situ NMR battery assembly: The same cathode slurry as used for half cells was blade coated onto aluminum mesh strips. In the glovebox, the lithium metal was pressed onto copper mesh strips. A certain amount of electrolyte (here LP30 1.0 M LiPF₆ in ethylene carbonate-dimethyl carbonate (EC: DMC =1:1) by Vol % was used rather than the previous one used for long-term cycling) was dropped onto a glass fiber separator to get the separator fully wetted. The battery was closely encapsulated in polymer bags to ensure good contact between electrolyte and cathode/anode.

Solid-state NMR experiments: All NMR experiments were performed on a 4.7 T Bruker Avance 200 MHz spectrometer. For the *ex situ* MAS NMR experiments, the spectra were acquired using 1.3 mm rotors at a MAS frequency of 60 kHz. The recycle delay was set to 1 s and the Larmor frequency was 29.5 MHz for ⁶Li. ⁶Li MAS NMR spectra were measured using a rotor-synchronized Hahn-echo pulse sequence (90°-τ-180°-τ-acquisition) with a 90° pulse length of 0.95 μs. The ⁶Li NMR shifts were referenced externally using an aqueous 1M ⁶LiCl solution (0 ppm). All spectra were normalized with respect to sample mass and number of scans. The temperatures of the rotors during spinning were calibrated using the shift of ²⁰⁷Pb in Pb(NO₃)₂.⁷² The spectra of Pb(NO₃)₂ can be found in **Figure 3.2**. Each ²⁰⁷Pb MAS NMR spectrum was measured with 64 scans (1160 scans for static (room temperature) measurement) with a 90° pulse length of 2.8 μs and a relaxation delay of 40 s. We allowed approximately 15 min for rotors to have a stable temperature before the measurement. We used the linear equation ($\delta = T \cdot 0.753 \text{ ppm}/^\circ\text{C}$) to calculate the temperature difference for different spinning speeds.⁷² For the static (room temperature) measurement, the isotropic shift was derived from a fit with chemical shift anisotropy $\eta = 0.14$. An increase of 5 kHz corresponds to a temperature change of about 5 °C. The paramagnetic shift of delithiated/relithiated LNO is several hundreds of ppm and proportional to 1/T, so there is only a minor influence of the temperature. For the variable temperature (VT) NMR measurement, 2.5 mm rotors were used with smaller spinning speed. This means the influence from temperature is even smaller than for the *ex situ* NMR measurements.

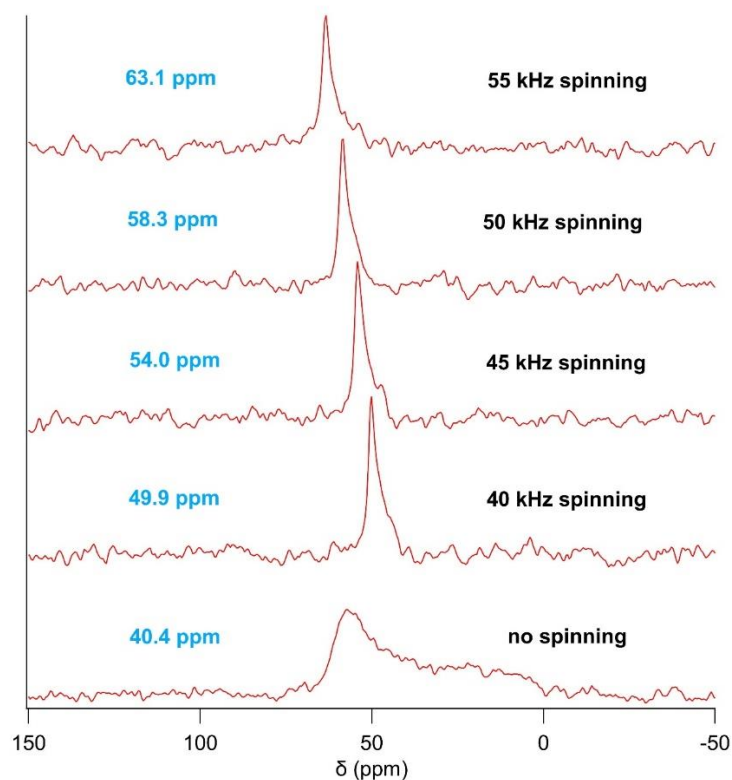


Figure 3.2 ^{207}Pb MAS NMR spectra of $\text{Pb}(\text{NO}_3)_2$ as a function of spinning speed.

Variable temperature (VT) ^7Li NMR spectra were acquired with 2.5 mm rotors at 30 kHz using a Hahn-echo sequence with a 90° pulse length of $1.9 \mu\text{s}$ and a relaxation delay of 1s. 900 scans were collected for each spectrum. For the *in situ* NMR measurement, ^7Li NMR spectra were collected at a Larmor frequency of 77.8 MHz without spinning. A Hahn-echo sequence was used with a 90° pulse length of $2.57 \mu\text{s}$, i.e. a radiofrequency strength of 97.3 kHz. The tailor-made “pouch cell” could be exactly placed into the flat RF coil. The measurement duration of each spectrum was 1 hour (3600 scans with 1s for the recycle delay). The ^7Li T1 relaxation time of LNO was measured using an inversion-recovery sequence and a value of 4.4 ms is obtained at room temperature. To determine the chemical shifts of each component inside the battery, the spectra of Li metal, electrolyte, and LNO cathode were measured separately also in the “pouch cell”. The *in situ* cell was cycled at a rate of 0.05 C between 2.8 - 4.7 V in order to also monitor the data in highly charged states.

Synchrotron radiation diffraction and X-ray absorption spectroscopy: The crystallographic structure of LNO was characterized by high-resolution synchrotron radiation diffraction (SRD) with a photon energy of 60 keV ($\lambda = 0.2072 \text{ \AA}$) at beamline P02.1, storage ring PETRA-III at DESY (Deutsches Elektronensynchrotron) in Hamburg, Germany. *In situ* SRD experiments were done at the MSPD beamline at ALBA synchrotron with an energy of 30 keV ($\lambda = 0.4130 \text{ \AA}$). The diffraction patterns were acquired using a MYTHEN 2D position sensitive detector. The exposure time for each pattern was 60 seconds. CR2025 coin cells with glass windows (diameter = 5 mm) were used.⁷³ The structural parameters were refined against the diffraction pattern using the Fullprof software. The LaB₆ standard packed in one coin cell was used for calibration. *In situ* X-ray absorption spectroscopy (XAS) was performed at beamline P65 at PETRA III, Germany. Electrochemical cycling was conducted in 2025-type coin cells with 5 mm-diameter Kapton window in the voltage range of 2.8-4.7 V. XAS spectra at the Ni K-edge (8.3 keV) were recorded in continuous XAS (6 min/spectrum) mode in transmission geometry using a Si (111) double crystal monochromator to modulate the incoming photon energy and a beam size of $0.3 \times 1.5 \text{ mm}^2$. All the XAS spectra were analysed and processed utilizing the ATHENA software package.

Galvanostatic intermittent titration technique (GITT): Regarding the GITT measurement, short pulses with a certain current were applied to the cell with a resting time of 4 h inserted after each pulse. The voltage/time profile is displayed in **Figure 3.3a**. A typical process containing one pulse and rest period is shown in **Figure 3.3b**. The diffusion coefficient could be calculated based on the following equation:⁷⁴

$$D_s = \frac{4}{\pi} \left(\frac{IV_m}{FS} \right)^2 \left(\frac{dU^\circ/dy}{dV/d\sqrt{t}} \right)^2, t \ll R^2/D_s \quad (3.1)$$

where I represents the current value for the short pulse, F represents Faraday's constant, V_m is the molar volume of the LNO active material, S represents the composite electrode active area, U° is the LNO open circuit potential at the end of each rest period, y is state of charge (SoC), V and t are voltage and time during pulse periods, respectively, and R is the diffusion length. Specifically, Verma's method was applied and will not be simplified.⁷⁴ A polynomial function was used to fit the open circuit potential data points (**Figure 3.3c**). Then values were obtained by differentiation of the fitting data (**Figure 3.3d**). **Figure 3.3e** displays the curve for a single current pulse. After a certain threshold time due to the over-potential, a highly linear trend was

observed and was determined from the slope of the fitting curve. Instead of giving the absolute diffusion coefficients, $D_s S^2 / V_m^2$ was calculated since the molar volume (V_m) and active surface area (S) are challenging to obtain.

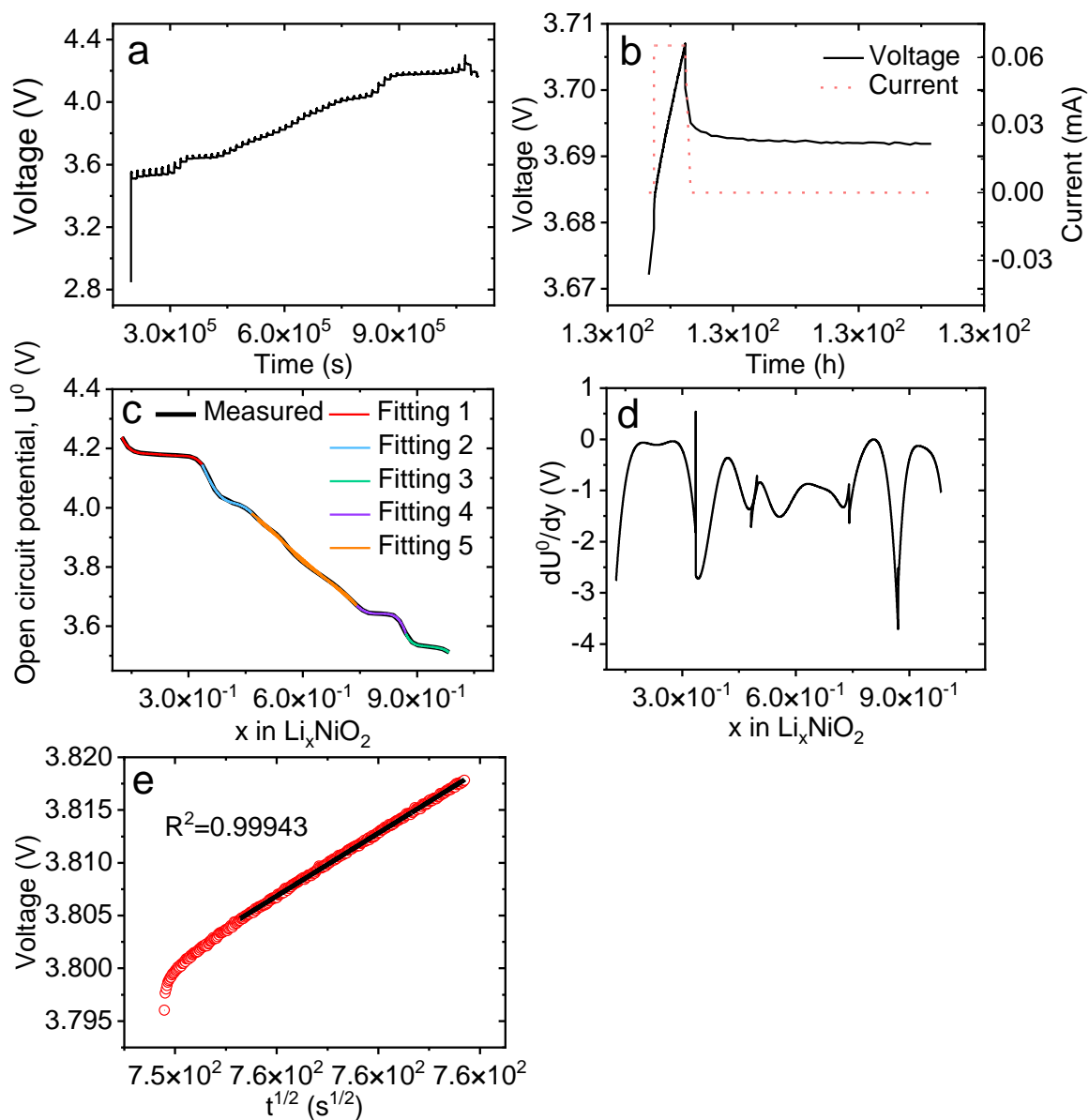


Figure 3.3 (a) The voltage-time profile obtained from GITT on LNO/Li half-cells. (b) Voltage and current as a function of time for a typical pulse-rest step acquired during GITT. (c) Open circuit potential (U^0) of LNO as a function of Li content determined from GITT with several polynomial fits. (d) Derivative of equilibrium potential as a function of Li content, derived from GITT. (e) Voltage as a function of square root of time for a single pulse duration with the corresponding linear fit. R^2 is 0.99943 for this fit and for most of the fitting R^2 values are larger than 0.99.

Building up the Li/vacancy ordering structures: The Li/vacancy ordering patterns described by Arroyo were used to create several structural models.⁶⁶ In their ordering schemes, only one Ni layer and adjacent two Li layers were given. Therefore, in order to determine the number of Ni³⁺ and Ni⁴⁺ surrounding Li, one Li layer and one Ni layer were further created. The construction is based on the oxygen packing of O3-type structure (AB CA BC sequence). When the models were constructed, two different Ni³⁺-O-Li arrangements (90° and 180° Ni-O-Li configuration) can be found and the corresponding shifts can be calculated as a sum of contributions from each Li-O-Ni³⁺ bond based on values given by previous papers.⁷⁵

3.3 Results and discussion

3.3.1 Structural and morphological characterization

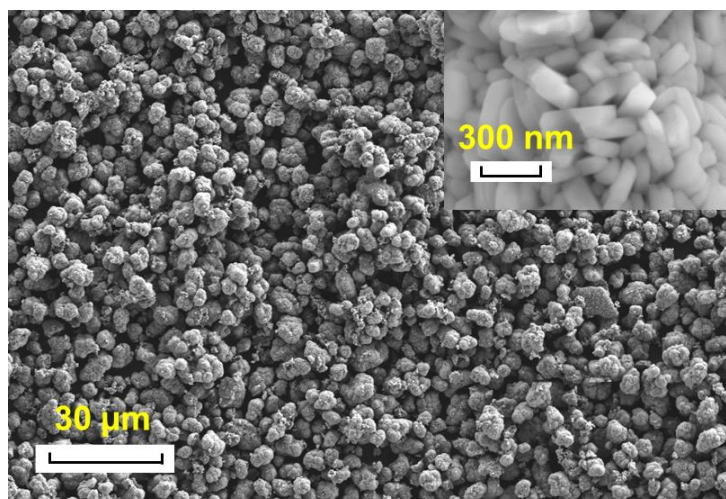


Figure 3.4 SEM image of LiNiO₂

The Precipitation and calcination method mentioned above is used for the synthesis of LNO. **Figure 3.4** shows the morphology of the LNO particles. Each secondary particle consists of large number of primary particles, which have a diameter of several hundred nanometres.

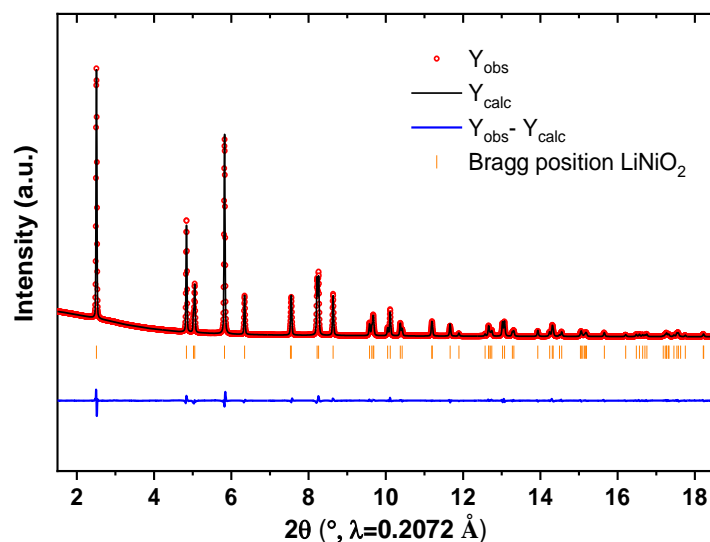


Figure 3.5 Rietveld refinement of LNO based on synchrotron diffraction pattern.

Figure 3.5 displays the Rietveld refinement of LNO based on synchrotron diffraction data. All reflections could be indexed on a layered hexagonal phase crystallized in space group $R\bar{3}m$. There is no impurity phase detected in this sample. The results of Rietveld refinement (**Table 3.1**) indicate that the degree of Ni/Li exchange is about 3%. Notice that a value of χ^2 smaller than 1 happens herein because Fullprof refines a structural model against XRD data having a low and noise-free background: it is known that most of the refinement programs like Fullprof, TOPAS, etc. result in χ^2 which is lower than 1. The degree of mixing has a profound effect on the structure and electrochemical characteristics.^{76,77} The real phase transition route of LNO can only be observed when the mixing value is smaller than 6%. Higher mixing value can lead to the disappearance of monoclinic distortion and the maintenance of the hexagonal cell on delithation.⁷⁷

Table 3.1 Detailed information about the refinement against the XRD data

LiNiO₂						
$R\bar{3}m$						
a = 2.876602			R _{Bragg} = 2.49		$\chi^2 = 0.8913$	
c = 14.194903			R _{wp} = 7.70			
Atom	Wyckoff position	Atomic position			SOF	B _{iso}
		x/a	y/b	z/c		
O	6c	0	0	0.2420(7)	1	0.69(3)
Ni	3b	0	0	0.5	0.969(7)	0.20(5)
Li	3a	0	0	0	0.969(7)	1.32(5)
Ni	3a	0	0	0	0.030(4)	1.32(5)
Li	3b	0	0	0.5	0.030(4)	0.20(5)

The electrochemical performance was evaluated by galvanostatic cycling of the LNO cathode in a CR2025 coin-type half-cell in the potential range of 2.8 to 4.3V vs Li⁺/Li. For the first three formation cycles, the cell was cycled at a rate of 0.1 C and the voltage-capacity curves for the first two cycles are shown in **Figure 3.6a**. The Coulombic efficiency is 89.2% and 96.2% for the 1st and 2nd cycle, respectively, both values are consistent with previous reports.⁷⁸ LNO has a high charge capacity of 257.8 mAh g⁻¹ and a discharge capacity of 230.6 mAh g⁻¹, which is one of the highest capacities of layered cathode materials. The difference between the first two cycles can be analysed using the differential capacity curve (dQ/dV vs. V) as a function of voltage (**Figure 3.6b**). Firstly, according to Ohzuku's report, all peaks fit well to the reported phase transitions.⁷⁹ A strong peak for the H1-M phase transition is found for the 1st charging process, which overlaps with the first process (the single-phase H1 delithiation). This result is consistent with findings from J. R. Dahn who observed sharp and narrow peaks in the dQ/dV curve during the 1st discharge and subsequent cycles.²⁷ Initially, the slow Li migration makes the two peaks move to higher potentials and overlap with each other. Subsequently, the peaks in the 2nd cycle occur at lower potentials for the charge and at higher potentials for the discharge process compared to the 1st cycle. The areas for each peak in the 2nd cycle are also larger than those of the 1st cycle, suggesting an increasing electrode activity. In order to determine the long-term cycling performance, the cell is measured at a rate of 0.5 C for 100 cycles (**Figure 3.7**). The performance is comparable to the reported results in the literature.^{80,81} As described in previous reports, the abrupt change in *c* lattice parameter during the H2-H3 transition leads to severe structural damage and pulverization of particles,⁸² resulting in a large irreversible capacity loss (here 67.8 mAh g⁻¹ after 100 cycles, **Figure 3.7**).

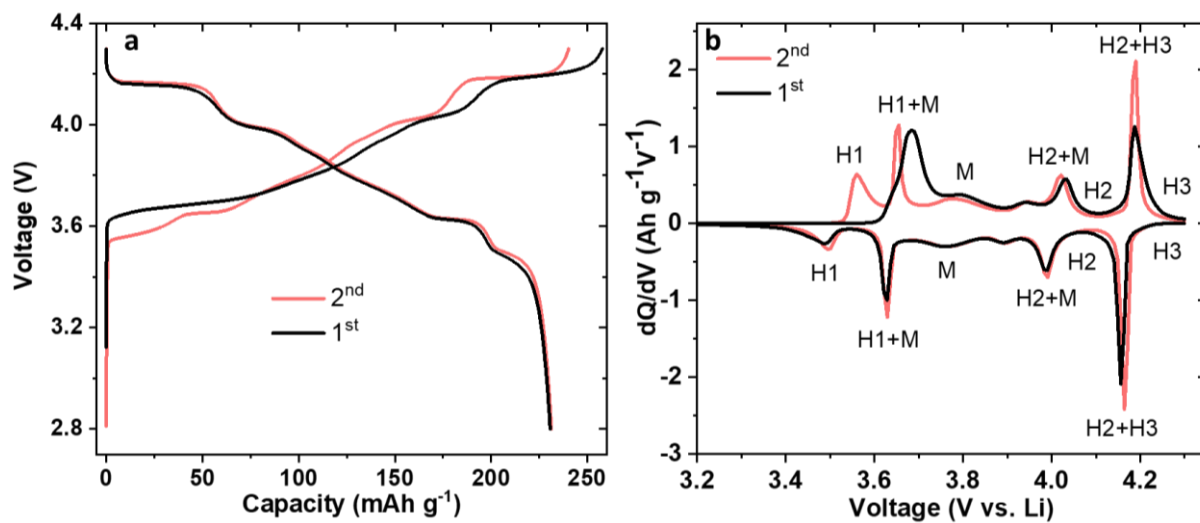


Figure 3.6 (a) Voltage profiles for the first and second galvanostatic charge and discharge cycles of an LNO/Li half-cell and (b) the corresponding differential capacity (dQ/dV) plot with phase compositions being labelled.

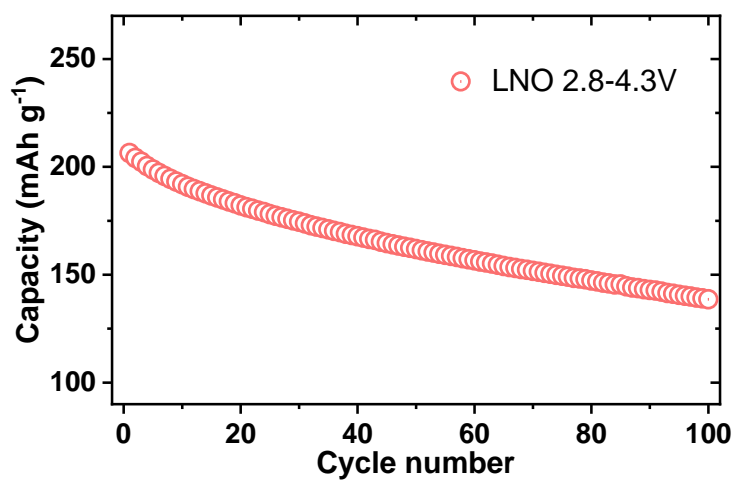


Figure 3.7 The cycling performance of LNO half-cell at a rate of 0.5 C

3.3.2 In situ XRD

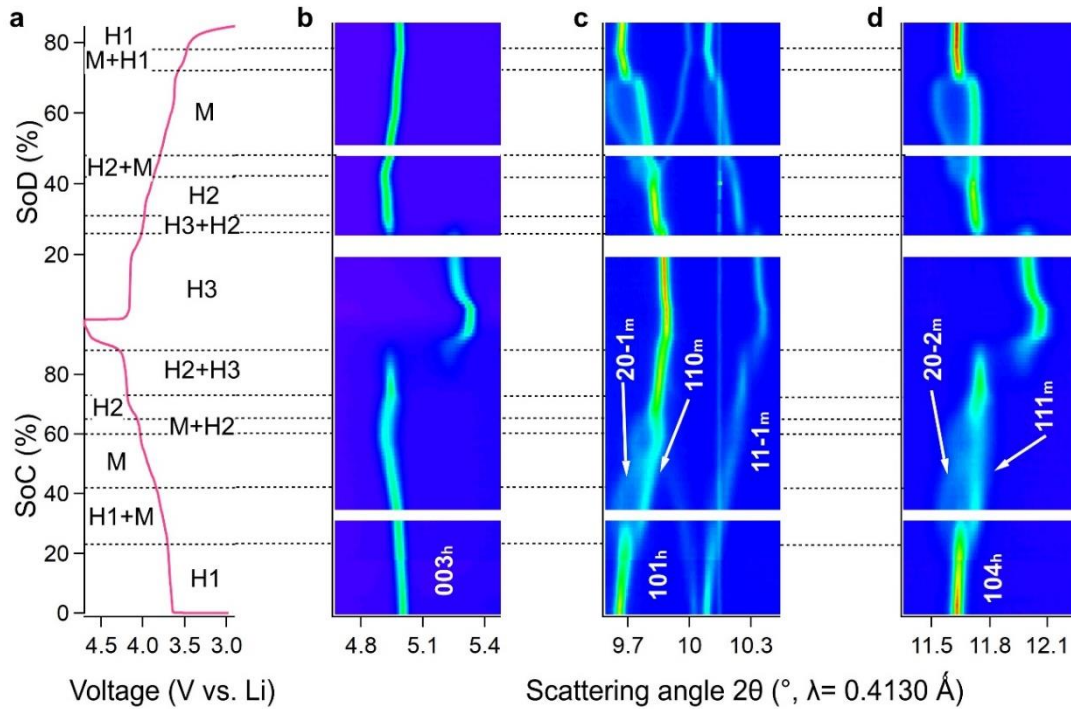


Figure 3.8 Contour maps of in situ synchrotron diffraction of LNO collected during the first cycle. **(a)** Cell voltage as a function of state of charge or discharge of the 1st cycle, which is aligned with the diffraction patterns; XRD patterns of selected scattering angle regions: **(b)** 4.68°-5.48°, **(c)** 9.59°-10.45° and **(d)** 11.36°-12.26°. Based on the refinement results, the phases in each region are labelled in **(a)**. The peak splitting for phase M is also indicated in **(c)** and **(d)**.

In situ XRD of LNO during the 1st cycle is recorded to determine the phase transitions. The cell voltage as a function of time aligned with the corresponding diffraction patterns is shown in **Figure 3.8**. Three selected regions of scattering angle are also displayed. At the initial stage of charge, all the reflections could be indexed based on layered LNO. In the beginning of charging, the original layered structure is maintained until SoC of 23% is reached. Subsequently, the monoclinic (M) phase gradually appears. The intensity of the original 101 reflection decreases and two new reflections, $20\bar{1}$ and 110, assigned to the M phase (space group $C2/m$) increase in intensity.²⁹ A similar behaviour is observed for the 104_h reflection, where $20\bar{2}_m$ and 111_m reflections gradually replace the original single reflection. This two-phase region exists between SoC 23% to 42%. The monoclinic structure can be derived from the original hexagonal lattice.

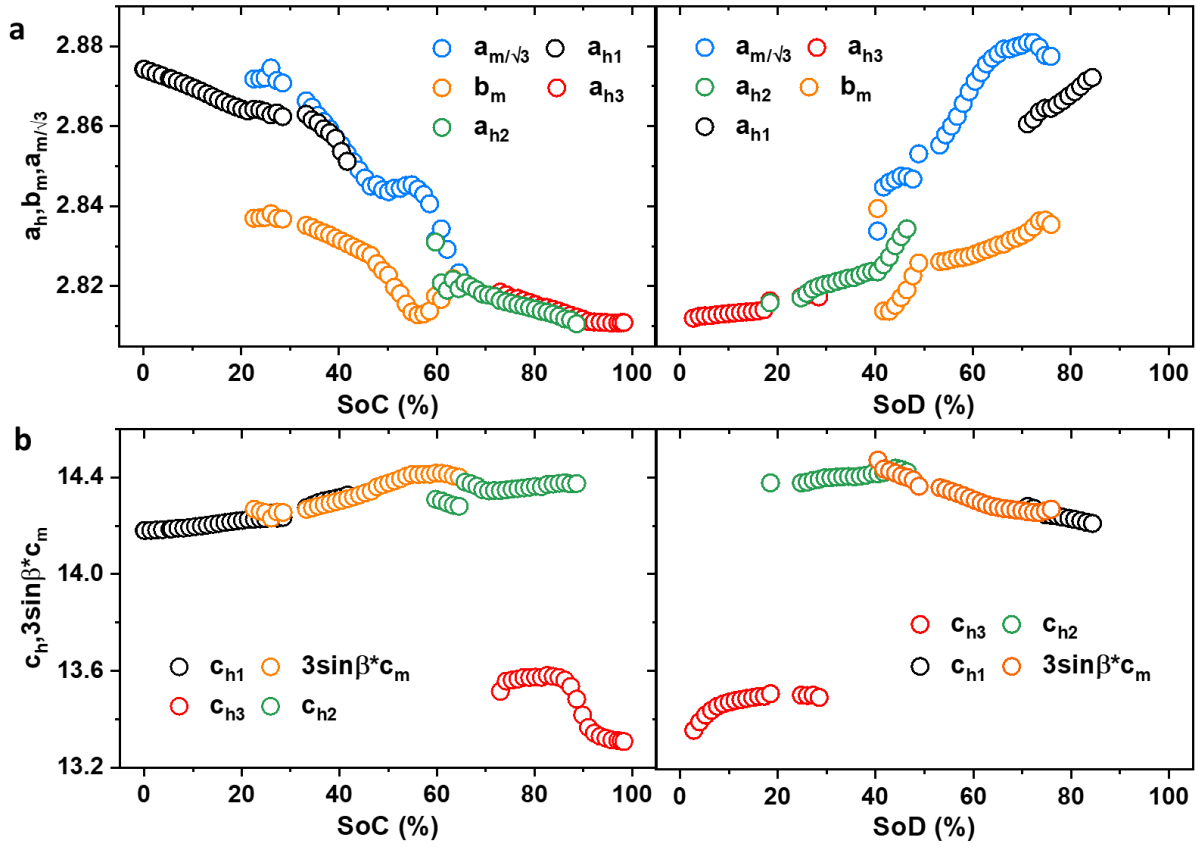


Figure 3.9 (a) Lattice parameters a_h , b_m , $a_m/\sqrt{3}$ and (b) c_h , $3\sin\beta \cdot c_m$ as a function of state of charge and discharge. The parameters belonging to the M phase are transformed to the hexagonal cell's system in order to evaluate the degree of distortion.

There is a certain relationship between the lattice parameters of the two phases described by Ohzuku ($b_m = a_h = b_h$, $a_m = b_m$, and $c_m = 1/3 \cdot \sin\beta \cdot c_h$) when there is no distortion.⁷⁹ With this transformation, the degree of distortion for the M phase can be evaluated as shown in **Figure 3.9**. The distorted M phase shrinks strongly in b_m direction and expands slightly in a_m direction. After the phase co-existence region, the single M phase is distorted much more seriously (b_m decreases and a_m increases strongly) in the SoC region 42%-65% before converting to the single second hexagonal (H2) phase. Up to now, it is still not clear why the M phase appears over such a long period during charging. The synergistic effects of lithium/vacancy ordering with JT distortion is the widely accepted theory.⁶⁶ During charging, the remaining lithium ions will rearrange and redistribute, forming certain stabilized ordering schemes. In these models the 180° $\text{Li}_A\text{-O-Ni-O-Li}_B$ configurations always exist with a JT-active Ni^{3+} centre. In Li_xNiO_2 , this certain Li distribution will lower the energy of e_g^* orbitals, since the hybridization of Li-O

orbitals allows e_g^* orbitals to be preferentially filled. Then the charge is localized at the Ni^{3+} and the JT effects are enhanced. Especially when there is a linear alignment of two Li vacancies with one Ni^{3+} site, the JT distortion is strong. For pristine LNO, there are no vacancies for enhancing the JT effect, so the undistorted hexagonal rather than the monoclinic phase appears. Beyond a certain point of SoC (60%), the remaining lithium cannot maintain enough of these special 180° configurations, so again a hexagonal (H2) phase appears. The peak splitting observed for the M phase disappears and single reflections reappear. With the lithium continually de-intercalated from the structure, the unit cell starts to contract dramatically in the c direction accompanied by appearance of another hexagonal phase (H3) at SoC of 73%. Two separate 003 reflections without any connection can clearly be observed in the XRD pattern. Up to now, the thermodynamic driving force for this structural collapse is still under discussion. One hypothesis is that the lithium/vacancy ordering still exists in some special configurations, which will stabilize this lithium-poor structure. However, no direct evidence to support this assumption is given up to now. At SoC of 88%, the whole structure changes to the H3 phase. Due to the high purity and low level of Li/Ni mixing, the *in situ* XRD cell could deliver a first charge capacity of 269.3 mAh g^{-1} (a composition of $\text{Li}_{0.02}\text{NiO}_2$ for the H3 phase). For the discharging process, LNO undergoes an inverse order of phase transitions compared to the charging process. The difference lies in the shorter periods with mixed phases, including H2+H3 and H1+M stages. This means that the transition processes are faster, smoother and kinetically easier. Moreover, when two states with same overall Li content during the charge and discharge processes are compared, the state during charging always possesses a higher amount of the Li-poorer phase, e.g. more H3 than H2. This could be attributed to some polarization and kinetic hysteresis.

3.3.3 Ex situ NMR

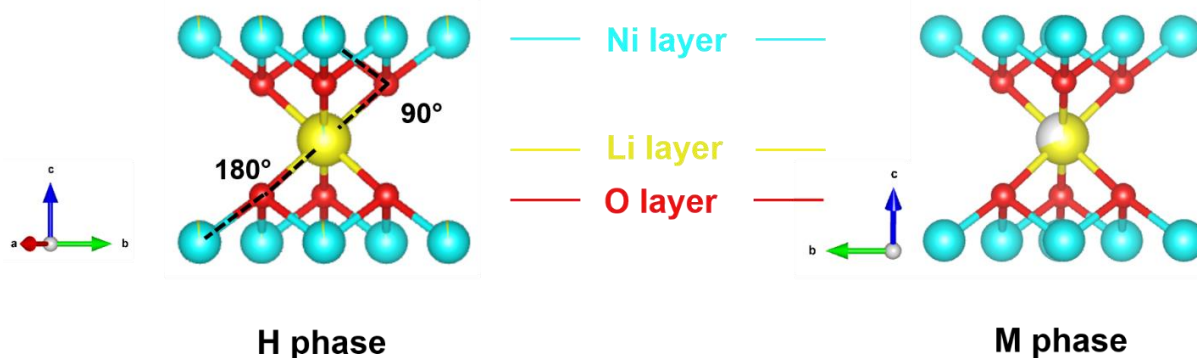


Figure 3.10 Illustration of the coordination environment of a Li-layer Li in LNO. There are 6 nearest cation neighbours which can transfer unpaired spin density to Li via Ni-O-Li 90° bonds. There are also 6 neighbouring cations which can transfer density via Ni-O-Li 180° bonds.

Solid state NMR is a useful tool to investigate the Li distribution or coordination environments.⁶¹ Li in a diamagnetic environment is normally associated with peaks with small shifts in the range ± 5 ppm. Larger ^{67}Li NMR shift can be caused by surrounding paramagnetic TM ions, mainly in the first cation coordination shell. The unpaired electron spin density from the TM ions will be transferred via oxygen to the 2s orbitals of Li, resulting in a so-called Fermi-contact interaction.⁵⁹ The magnitude of the NMR shift is determined by the symmetry of the TM orbitals and the angle of the Li-O-TM bonds. The coordination environment for Li in LNO is shown in **Figure 3.10**. The total Li NMR shift is the sum of hyperfine contributions from each paramagnetic neighbour.⁷⁵ To investigate the possible Li/vacancy ordering schemes with different phases confirmed by XRD, both *in situ* ^7Li and *ex situ* ^6Li NMR spectra were measured covering the full first galvanostatic cycle of LNO against Li metal. For the pristine material (**Figure 3.14**), a broad peak centred at around 700 ppm is observed.⁴⁷ This particular shift can be explained by the Li located in a pure Ni^{3+} environment. The substitution of Ni^{3+} by Ni^{2+} creates environments with larger or smaller values for the NMR shift. A small peak located at 425 ppm is ascribed to a Ni-rich rock-salt phase⁴⁷ and it was further verified by electron energy loss spectroscopy (**Figure 3.11**).³¹ On the particle surface, Ni ions are not fully oxidized to 3+, so the rock salt structure of NiO is retained without rhombohedral distortion. The small, narrow peak at 0 ppm is attributed to residues from the electrolyte salt or diamagnetic impurities such as LiOH/Li₂CO₃.

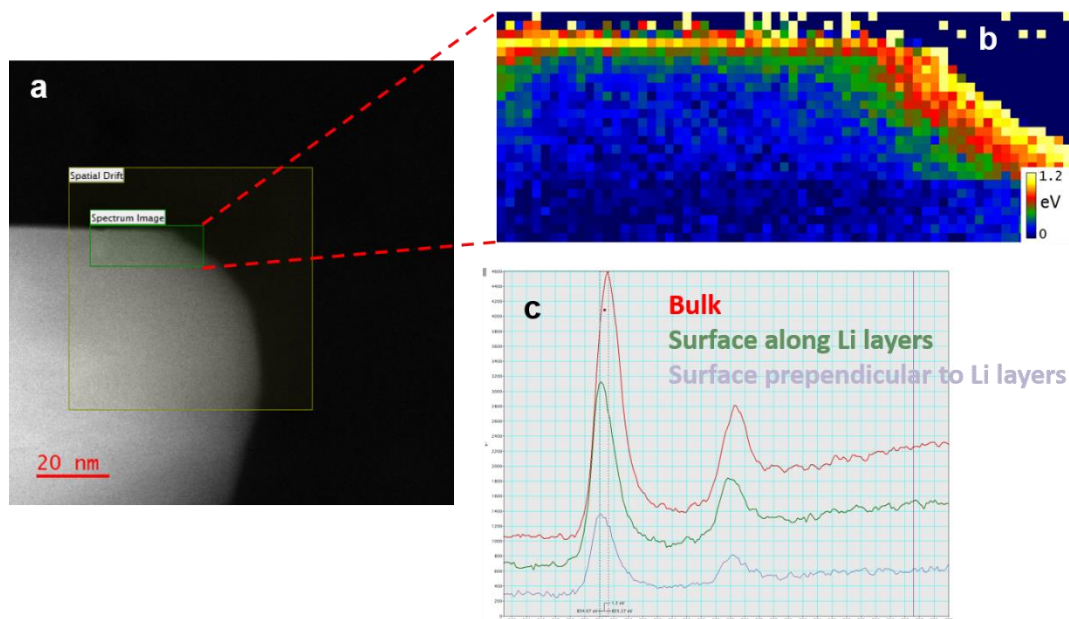


Figure 3.11 (a) STEM image of an LNO particle, (b) Ni L-edge chemical shift mapping of the green area in (a) and (c) corresponding EELS signals from different locations revealing a reduced oxidation state of Ni at the surface.³¹

In order to analyse the NMR data, several structural models were constructed based on the Li/vacancy ordering patterns provided by Arroyo et al.⁶⁷ (**Figure 3.12**). Corresponding Li orderings in the Li plane are also shown in another schematic diagram along the c axis direction.⁶⁷ The NMR shifts can then be estimated in these compositions, since the number of Ni^{3+} surrounding Li (90° and 180° Ni-O-Li configuration) is easily determined from these models. $\text{Li}_{0.5}\text{NiO}_2$ and $\text{Li}_{0.6}\text{NiO}_2$ were treated differently, since $\text{Ni}^{3.5+}$ ions are predicted to exist in these configurations. For each composition, two models were constructed regarding $\text{Ni}^{3.5+}$ ions as Ni^{3+} and Ni^{4+} separately (**Figure 3.13**). Multiple Li environments were found and only those having higher probability were chosen as calculated shifts (**Table 3.2, 3.3**). We chose average values from Ni^{3+} and Ni^{4+} models as the final estimated shifts. All the different Li environments and the corresponding shifts are summarized in **Table 3.4**.

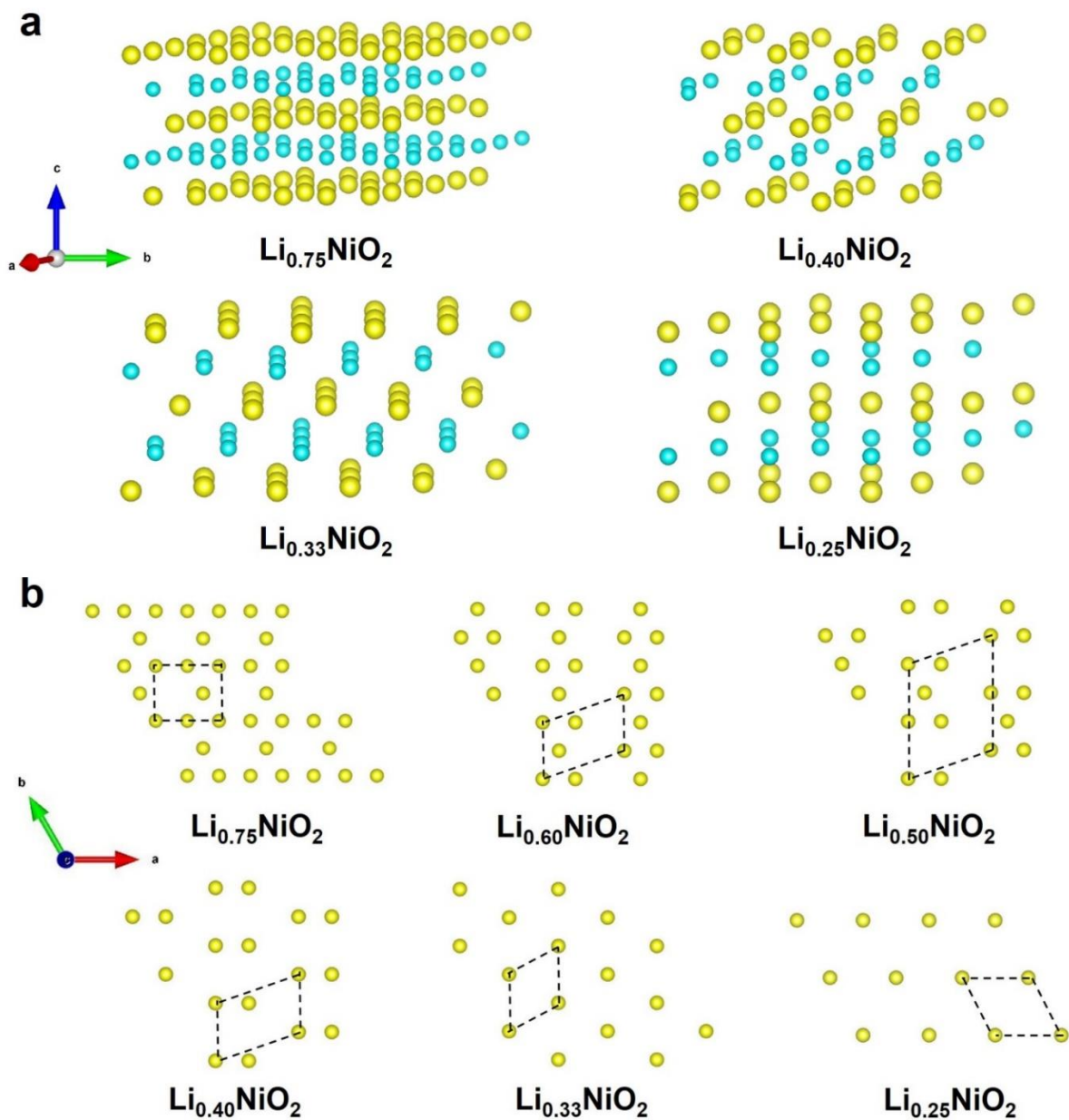


Figure 3.12 (a) Li/vacancy ordering schemes in Li_xNiO_2 at x values of 0.25, 0.33, 0.4, and 0.75. Only lithium and Ni^{3+} are shown without oxygen atoms and bonds. Models of $\text{Li}_{0.5}\text{NiO}_2$ and $\text{Li}_{0.6}\text{NiO}_2$ are shown in **Table 3.2, 3.3**. (b) Li layers of each composition with Li ordering along c axis direction.³¹

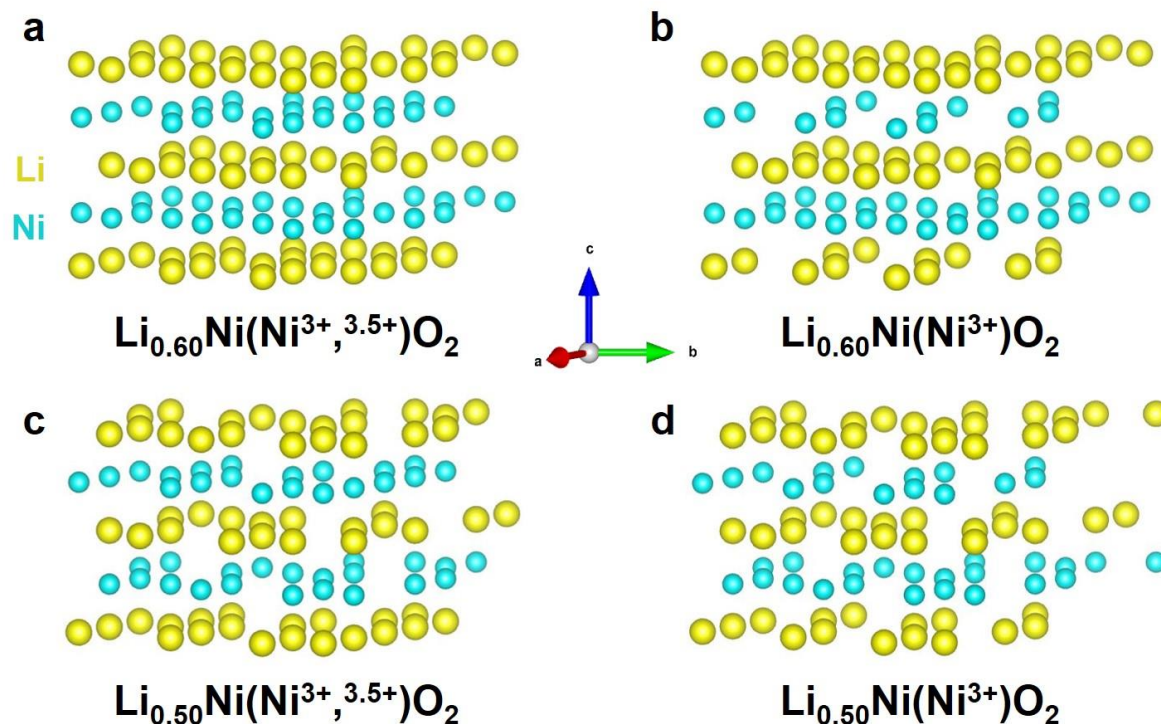


Figure 3.13 Li/vacancy orderings in Li_xNiO_2 at x values of 0.60 (a)(b) and 0.50 (c)(d). Oxygen atoms and bonds are not shown. In (a) and (c) the $\text{Ni}^{3.5+}$ ions are considered to be Ni^{3+} and in (b) and (d) the $\text{Ni}^{3.5+}$ ions are considered to be Ni^{4+} and are not shown in the figure.³¹

Table 3.2 Different Li environments in two models of $\text{Li}_{0.6}\text{NiO}_2$ when considering $\text{Ni}^{3.5+}$ ions as Ni^{3+} and Ni^{4+} separately.³¹

x in Li_xNiO_2	No. of Ni^{3+} surrounding Li		Probability	Calculated shifts (ppm)	Integrated value (ppm)
	90°	180°			
0.60 ($\text{Ni}^{3.5+}$ is believed to be Ni^{3+})	4	5	High	490	442
	3	4	low	395	
	5	3	low	255	
	5	2	low	145	
	4	2	low	160	
0.60 ($\text{Ni}^{3.5+}$ is believed to be Ni^{4+})	3	4	High	395	
	5	1	High	35	
	3	1	low	65	

Table 3.3 Different Li environments in two models of $\text{Li}_{0.5}\text{NiO}_2$ when considering $\text{Ni}^{3.5+}$ ions as Ni^{3+} and Ni^{4+} separately.³¹

x in Li_xNiO_2	No. of Ni^{3+} surrounding Li		Probability	Calculated shifts (ppm)	Integrated value (ppm)
	90°	180°			
0.50 ($\text{Ni}^{3.5+}$ is believed to be Ni^{3+})	3	4	High	395	395 410
	2	4	High	410	
	3	5	low	505	
	4	4	low	380	
	4	2	low	410	
	3	2	low	175	
	5	2	low	145	
0.50 ($\text{Ni}^{3.5+}$ is believed to be Ni^{4+})	2	5	low	520	395 410
	3	4	High	395	
	2	4	High	410	
	3	1	low	65	
	5	1	low	35	
	4	1	low	50	

Table 3.4 Comparison between the experimental and calculated shifts for the Li_xNiO_2 phases.

x in Li_xNiO_2	No. of Ni^{3+} surrounding Li		calculated shifts (ppm)	experimental shifts (ppm)
	90°	180°		
0.25	0	6	660	547.8
0.33	2	2	190	436.2
0.40	2	4	410	496.8
0.50			410,395	494.1
0.60			442	504.2
0.75	4	6	600 (2/3)	724.1
	5	3	255 (1/3)	

Table 3.5 Parameters of ${}^6\text{Li}$ NMR peaks in the *ex situ* measurement.

SoC (%)	Observed shifts (ppm)	Half-peak width (ppm)	Phase composition	SoD (%)	Observed shifts (ppm)	Half-peak width (ppm)	Phase composition
0%	698.7	111.8	H1				Not accurate
5%	667.0	115.5	H1	Full	698.9	91.1	H1
20%	724.1	261.4	H1	80%	492.2	44.2	H1
35%	504.2	141.2	H1+M	65%	611.3	231.1	M
50%	494.1	49.1	M	50%	488.4	52.5	M
60%	496.8	54.0	M+H2	40%	410.0	58.0	H2
65%	436.2	64.1	H2	35%	437.7	77.2	H3+H2
75%	547.8	103.2	H2+H3	25%	417.0	74.3	H3
80%	584.4	130.6	H2+H3	20%	418.8	70.1	H3
85%	565.6	91.5	H2+H3				

For the *ex situ* NMR experiments (**Figure 3.14**), the NMR shifts, phase compositions and peak half widths are summarized in **Table 3.5**. For each material, the isotropic NMR shifts were compared with the estimated shifts deduced from the ordering patterns as described above. As LNO is delithiated by only 5%, the spectrum is almost unchanged with only a slight peak shift to lower ppm values. This decrease in NMR shift corresponds to oxidation of 5% of Ni^{3+} to Ni^{4+} . Since Ni^{4+} has an electronic configuration $3d^6$, in an octahedral environment a low-spin configuration is adopted corresponding to a diamagnetic state. Therefore, there is no contribution of this Ni (now Ni^{4+}) neighbour to the overall NMR shift. From *in situ* XRD data, we could see that in this state the system is still in the single-phase H1 region and there are only few vacancies to facilitate lithium movement. Lithium rearrangement to form a lithium-ordered structure is not possible yet. In the following, at SoC 20%, a considerable NMR line broadening is observed. This is in contrast to earlier reports for NMC and NCA materials.^{75,83} After removing a certain amount of Li, the Li residence time will be shorter than the time scale of these NMR experiments (some ms). As a result, a time-averaged signal will be recorded after certain degree of charging that can result in narrowing of the NMR peak.^{75,83} However, our finding is in contrast to this trend. Looking back to the XRD data, the material is still in the H1 region at this stage. As reported earlier, Li/vacancy ordered structures are believed to exist between two-phase regions as suggested from DFT calculations.⁶⁶ $\text{Li}_{0.75}\text{NiO}_2$ is the composition that appears just before formation of the M phase. In this structure, there are short-range, repulsive, in plane Li-Li interactions and long-range interplane Li-O- Ni^{3+} -O-Li chains. The first interaction maintains the ordered distribution of Li and vacancies. The latter one lowers the energy of the structure and strengthens the Jahn-Teller effect of Ni^{3+} in the centre of this chain. Subsequently, the strong distortion results in the formation of the M phase.⁶⁶

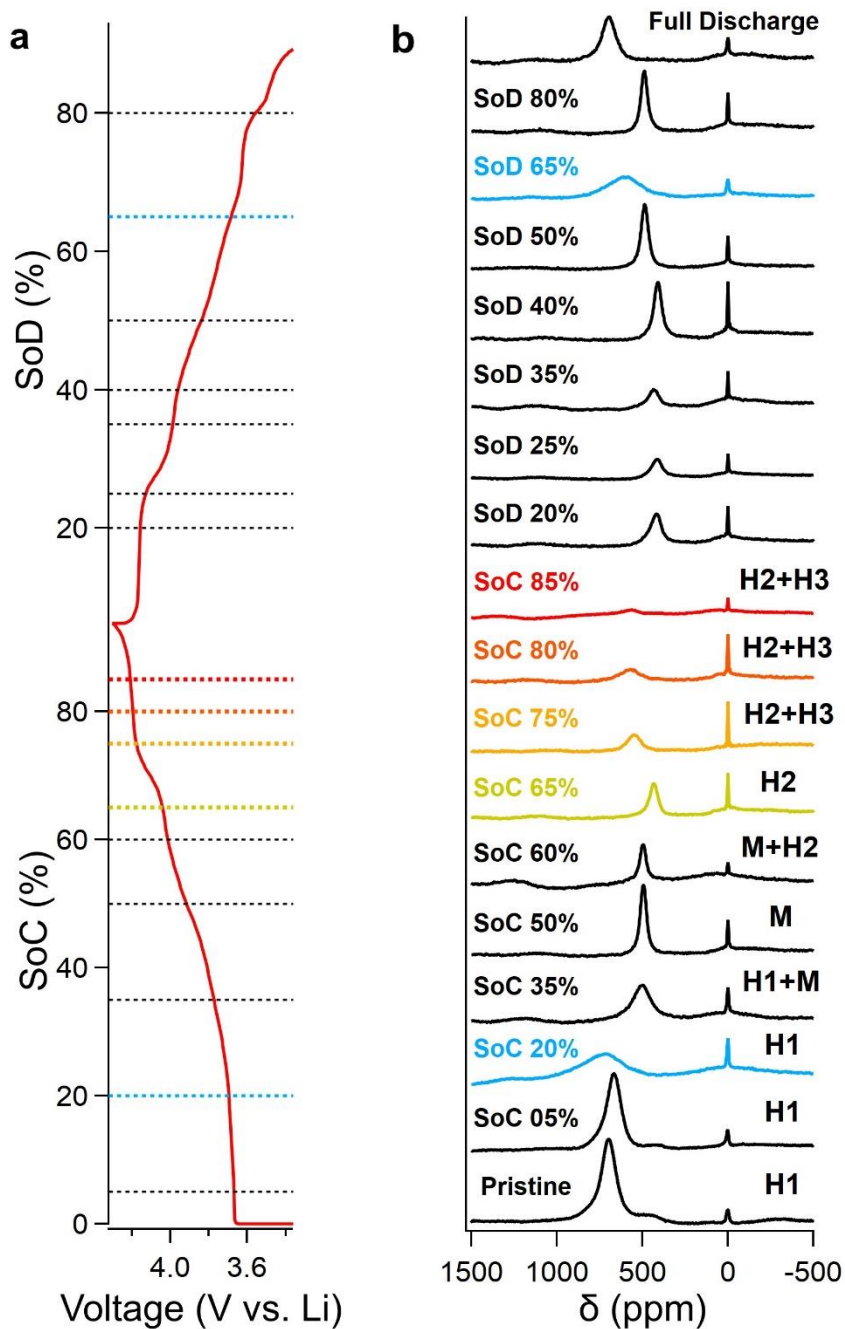


Figure 3.14 Ex situ ^6Li MAS NMR spectra. Cell voltage as a function of state of charge and discharge for the first galvanostatic cycle of an LNO half-cell, dashed lines indicate points where cells were disassembled for NMR experiments (a). ^6Li MAS NMR spectra of ex situ LNO cathode samples (b). Two regions of interest are labelled with coloured lines in both figures.³¹

For $\text{Li}_{0.75}\text{NiO}_2$, in our structural models two different environments for Li have been given inducing two different estimated NMR shifts. Only one signal is observed at 724.1 ppm. The difference between experiment and the majority calculated shift is not large and the reason might be slight differences in bond angles and distances, since the calculated shifts are based on the known shifts from Ni^{3+} in NCM811 material.⁷⁵ The actual distances and angles of bonds are probably different in the Li_xNiO_2 compounds. Moreover, the estimated shift is deduced from the structure of $\text{Li}_{0.75}\text{NiO}_2$, which is the only established pattern closest to our deintercalated sample ($\text{Li}_{0.80}\text{NiO}_2$). To further explore the reason of NMR peak broadening at SoC 20%, ^7Li MAS NMR spectra at variable temperatures (VT) were recorded for pristine LNO, $\text{Li}_{0.80}\text{NiO}_2$, and $\text{Li}_{0.50}\text{NiO}_2$ (**Figure 3.15**). For LNO and $\text{Li}_{0.80}\text{NiO}_2$, a continuous narrowing of the peaks occurs upon heating, because Li hopping among sites becomes much faster than the line width of the NMR peak (in kHz). Dipolar interaction is averaged and signals are motionally narrowed.⁸⁴ A decrease of paramagnetic susceptibility at high temperatures also induces shifting to lower (less positive) ppm values.⁸⁵ For VT spectra of pristine LNO and $\text{Li}_{0.50}\text{NiO}_2$, signals are already narrow at room temperature. However, the two signals of $\text{Li}_{0.80}\text{NiO}_2$ only start narrowing above 305 K. The slower exchange reveals that the movement of Li hopping is slow enough at room temperature, so that more different Li environments can be observed. Normally the rate of Li hopping in the pristine state should be smaller than that of $\text{Li}_{0.80}\text{NiO}_2$ because of the increased number of lithium vacancies and larger interlayer spacing in $\text{LiNi}_{0.80}\text{O}_2$. In this case, the appearance of Li/vacancy ordering ($\text{Li}_{0.75}\text{NiO}_2$) strengthens the Jahn-Teller effect, and thus the original layered structure is distorted and hopping rate is decreased. Furthermore, SoC 20% corresponds to the state just before the Li/vacancy ordered structure ($\text{Li}_{0.75}\text{NiO}_2$) appears. The structural distortion also results in a broader distribution of local environments around the Li ions compared to that of the pristine structure, further contributing to the broadening of signals.

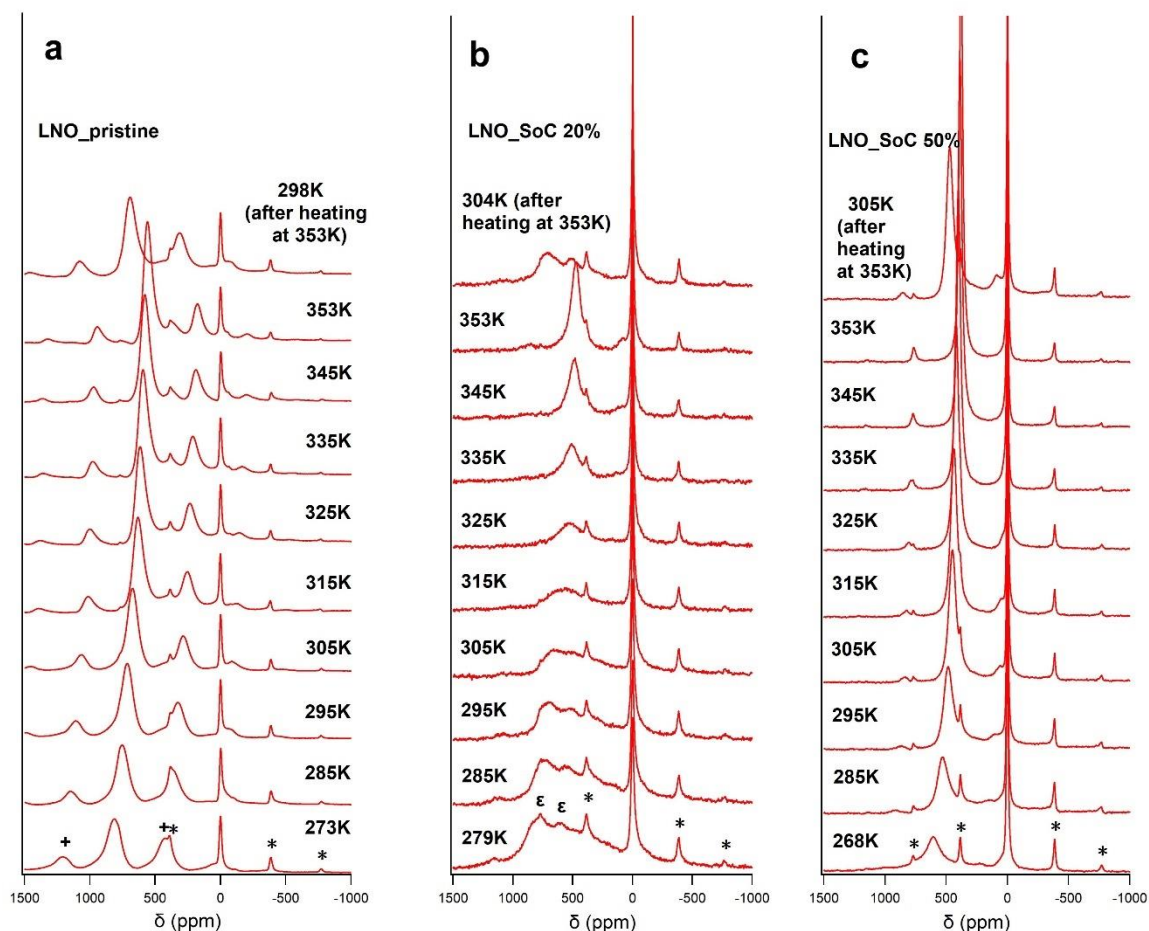


Figure 3.15 Variable temperature ${}^7\text{Li}$ solid-state NMR spectra of LNO at three different states: (a) pristine LNO, (b) $\text{Li}_{0.80}\text{NiO}_2$, and (c) $\text{Li}_{0.50}\text{NiO}_2$. Asterisks (*) and plus (+) signs indicate the position of spinning sidebands. Note that for $\text{Li}_{0.80}\text{NiO}_2$ two signals were detected in contrast to the single signal in *ex situ* NMR data. (cf. **Figure 3.14**; this might be caused by the faster spinning used in the *ex situ* measurements associated with a slightly enhanced temperature), but the broadening and position of the signal look the same.

When the SoC reaches 35%, the NMR peak becomes narrow again and moves to the lower ppm region. At this point, the monoclinic phase is already dominating (93%) and the presence of more lithium vacancies stimulates the Li hopping. The theoretical ordering model closest to this state is $\text{Li}_{0.6}\text{NiO}_2$. The calculated NMR shift is 442 ppm, which is not far away from the experimental value (504.2 ppm). For the SoC of 50%, the peak becomes even much narrower (**Table 3.5**), because now only the single M phase exists and, most important, a higher concentration of Li/vacancy exists. The observed shift (494.1 ppm) is close to the calculated value (395/410 ppm), indicating the appearance of Li/vacancy ordering. The VT NMR spectra

of $\text{Li}_{0.50}\text{NiO}_2$ are shown in **Figure 3.15c**. At lower temperatures such as 285 K, the signal of $\text{Li}_{0.50}\text{NiO}_2$ is slightly broader than that of pristine LNO. However, with increasing temperature the signal becomes much narrower, suggesting fast Li diffusion. For the next charged state (SoC 60%), the H2 phase begins to appear but with a very small content (7%). The third Li-ordered structure ($\text{Li}_{0.40}\text{NiO}_2$) before the appearance of the H2 phase exists before this state. The ordering pattern suggests 4 Ni^{3+} with 180° and 2 Ni^{3+} with 90° configuration. The estimated shift (410 ppm) is quite compatible with the experimental shift (496.8 ppm), indicating the formation of Li/vacancy ordering in this state. It should be noted that the large differences between experimental and calculated values are mainly caused by uncertainties in the calculations.⁶² The phase transition from M to H2 has reduced the Li ordering, as it can be seen from some slight broadening of the NMR peak (**Table 3.5**). The M phase undergoes severe changes in the lattice parameters before this point and starts to return back to a hexagonal phase (**Figure 3.9**). The following state with SoC 65% is the point where only the H2 phase exists. The peak keeps shifting to lower ppm positions, which reveals the further oxidation of Ni^{3+} to Ni^{4+} . The ordering model close to this charge stage is for $\text{Li}_{0.33}\text{NiO}_2$ with 2 Ni^{3+} with 180° and 2 Ni^{3+} with 90° configuration. The NMR shift is not compatible with the ordering structure, similar to the discovery by C. Delmas et al.⁷⁸ However, this ordering pattern has been proved experimentally by electron diffraction. One assumption for the disparity is that Li is surrounded by more Ni^{3+} ions with a 180° configuration. It is worth noting that for the previous three states (50%-65%), peaks just move to lower ppm locations step by step, in addition to the decreasing intensity as expected from the removal of Li. However, for the next spectrum at SoC 75%, the peak evidently moves to higher ppm locations. This back-shifting of ^6Li NMR peak positions for LNO is similar to that reported earlier for ^7Li NMR measurements, although in that case the higher magnetic field and the slower spinning obscured some of these details.¹⁴ It indicates that the local lithium environments in the H2 phase have changed drastically or, in other words, there are new ordered structures in this regime. Between SoC 65% and SoC 75%, there are also two reported lithium/vacancy ordering models ($\text{Li}_{0.33}\text{NiO}_2$ and $\text{Li}_{0.25}\text{NiO}_2$). Just like in the situation before the appearance of the M phase, new Li/vacancy orderings are formed before the phase transition. The difference of peak position between SoC 65% and SoC 75% is 117 ppm, which just corresponds to the chemical shift contribution of one Ni^{3+} -O-Li 180° bond.⁷⁵ So in order to form new ordered structures, Li ions are surrounded by one more Ni^{3+} at one of the nearest neighbouring metal sites. In the calculation model of $\text{Li}_{0.25}\text{NiO}_2$, each Li ion is surrounded by six Ni^{3+} ions with the 180° configuration. The observed shift is similar to the estimated value. The experimental shift increases upon Li deintercalation when the number of

Ni^{3+} decreases. Li remains surrounded by a given number of Ni^{3+} ions. This observation suggests an ordered $\text{Ni}^{3+}/\text{Ni}^{4+}$ arrangement around Li and coupled ionic and electronic hopping to realise such an arrangement. It is reported that the electrons could follow the movement of Li ions to change the oxidation state of locally coordinated Ni.⁷⁸ Such a special Li-ordered and $\text{Ni}^{3+}/\text{Ni}^{4+}$ -ordered structure appears to be the necessary preparation step for H3 formation, possibly facilitating the further deintercalation and providing enough stability. When the transition between H2 and H3 happens, there are no big changes in the NMR spectra of SoC 80% and SoC 85%, except for some slight broadening. At SoC 85%, the fraction of the H3 phase is already 77%. Although most of the Ni^{3+} is oxidized to Ni^{4+} at this point, the NMR peak position is still at a quite high value of about 565.6 ppm. This suggests that the remaining Ni^{3+} is located preferentially in the vicinity of the remaining Li ions. For the last three charge states (75%-80%-85%) it can be clearly seen that the peak position does not change but just the peak intensity is decreasing. This clearly shows that in this region we have a two-phase reaction where a Li-containing phase is replaced by a Li-poor phase. When the amount of the H3 phase increases, the lithium content in this H3 phase remains constant until the whole two-phase transition is finished. This could be verified by the constant c parameter of the H3 phase in the first part of this reaction step (**Figure 3.9b**). This means that no further Li de-intercalation from the H3 phase happens when the transformation from H2 to H3 is still ongoing.

In case that Li ions would be removed from H2 without phase transitions, more Ni-O-Li 180° bonds would disappear. Removing Ni-O-Li 180° bonds corresponds to disappearance of the $180^\circ \text{Li}_A\text{-O-Ni}^{3+}\text{-O-Li}_B$ chain configuration, which always ensures good stability of these structures. This extra stability prevents LNO from evolving into hybrid H1-3 structures or O1-type stacking faults as in LiCoO_2 .^{86,87} When the de-intercalation continues, the single H3 phase reveals a decreasing c parameter, indicating that vacancies are created and possibly Li hopping is needed again to establish the last Li/vacancy ordering. One should notice that there is no intermediate left shift of NMR peaks or enormous peak broadening in highly charged NCM or NCA phases,⁷⁵ since the additional elements (Co, Mn, Al) suppress the Jahn-Teller distortion and thus the phase transition H2 to H3.

For the discharging process, the NMR spectra suggest that it is not just the reversed process of charging. For same Li contents (like SoC 80% vs SoD 20%, i.e. $\text{Li}_{0.2}\text{NiO}_2$), peak shapes and locations are different. At SoD 20%, there is not the same lithium-ordered structure as that observed at SoC 80%. The phase composition obtained from XRD refinement may be different, since the *in situ* XRD cell was charged to a higher voltage of 4.7 V (SoC 98% is the final state)

and *ex situ* NMR cells were charged to SoC 85% only. As a result, the phase transition process for the *ex situ* NMR cells observed during discharging starts at slightly higher Li contents. Moreover, the phase transitions during the discharging are faster than those of the very first charging, as observed by a reduced polarization (cf. also **Fig. 3.6b**).²⁷ Furthermore, the O₂ evolution happening at high charging voltages can form a cubic phase at the particle surface, which can act as protection layer.⁸⁸ In short, all factors described above contribute to the faster phase transitions during discharging. The samples obtained at SoD 20%, 25%, and 35% may already be in the single H2 region. The samples at SoD 40% and 50% should be in the region of the single M phase. The NMR peak at SoD 50% has a larger NMR shift, indicating a state closer to the pristine state than for SoC 50%. Most evidently, the strong peak broadening caused by Li ordering/disordering also happens already at a lower Li-content at SoD 65% (cf. blue spectra in **Fig. 3.14**). At the end of discharge, the final state corresponds to the SoD of 86.8%, so the NMR intensity is smaller than that in the pristine state. Interestingly, the Ni-rich rock salt phase appearing in the pristine state does not appear at the end of discharge. It could be explained by the oxidation of Ni during Li de-lithiation, when the cubic phase is already transformed to a layered phase. The missing signal at 425 ppm in the spectra at SoC 20% and 30% supports this assumption.

3.3.4 In situ NMR

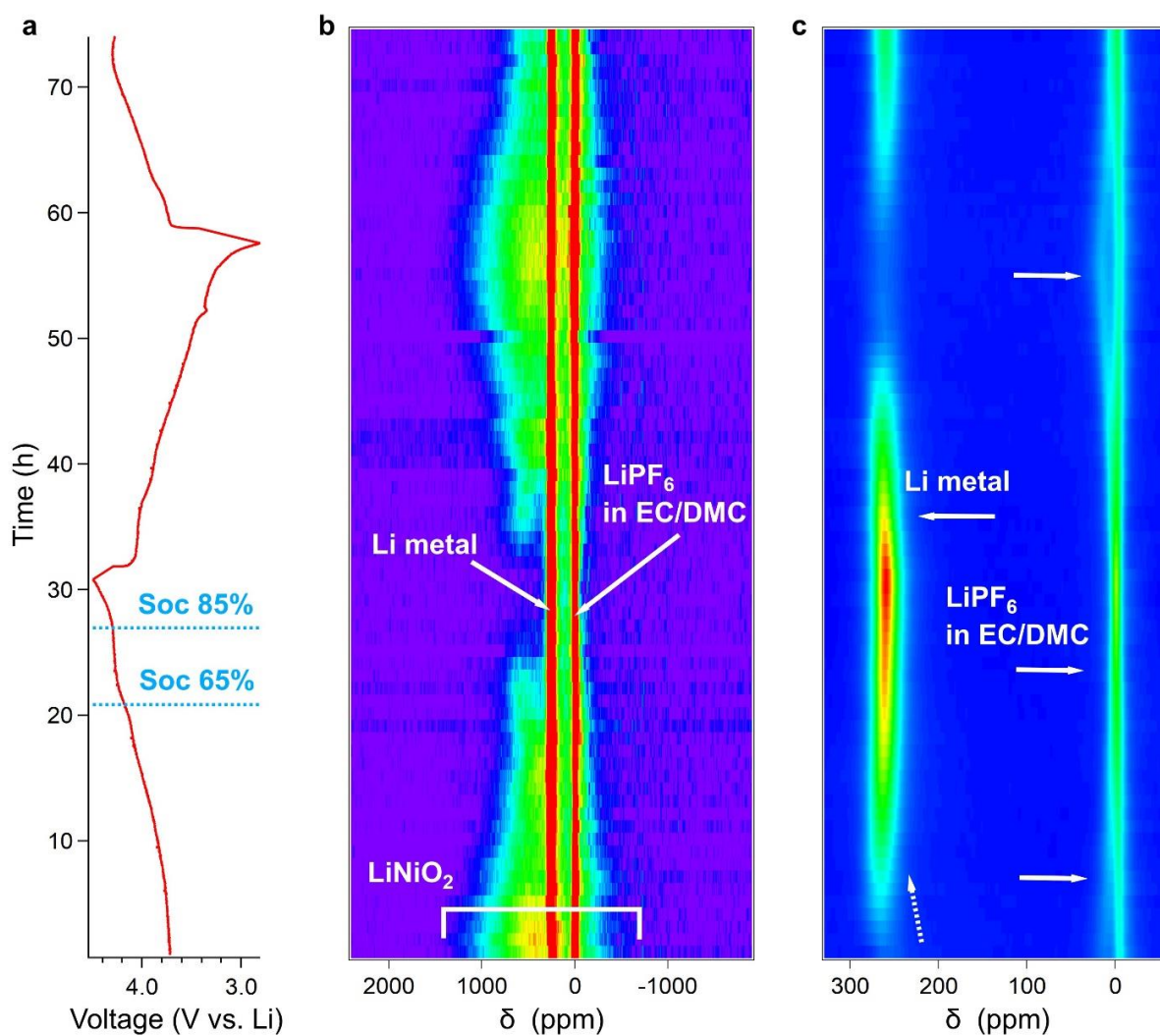


Figure 3.16 (a) Voltage profile and (b) contour plots of in situ ^7Li NMR data recorded on an LNO/Li half-cell during cycling between 2.8 to 4.7 V at a rate of 0.05 C. LNO, Li metal and electrolyte are separately labelled. The same behaviour of signal left shifting as in ex situ ^6Li NMR (Figure 3.14) is also found in the highly charged region which is also indicated in the voltage profile. (c) A magnified view of the range 330 - (-60) ppm is used to monitor the evolution of Li metal and electrolyte signals.

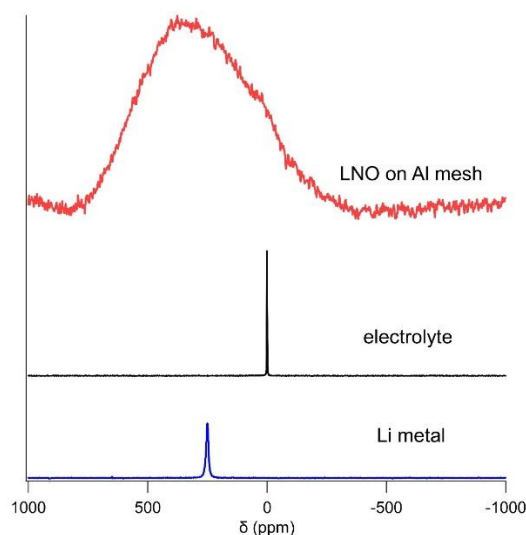


Figure 3.17 The static ${}^7\text{Li}$ NMR spectra of Li metal, electrolyte, and LNO measured separately by putting each part into the pouch cell.

In situ ${}^7\text{Li}$ NMR spectroscopy on a complete battery cell is also performed in order to monitor the phase evolution during cycling as shown in **Figure 3.16**. One interesting region (between SoC 65% and SoC 85%) is labelled in the corresponding voltage profile. The shift range containing peaks from Li metal and electrolyte is enlarged in **Figure 3.16c**. A small pouch cell was carefully assembled with the LNO cathode, lithium metal, and electrolyte LP30. Since there is no magic-angle spinning like for the *ex situ* measurements, the peak for ${}^7\text{LiNiO}_2$ is much broader covering a range from 1000 ppm to -250 ppm. This is verified by the static ${}^7\text{Li}$ NMR spectrum obtained for a single LNO pellet (**Figure 3.17**). The sharp peaks located at 270 ppm and 0 ppm could be ascribed to Li metal and electrolyte LP30, respectively. This is verified by the static ${}^7\text{Li}$ NMR spectra of a pouch cell with only a Li metal piece or a piece of separator soaked with the electrolyte, respectively (**Figure 3.17**).

Table 3.6 Comparison of peak positions between *in situ* ${}^7\text{Li}$ NMR and *ex situ* ${}^6\text{Li}$ MAS NMR spectra.

${}^7\text{Li}$ <i>in situ</i> NMR		${}^6\text{Li}$ <i>ex situ</i> NMR	
SoC (%)	Observed shifts (ppm)	SoC (%)	Observed shifts (ppm)
65%	516.6	65%	436.2
70%	561.2	70%	-
75%	543.6	75%	547.8
80%	557.7	80%	584.4
85%	517.7	85%	565.6

During charging, the centre of the broad peak assigned to LNO shifts towards 0 ppm linearly, since Ni^{3+} ions are successively oxidized to diamagnetic Ni^{4+} . Unlike the broad peak belonging to the Li ordering/disordering transition observed in *ex situ* ^6Li MAS NMR, it is impossible to detect such detailed changes anymore because of the broader components in the static ^7Li NMR spectra. However, we find the same signal shifting to higher ppm values in highly charged states just like that observed with *ex situ* NMR (**Figure 3.16**, region marked with dashed blue lines). The comparison of NMR shifts between *in situ* and *ex situ* NMR measurements in this region is shown in **table 3.6**. Although some differences exist in the exact shift positions, the overall left shifting tendency is identical. For the *in situ* NMR spectra, this signal intensity at about 600 ppm is maintained until only a minor intensity is finally left between the signal of Li metal and electrolyte. As observed both from *in situ* and *ex situ* NMR, the Li local environments contain one more Ni^{3+} for the Li-ordered structure before the phase transition H2 to H3. In this region, the NMR peak also does not move to lower ppm values as in *ex situ* data. Instead, the peak position is steady only with small broadening. Unlike for the *ex situ* measurements, the *in situ* NMR spectra beyond SoC 85% are still available here because of the higher cut-off voltage of 4.7 V. As described above, weak intensity is still observed at higher ppm values (around 600 ppm), confirming that Li ions are still surrounded by Ni^{3+} with Ni-O-Li 180° bonds in the single H3 phase. During discharge, the changes observed during charge are reversed. The right shift during discharge observed at very low Li contents is missing in the *ex situ* NMR spectra, because the *ex situ* samples do not contain this very highly charged regime. Overall, a very high reversibility of the Li/vacancy ordering is observed. There are also clear changes for the peaks associated with Li metal and the electrolyte. For the peak ascribed to Li metal (about 260 ppm), the pristine signal is broad and the intensity is quite low since the radiofrequency radiation necessary to excite these NMR signals cannot penetrate the massive Li metal plate.⁸⁹⁻⁹¹ During continuous charging, more and more de-intercalated lithium ions from the cathode are deposited on the Li metal surface, increasing the intensity of the ^7Li signal drastically and also a clear narrowing is detected.

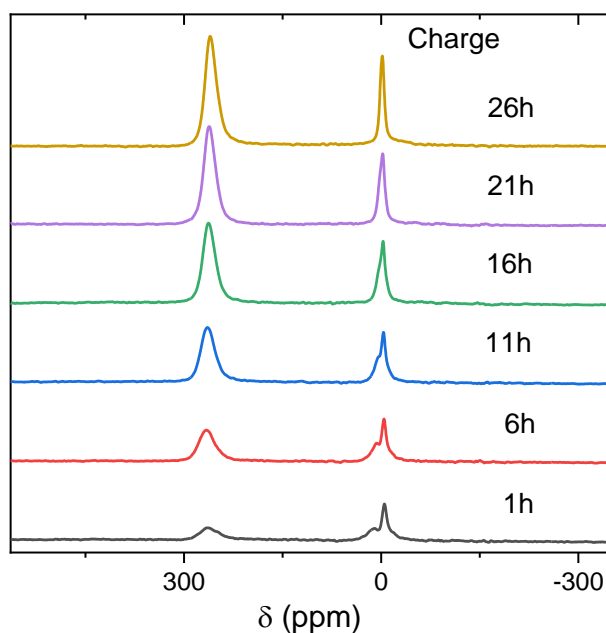


Figure 3.18 Selected static ${}^7\text{Li}$ NMR spectra extracted from the in situ NMR measurements for charging steps of 5 h. The small peak located close to the electrolyte signal (at 10 ppm) gradually disappears as described in the text.

As reported before, the exact NMR shifts are different for the Li metal foil and the small deposited Li structures, e.g. dendritic Li.⁸⁹ In the spectrum, a new peak from deposited Li gradually appears at slightly higher ppm values, indicating the sensibility of NMR for Li with dendritic structures. The strong increase in intensity can be explained by the small dimensions of the newly formed Li metal structures that can now be much better penetrated by the radiofrequency waves. The intensity of the peak at 260 ppm ascribed to small Li metal structures disappears almost completely during discharging. This shows that the Li removed from the Li metal electrode is taken exactly from the small Li dendrites/mossy structures that had previously been deposited, and not from the original Li metal plate. For the peak of the electrolyte close to 0 ppm, it is interesting to note that initially there is a clear peak splitting with a small peak situated on the left side, at about 10 ppm (**Figure 3.18**). However, such a peak splitting could not be found in the spectrum of the single electrolyte and the peak at 10 ppm is also not observed in the spectra of the pure Li metal nor for the pure LNO (**Figure 3.17**). Therefore, the peak at 10 ppm has to be ascribed to some interphase layer either between Li metal and electrolyte or between LNO and electrolyte. The value of 10 ppm is too high for pure

diamagnetic phases but could hint at some phases such as LiOH or Li₂CO₃ in some passivation layer on the surface of the LNO particles. The Li ions in these phases do not have direct Ni³⁺ neighbours, but still the close proximity to LNO could result in the shift value of 10 ppm. In the middle of the charging period, this small peak in the static spectra (**Figure 3.16c**) disappears because broad Li_xNiO₂ signals cover the bottom part of the peaks close to 0 ppm (**Figure 3.17**). Furthermore, the oxidation of Ni³⁺ to diamagnetic Ni⁴⁺ especially in the surface of the LNO particles can cause a reduction of the Li NMR shift for the Li in the passivation layer. At the end of discharging, this small peak is recovered again with even stronger intensity (**Figure 3.19**). This might also hint at some reversible side reactions at the highly charged states. Another explanation for the peak at 10 ppm might be the presence of a Li-rich phase containing high amounts of Ni⁴⁺, i.e. something close to Li_{2/3}Ni_{1/3}O, on the surface of LNO. This phase might have been formed in contact with the electrolyte. This Li rich Li₂NiO₃ structure recently is reported to be electrochemically active and can transform into a rock salt phase during cycling.⁹² This might explain the disappearance/reappearance during charging/discharging.⁹¹

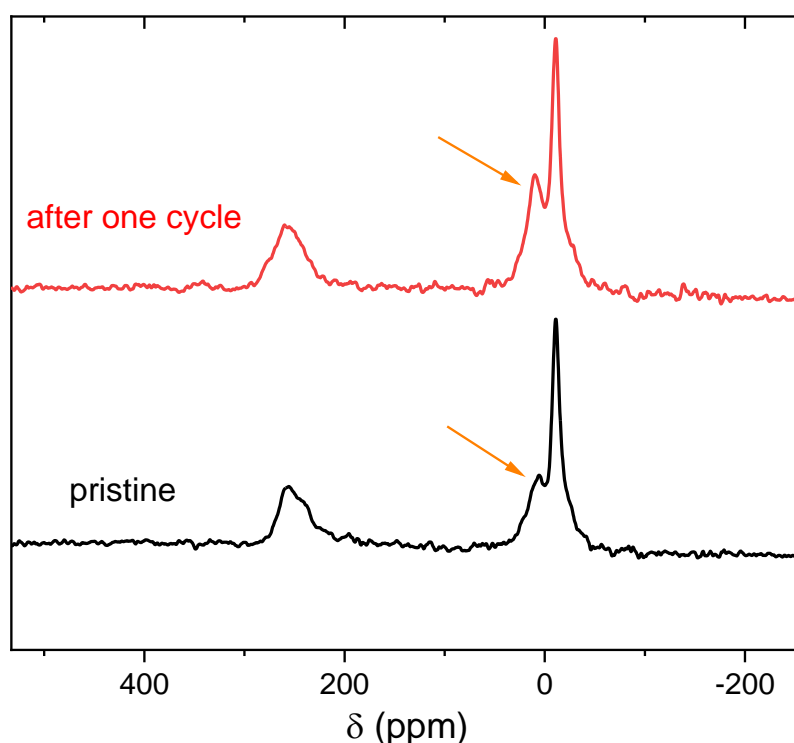


Figure 3.19 The comparison of the first in situ ⁷Li NMR spectrum of the complete battery in comparison to the spectrum obtained after the complete first cycle. Attention should be paid to the increasing area of the small peak located at 10 ppm.

3.3.5 Ex situ XAS

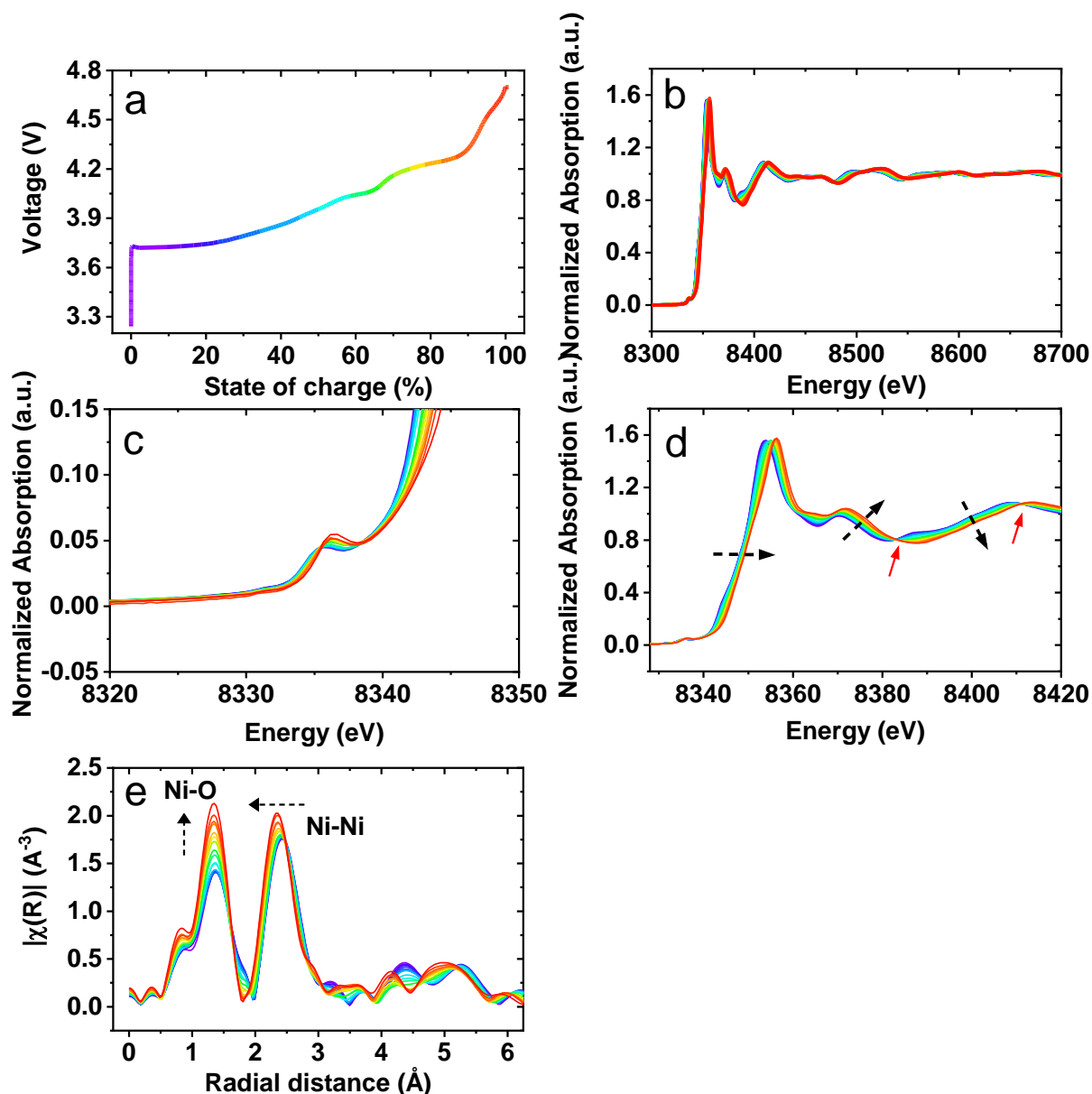


Figure 3.20 (a) Ni K-edge XAS spectra of the in situ LNO/Li half-cell. Cell voltage as a function of state of charge for the first cycle; (b) The in situ XAS spectra in the energy range between 8300 and 8700 eV; (c) An expanded view of the region of the pre-edge peak; (d) the edge region of 19 XAS spectra is enlarged to analyse the change of oxidation state and (e) Experimental Fourier transforms for Ni K-edge spectra as a function of state of charge.³¹

To investigate the electronic and structural environments of Ni-ions during the electrochemical process, *in situ* XAS was performed on the LNO cathode material at the Ni K edge in an *in situ* coin cell. The *in situ* half-cell was charged at a rate of C/12 to reduce hysteresis effects caused, e.g., by inhomogeneous reactions, and 19 spectra were acquired for the whole charging process, as indicated in the voltage profile (**Figure 3.20a, b**). The near-edge structure of K-edges reflects dipole-allowed transitions of the 1s electron to levels with substantial p-orbital character. The pre-edge peak near 8335 eV corresponds to the formally dipole-forbidden 1s \rightarrow 3d transition, which becomes broad and shifts with increasing state of charge (**Figure 3.20c**). This is caused by the rhombohedral distortion of the layered phase.⁹³ The Ni K absorption edge shifts towards higher energy throughout the whole charge process, suggesting steady electron removal continuously from Ni³⁺ to Ni⁴⁺ (**Figure 3.20d**). Two distinct isosbestic points (red arrows in **Figure 3.20d**) are detected at high and low energy for the charge process, indicating the phase transition process.⁹⁴ The Fourier transform (FT) data are shown in **Figure 3.20e**. Two coordination spheres are displayed with strong signals. The first coordination sphere represents the octahedral coordination of Ni with O neighbors. The amplitude of this peak increases with a decrease in Li content. For Ni³⁺, a Jahn-Teller distortion is present and thus four O atoms at the short distance and two O atoms at the long-distance lead to destructive interference between two components, thus diminishing amplitude in the FT data in the pristine state and early stages of charging. However, when Ni is oxidized to Ni⁴⁺, it has only a single contribution from six O atoms at a short distance. This makes the amplitude larger than that of Ni³⁺.⁹⁵ Interestingly, for the first seven spectra (from SoC 0% to SoC 34%), the amplitude almost keeps the same. This is because of the gradually increased Jahn-Teller distortion making the destructive interference stronger between two components, which offsets the effect of Ni oxidation. The second coordination sphere located near 2.6 Å is mainly due to a Ni-Ni single scattering contribution within the NiO₂ slabs. It shifts to a smaller value, suggesting a decrease in the interatomic distance in the Ni-Ni bonding, as expected from the smaller ionic radius of Ni⁴⁺ compared to Ni³⁺.⁹⁶ In summary, the XAS measurement monitored the whole Ni oxidation process. It confirms the appearance of a stronger Jahn-Teller effect in the early stages of charging, which corresponds to the region of the phase transition from H1 to M in *in situ* XRD data. Subsequently, this Jahn-Teller distortion disappears when large amounts of Ni⁴⁺ have been formed.

3.3.6 GITT

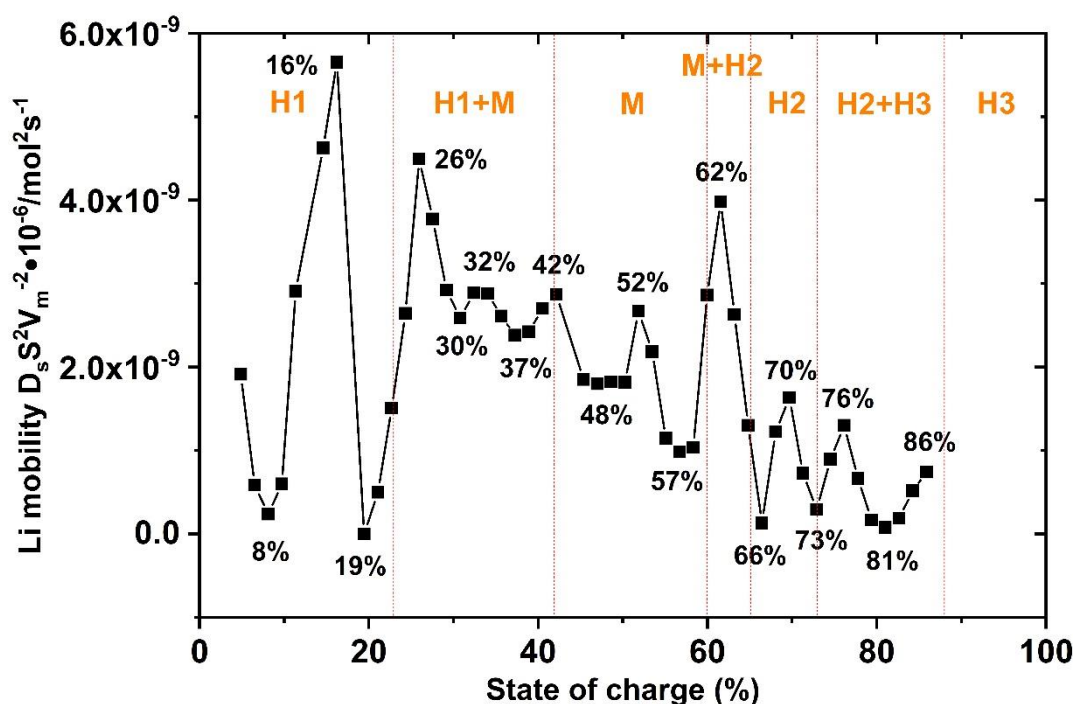


Figure 3.21 Li mobility calculated from GITT of LNO/Li half-cells.

GITT was used to probe the change of Li-ion diffusion coefficient during charging (**Figure 3.21**). Two additional GITT experiments were conducted to increase the reliability of the conclusions (**Figure 3.22**). The aim was to investigate the relationship between diffusion coefficient, lithium/vacancy ordering, and phase transitions. Since it is difficult to get exact values for the molar volume (V_m) and the active surface area (S), the normalized quantity $D_s S^2 / V_m^2$ was used to represent the changes in Li mobility, see **Figure 3.21**. The Li diffusion starts to increase beyond SoC 8%, because the formation of Li vacancies and the increasing of interlayer spacing effectively reduce the activation barrier for Li hopping.⁹⁷ Subsequently, the diffusion coefficient starts decreasing from SoC 16% and reaches a minimum at SoC 19%, after which it increases again. This overall trend of Li mobility evolution correlates well with VT NMR spectra: the Li diffusion of SoC 20% is much lower than that of the pristine state and with a SoC of 50%. Firstly, the enhanced Jahn-Teller effect distorts the layered structure and decreases the Li diffusion rate. Then, more vacancies were formed with continuous Li deintercalation and facilitate the Li mobility. The maximum diffusion coefficient is reached at SoC 26%, after which it starts decreasing quickly. At SoC% 62%, there is a pronounced

maximum in mobility which could be ascribed to the phase transition from M to H2. The disappearance of Jahn-Teller distortions makes the structure change back to a hexagonal one which is more suitable for Li diffusion.

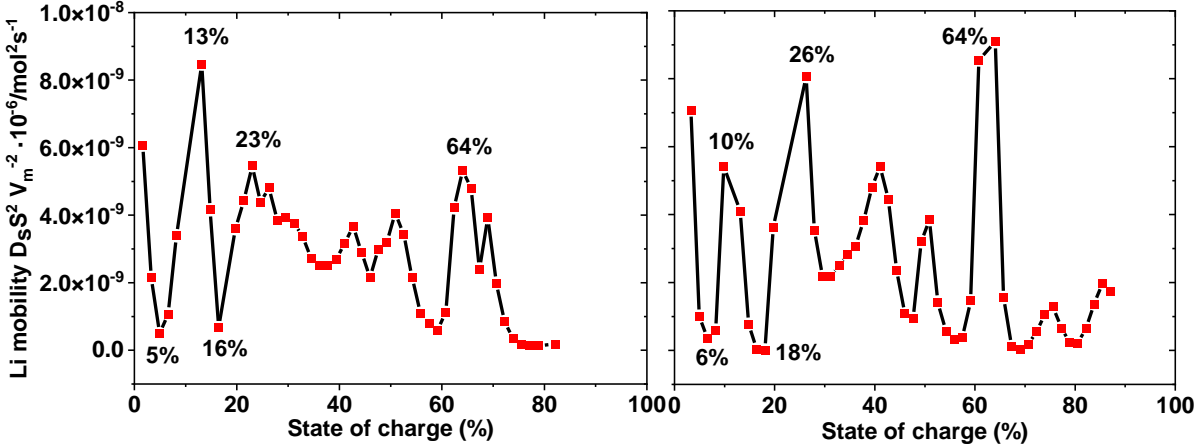


Figure 3.22 Repeated GITT measurement of LNO/Li half-cells.

3.4 Conclusion

We have investigated the structural changes during the complete first delithiation/relithiation cycle of LNO, with a focus on the change of local Li environments. The combination of *in situ* ^7Li and *ex situ* ^6Li NMR was especially applied to investigate the Li/vacancy ordering structures, in comparison with reported theoretical models. Combined movements of Li^+ ions and electrons generate the Li coordination environments with large amount of Ni^{3+} . This special local Li structure opens a new cognitive perspective towards structural collapse and evolution. GITT and XAS measurements were also conducted to explore changes of Li mobility and oxidation state of Ni. In summary, close attention should be paid to the change of local Li environments, a new perspective on the phase transition and lattice structures.

Chapter 4 Investigation of Structural and Electronic Changes Induced by Post-Synthesis Thermal Treatment of LiNiO_2

4.1 Introduction

As introduced in the 1st chapter, LNO would slowly decompose towards a rock salt phase under high-temperature conditions. This decomposition occurs at 700°C at low rate, while it proceeds much faster at 800°C.^{45,98} The decomposition rate is also influenced by the gas employed: an Ar atmosphere can cause a significantly more rapid decomposition rate than in air or in O_2 . The decomposition products contain $\text{Li}_{1-z}\text{Ni}_{1+z}\text{O}_2$, Li_2O and O_2 . Li_2O can be confirmed by XRD when an Ar atmosphere is chosen. Otherwise, Li_2O can react to O_2 , forming volatile Li_2O_2 . The distribution of rock salt like $\text{Li}_{1-z}\text{Ni}_{1+z}\text{O}_2$ phase may not be homogeneous across the sample. A larger z (or even thin layers of NiO) may be found at the surface rather than in the bulk.⁴¹ The annealing temperature, duration as well as atmosphere can profoundly affect the extent and rate of this transformation.

Bianchini et al. investigated the structural changes during decomposition by *in situ* XRD in detail.⁴¹ The unit cell volume starts decreasing at 700°C in air and the process proceeds three times slower than at 800°C. The variation of the volume can be mainly ascribed to the change in lattice parameter a . The substantial increase in a results from the reduction of Ni^{3+} to Ni^{2+} in the Ni layer. On the other hand, c remains stable at 700°C and has a minor increase at 800°C, reflecting slight variations in interlayer spacing. It can be understood by the interplay between Ni reduction (increase in c), Li loss, and replacement of Li^+ by smaller Ni^{2+} in the Li layer (decrease in c). In addition, the thermal expansion can also affect c in the direction of enlargement. These factors compete with each other and give rise to only small changes in c . The reduction of Ni^{3+} to Ni^{2+} also induces an increase in slab thickness (S), while the interlayer thickness (I) barely changes owing to a complex interplay of steric and coulombic effects. The above situation (S and I) gives rise to an increase in c ($c = 3(S+I)$). Furthermore, for pristine LiNiO_2 , high Li mobility within the interlayer space is expected, however the average mobility of the atoms located in the Li layers is decreasing because of the migration of Ni^{2+} to these sites.

Although LiNiO_2 in the pristine state is reported to be stable at temperatures below 700°C , the delithiated phases have a limited thermodynamic stability, especially for $x < 0.5$ in Li_xNiO_2 . All the phases on the LiNiO_2 - NiO_2 line in the phase diagram are calculated to be unstable at 0 K.⁹⁹ When heated at temperatures between 100 - 200°C , the situation is even getting worse, since the highly oxidized Ni^{4+} ions are not favored. The decomposition process includes a release of O_2 and a reduction of Ni^{4+} to Ni^{2+} . It was reported that lower content of Li also corresponds to lower temperatures at which O_2 release reaches a maximum.¹⁰⁰ The decomposition of partially delithiated Li_xNiO_2 follows a certain sequence: first Ni migrates to the Li layers and Li moves to the tetrahedral sites, forming a defective spinel structure. Then, a disordered layered structure appears after a two-phase transition, accompanied with O_2 evolution and Li/Ni mixing. A fully disordered rock salt structure can be observed as the final product, same as for the decomposition of pristine LiNiO_2 .

The well-known instability of delithiated phases induces interest in investigating the stability of the pristine state at moderately elevated temperatures (some hundred $^\circ\text{C}$), which is seldom reported.¹⁰¹ Some reactions may occur at low rate and small extent, making it challenging to characterize them. In order to investigate the correlation between low-temperature stability of the pristine state and cycling stability, a heat treatment in air after synthesis was performed with 12 h duration to increase the extent of these reactions. A series of heat-treatment temperatures (from 200°C to 1000°C) is used to investigate how the rate of these subtle reactions changes with temperature. The relationship between these reactions and LiNiO_2 decomposition is also uncovered. Characterization methods include *in situ* and *ex situ* XRD, *ex situ* ^7Li NMR, *ex situ* XAS, TEM, *ex situ* measurements of magnetic properties and thermogravimetric analysis (TG). By combining all these methods, we aim to provide the full image about reactions in LNO at different temperatures. The possibility of improving the electrochemical performance of LNO only by post-synthesis thermal treatment is also demonstrated.

4.2 Experimental

Synthesis of LiNiO₂: NiOH was synthesized through the traditional co-precipitation process. Three solutions were prepared at first: aqueous solution (A) 0.3L of 2 M NiSO₄; (B) 0.3L of 2 M NH₃ with 2M NaOH; (C) 0.2 L of 2 M NaOH. At first, 200ml deionized water was added to the 1.2 L reactor with 2ml NH₃ in H₂O. Then the pH value was automatically controlled to 10.7 by adding solution C. Once the pH value is steady, we start adding solutions A and B. The pumping speed was calculated in such a way that the reaction could be finished in 18 h. The precipitate was washed thoroughly with deionized water and dried in an oven at 80 °C overnight. LiNiO₂ (LNO) was then synthesized by calcining the mixture of the precipitate (NiOH) and LiOH. The two components were ground using a mortar for 30 minutes and transferred to the oven. In a pure oxygen atmosphere, the temperature was firstly increased to 500 °C, maintained for 6 h, and then further increased to 700 °C, where it was kept for another 12 h. The sample was cooled freely in the oven, which normally takes 8-10 h.

Post-synthesis thermal treatment of LiNiO₂: After the synthesis was performed in O₂, LNO samples were reheated in air from room temperature to different temperatures (200 to 1000 °C for 12 h) with a heating rate of 5 °C min⁻¹. In the following, these samples are denoted as LNO-“heat treatment temperature” (for example, LNO-200).

Electrochemical Characterization: Same processes for making electrodes and coin cells in the last chapter were used to test the electrochemical performance of all samples after the thermal treatment. The voltage window is enlarged to 2.5-4.5 V instead of using 2.8-4.3 V to increase the specific capacity of the cathodes. The cells were cycled at a rate of 0.1 C (1 C = 180 mA g⁻¹) for long-term cycling.

Synchrotron radiation diffraction and X-ray absorption spectroscopy: The crystallographic structure of heat-treated LNO was determined by high-resolution synchrotron radiation diffraction (SRD) with a photon energy of 60 keV ($\lambda = 0.21 \text{ \AA}$) at beamline P02.1, storage ring PETRA III at DESY (Deutsches Elektronensynchrotron) in Hamburg, Germany. *In situ* high-temperature SRD (HTSRD) was carried out at MS beamline of Paul Scherer Institute (PSI), Villigen, Switzerland. LNO powders were heated in air with a heating rate of 20 °C min⁻¹ from room temperature to 900 °C. XRD patterns were collected with steps of 50 °C except for the high-temperature region (750-900 °C), where the interval was set to 25 °C. A MYTHEN II detector was used for obtaining the diffraction images at synchrotron radiation energy of 24.3

keV ($\lambda = 0.51 \text{ \AA}$). The lattice structure parameters and phase fractions were refined using the Rietveld method with the program Fullprof.¹⁰² X-ray absorption spectroscopy (XAS) was performed at the XAS beamline of the KIT Light Source (Karlsruhe). XAS data were recorded at the Ni K-edge (8333 eV) in transmission mode. Background subtraction and normalization was done with the ATHENA software, which is part of the Demeter package. The energy calibration was checked by a Ni metal foil, which was placed between the second and third ionization chamber.

Solid-State Nuclear Magnetic Resonance Spectroscopy: ^7Li magic-angle spinning (MAS) NMR experiments were conducted on a Bruker Avance 200 MHz spectrometer at a magnetic field of 4.7 T. Spectra were acquired at a Larmor frequency of 77.8 MHz with 1.3 mm rotors and spinning at 60 kHz. A rotor-synchronized Hahn-echo pulse sequence (90° - τ - 180° - τ -acquisition) was used with a 90° pulse length of $0.9 \mu\text{s}$ and a recycle delay of 1 s. The ^7Li NMR shifts were referenced using an aqueous 1 M LiCl solution (0 ppm). All spectra were normalized with respect to sample mass and number of scans.

Thermogravimetric analysis: The TGA measurement was performed to acquire the mass loss of LNO during heat treatment. It was carried out on an STA 449 F3 Jupiter instrument (NETZSCH) with a heating rate of 5 K min^{-1} up to $1000 \text{ }^\circ\text{C}$ in air atmosphere. The gas flowing rate is 50 ml min^{-1} . Before the measurement, 30 min of gas flowing was conducted. The experiment was repeated once to check reproducibility. The data has been corrected considering the buoyancy effect.

Magnetization measurements: Magnetization as a function of temperature and magnetic field was measured with a physical property measurement system (PPMS® DynaCool™) from QuantumDesign equipped with a vibrating sample magnetometer (VSM). Zero field cooled (ZFC) and field cooled (FC) magnetization vs. temperature was measured from 2 K to 380 K (for ‘pristine’ sample only up to 300 K) at a field of 0.5 T. From 2 K to 50 K the heating rate was set to 1 K min^{-1} and from 50 K to 380 K it was set to 2 K min^{-1} . Magnetization vs. field hysteresis measurements with maximal fields of 7 T have been performed at 2 K and 300 K in a field cooled mode starting the field scan with the maximum positive field as specified above. Additionally, magnetization vs. temperature was measured from 270 K to 390 K at a field of 5 T with a rate of 2 K min^{-1} . The data sets from these temperature scans at a higher field were used for Curie-Weiss fits. Additionally, magnetization vs. field hysteresis measurements were performed at 300 K and 390 K with a maximum field of 5 T for in-depth magnetic

characterization at higher temperatures. For data evaluation, the sample masses for pristine LNO, LNO-200, and LNO-300 have not been corrected. For LNO-400 to LNO-750 that contain a certain amount of Li_2CO_3 only the masses of the LNO phase have been considered since Li_2CO_3 has a negligible contribution to the magnetic signal. For LNO-800 and LNO-1000 that consist of LNO and a cubic (Li, Ni)O phase the masses and molar masses have accordingly been corrected assuming two different types of (Li, Ni)O phase: a) a Li containing $\text{Li}_{0.5}\text{Ni}_{0.5}\text{O}$ phase that corresponds to LiNiO_2 (LNO) and b) a Li-free NiO phase.

Transmission electron microscopy (TEM): In order to perform TEM measurements, the sample was prepared inside an argon filled glovebox and then transferred to the microscope using a vacuum transfer holder in order to prevent samples from extensive air exposure. The dry powder of the samples was directly dispersed on the TEM holey carbon membrane without the use of solvents. The measurements were performed using a double aberration-corrected and monochromated Themis Z microscope equipped with a Gatan GIF Continuum 970 spectrometer and a K3 IS camera. High-resolution STEM-HAADF images were recorded using a collection angle range of 63-200 mrad. EELS spectrum imaging data cubes were acquired with a probe convergence angle of 30 mrad and a probe current of 0.5 nA. The pixel size was around 1 nm and a dwell time of 0.1 s per pixel was used for all the data series. The camera length was 30 mm and the spectrometer aperture was set to 5 mm resulting in a collection angle of about 40 mrad. All EELS data was acquired in dual-EELS mode containing both the core loss and the low loss spectra. All core loss spectra were realigned and deconvoluted based on the low loss spectra pairs prior to any data analysis.

4.3 Results and Discussion:

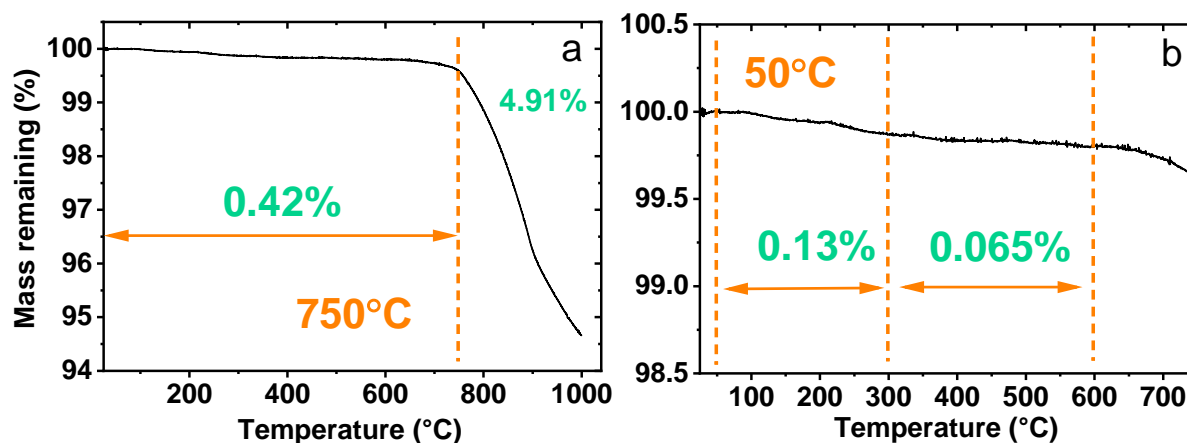
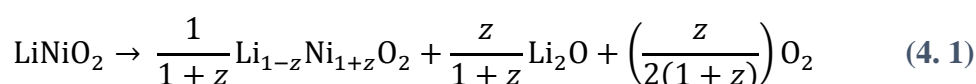


Figure 4.1 (a) full temperature region and (b) enlarged region of TGA measurement on LNO in air from room temperature to 1000 °C (750 °C for (b)). The green numbers correspond to the mass loss of denoted regions.

As-prepared LNO was further heated in air at different temperatures (200, 300, 400, 500, 600, 700, 750, 800, 850, and 1000 °C) for 12 h and slowly cooled to room temperature. As explained in the Experimental Section, these samples are denoted as LNO-“heat treatment temperature” (for example, LNO-200). A TGA measurement was conducted on as-prepared LiNiO₂ in air to investigate the mass loss during the heat treatment (**Figure 4.1**). This measurement was repeated and a similar behavior of mass loss was observed (**Figure 4.2**). 50 °C was chosen as the reference for original mass of the LNO, since the sudden mass drop at the beginning of the experiment might just stem from removal of moisture. Interestingly, the mass loss within the 50-300 °C temperature region (0.13%) is two times larger than that of the 300-600 °C region (0.065%). The mass loss is decreasing at higher temperatures, since LNO reacts with CO₂ to a larger extent and the formation of Li₂CO₃ offsets the oxygen loss. This will be further discussed in the XRD part. A strong mass loss was found starting from 750 °C on. 4.91% mass loss was recorded between 750 and 1000 °C, whereas the corresponding value between 50 and 750 °C is only 0.42%. The mass loss at high temperatures corresponds to the phase transition from layered to cubic structure, which is accompanied by severe loss of Li and O₂:



Herein, $\text{Li}_{1-z}\text{Ni}_{1+z}\text{O}_2$ denotes the decomposition product still possessing a layered structure. After the continuous loss of O and Li, a phase transition occurs and $\text{Li}_{1-y}\text{Ni}_y\text{O}$ will be used to denote the cubic structure.

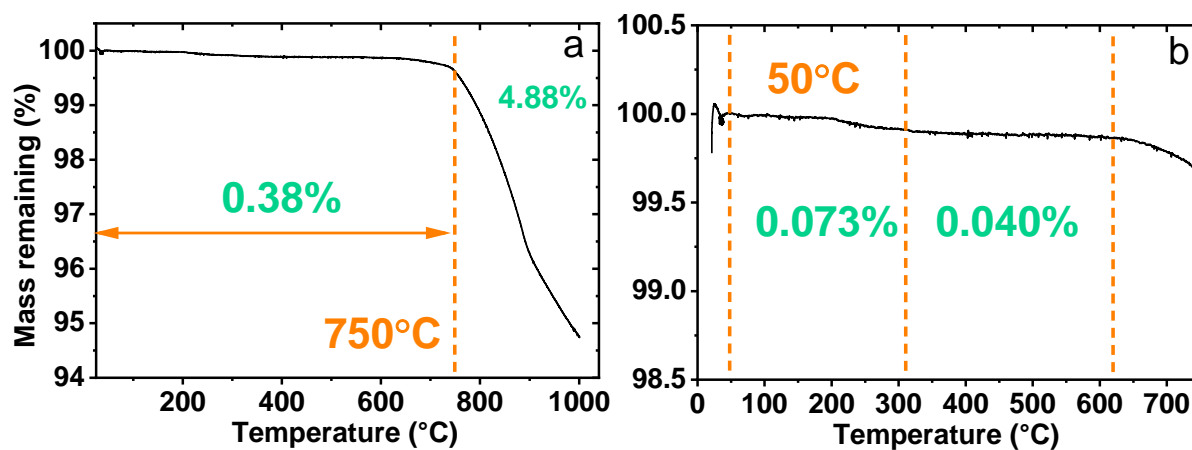


Figure 4.2 (a) Full temperature region and (b) enlarged region of the *repeated* TGA measurement of as-prepared LNO in air from room temperature to 1000 °C.

4.3.1 Electrochemical performance

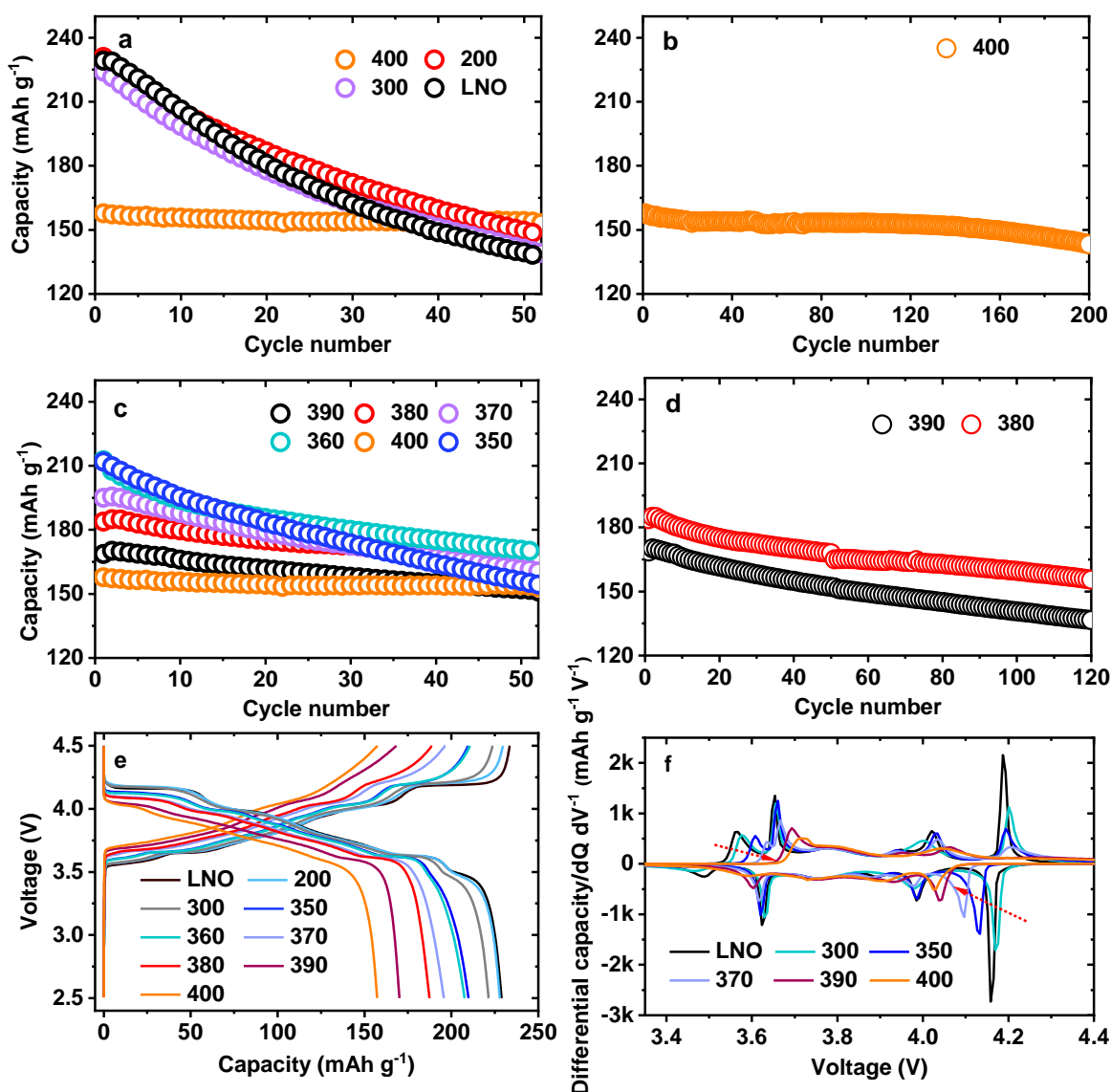


Figure 4.3 Electrochemical performance during galvanostatic cycling at 0.5 C in the voltage range of 2.5-4.5 V: **(a)** pristine LNO, LNO-200, LNO-300, and LNO-400, **(b)** long-term cycling performance of LNO-400, **(c)** comparison between LNO-350, LNO-360, LNO-370, LNO-380, and LNO-390 and **(d)** long-term cycling performance of LNO-380 and LNO-390. **(e)** Cell voltages as a function of specific capacities during the 1st cycle of all cathodes and **(f)** differential capacity as a function of cell voltage (dQ/dV vs. V) of selected cathodes. The red dashed arrows show the changes with increasing heating temperature.

To investigate the influence of the heat treatment on electrochemical performance, selected samples were used to prepare cathodes that were tested in coin-type half-cells. **Figure 4.3a** shows the cycling performance of pristine LNO, LNO-200, LNO-300, and LNO-400 cycled galvanostatically between 2.5 and 4.5 V at 0.1 C (18 mA g⁻¹) at 25 °C. Tiny differences in electrochemical performance from pristine were observed. The capacity retention after 50 cycles is 64.7% ± 2.4% for LNO-200, 63.0 ± 2.1% for LNO-300, and 60.8 ± 1.8% for pristine LNO. The initial discharge capacities of these three cathodes are close (229 mAh g⁻¹ for LNO-200 and LNO, 224 mAh g⁻¹ for LNO-300). The cycling stability is obviously enhanced when the heat-treatment temperature is increased to 400°C. LNO-400 cathode maintains 90.8 ± 3.5% of its initial capacity after 200 cycles (**Figure 4.3b**). Since there is an obvious specific capacity difference between the samples heated to 300 and 400, five more heat-treatment temperatures (from 350 to 390 °C) were added in this region to investigate this in detail to further optimize the performance (**Figure 4.3c**). The specific capacities gradually decrease from 211 (LNO-350) to 168 mAh g⁻¹ (LNO-390), but the corresponding retentions are improved step by step from 73.6 ± 2.2%, 80.3 ± 2.6%, 82.9 ± 3.5%, 91.4 ± 3.1% to 90.2 ± 3.4% after 50 cycles. The improved cycling stability is maintained during prolonged cycling of LNO-380 and LNO-390 cathodes. As shown in **Figure 4.3d**, the half cells exhibit a capacity retention of 84.56% for LNO-380 and 83.44% for LNO-390 after 120 cycles. Better cycling stability can be realized when the upper voltage limit was reduced from 4.5 to 4.3 V, since side reactions between electrode and electrolyte are stronger at high cell voltages. Examples for LNO-360 and LNO-370 are displayed in **Figure 4.4a**. Both samples show a formation behaviour in the first few cycles, i.e. an increasing capacity. A rock-salt cubic phase at the surface of the cathodes may make the electrolyte immersion slower (discussed in the TEM part later). In summary, the electrochemical performance is quite sensitive to the heat-treatment temperatures between 350 to 390 °C. To better understand the effect of heat treatment on the electrochemical properties, first-cycle voltage and dQ/dV profiles were plotted in **Figure 4.3e, f**, respectively. With increasing heat-treatment temperatures, the average voltage of the voltage plateaus observed during charging is also increased. This increase is related to a larger overpotential, i.e. stronger polarization.

The observed voltage is the sum of thermodynamic equilibrium voltage of an electrochemical reaction and the overpotentials (cell impedance).²⁹ High-temperature treatments induce a thicker cubic phase or Li_{1-z}Ni_{1+z}O₂ region at the surface or even the formation of Li₂CO₃ (see discussions on XRD, magnetic measurements, and TEM below) and therefore larger cell

impedance. In the corresponding dQ/dV curves of cathodes treated at higher temperatures, peaks which represent two-phase regions also appear at higher potentials during charging. Moreover, with increasing heat-treatment temperature, an increasing peak width is observed in the voltage range 4.15-4.27 V. This peak corresponds to the phase transition from the second hexagonal phase (H2) to the third hexagonal phase (H3).³⁶

The off-stoichiometry ($\text{Li}_{1-z}\text{Ni}_{1+z}\text{O}_2$) has been shown to disrupt Li ordering, thus establishing the behaviour of solid solution and eliminating phase transitions.⁸² The H2 to H3 phase transition is crucial to the performance, since it always entails large volume changes and the coexistence of two phases induces interfacial strain.¹⁰³ The release of the strain further induces cracking in electrode particles. To confirm if this surface structure transformation is reversible, the LNO-400 cathode was reheated in pure oxygen again and tested. The same voltage profile as for the pristine LNO sample was observed (**Figure 4.4b**), which shows that the $\text{Li}_{1-z}\text{Ni}_{1+z}\text{O}_2$ or cubic surface phases could be reversibly transformed to a layered phase again. During resynthesis, Li from surface Li_2CO_3 will be incorporated into the surface lattice and local “LNO synthesis” happens again. The electrochemical performance of samples LNO-500 and LNO-600 was also tested (**Figure 4.4c**). The specific capacities are very small (below 80 mAh/g) with strong polarization effects. Interestingly, the specific capacity increases to 160 mAh g^{-1} for the LNO-700 sample (**Figure 4.4d**). The unusual increase could be ascribed to the different reaction situation during post-synthesis thermal treatment at 700 °C, detailed discussion can be found in the following XRD part. The LNO-850 sample has almost no capacity (**Figure 4.4e**), although decreased charging/discharging rate could improve this situation. A table (**Table 4.1**) is given below to summarize all the electrochemical performance. To investigate the chemical and structural changes related to the electrochemical performance, multiple characterization methods have been applied as described hereinafter.

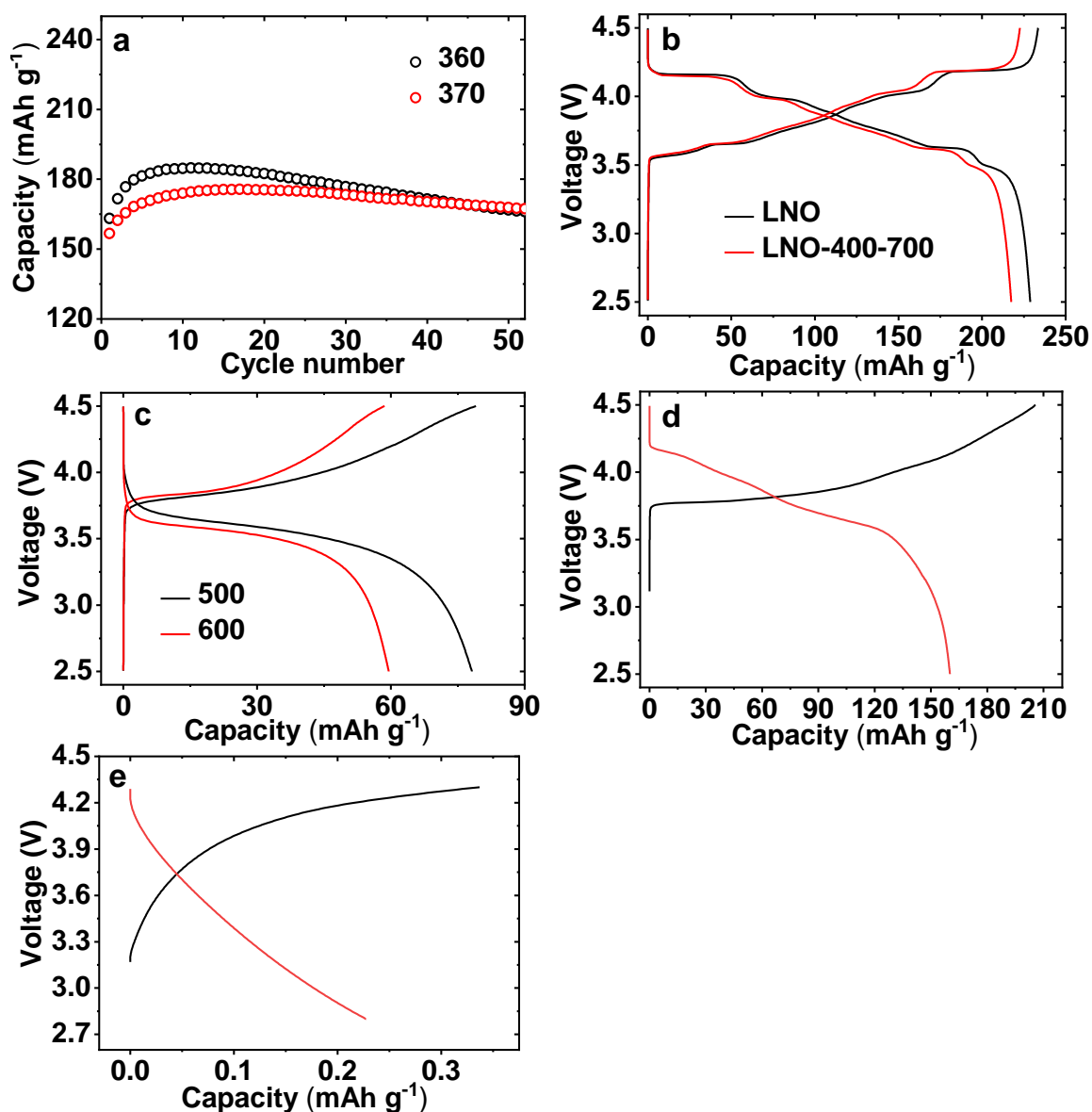


Figure 4.4 Electrochemical performance during galvanostatic cycling at 0.5 C: **(a)** Cycling performance of LNO-360 and LNO-370 in the voltage range between 2.5-4.3 V, **(b)** the difference between pristine LNO and the reheated LNO-400, **(c)** cell voltages as a function of specific capacities during the 1st cycle of LNO-500 and LNO-600, **(d)** cell voltages as a function of specific capacities during the 1st cycle of LNO-700, and **(e)** Cell voltages as a function of specific capacities during the 1st cycle of LNO-850.

Table 4.1 Summary of the electrochemical performance of all mentioned materials.

Name	Initial discharge capacity (mAh g ⁻¹) 2.5-4.5 V 0.1 C	Capacity retention after 50 cycles
pristine	229	64.7% ± 2.4%
LNO-200	231	64.7% ± 2.4%
LNO-300	224	63.0% ± 2.1%
LNO-350	212	73.6% ± 2.2%
LNO-360	212	80.3% ± 2.6% 102%*
LNO-370	195	82.9% ± 3.5% 106%*
LNO-380	184	91.4% ± 3.1%
LNO-390	168	90.2% ± 3.4%
LNO-400	158	97.6% ± 3.7%
LNO-500	79	
LNO-600	58	* 2.5-4.3 V voltage window
LNO-700	160	
LNO-850	0.2	

4.3.2 Ex situ XRD

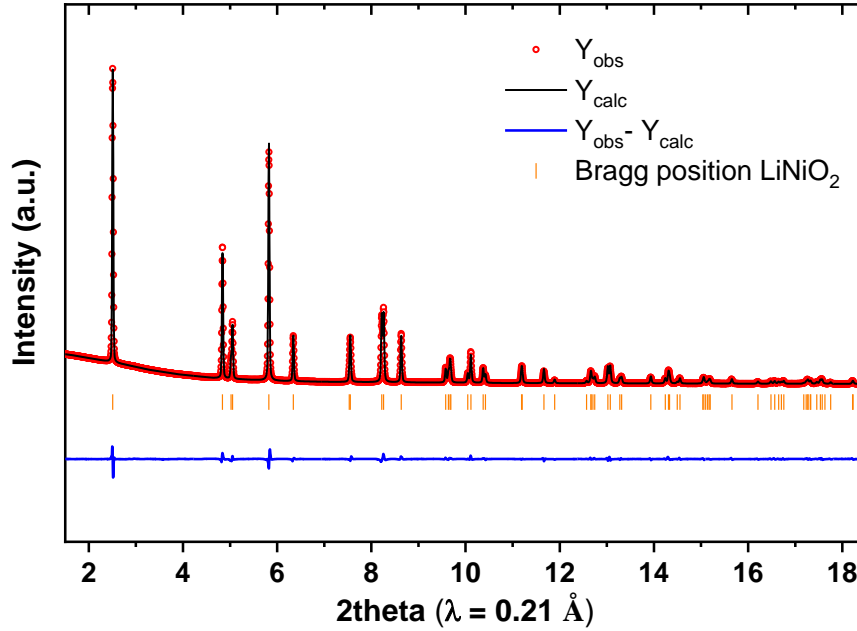


Figure 4.5 The XRD Rietveld refinement pattern of LNO with Li/Ni antisite mixing.

Table 4.2 Detailed information about the refinement in **Figure 4.5**.

LiNiO ₂						
$R\bar{3}m$						
a = 2.87660(2) Å				$R_{\text{Bragg}} = 2.49$	$\chi^2 = 0.8913$	
c = 14.19490(3) Å				$R_{\text{wp}} = 7.70$		
Atom	Wyckoff position	Atomic position			SOF	B_{iso}
		x/a	y/b	z/c		
O	6c	0	0	0.2420(7)	1	0.69(3)
Ni	3b	0	0	0.5	0.969(7)	0.20(5)
Li	3a	0	0	0	0.969(7)	1.32(5)
Ni	3a	0	0	0	0.030(4)	1.32(5)
Li	3b	0	0	0.5	0.030(4)	0.20(5)

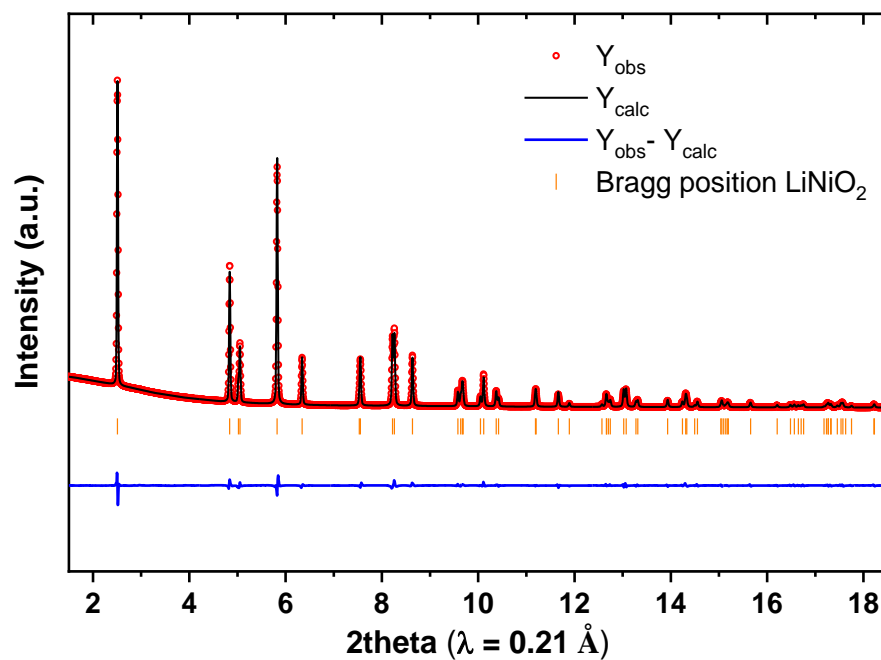


Figure 4.6 The XRD Rietveld refinement pattern of LNO with excess Ni in Li layers.

Table 4.3 Detailed information about the refinement in **Figure 4.6**.

LiNiO ₂						
$R\bar{3}m$						
a = 2.87660(1) Å				R _{Bragg} = 2.91	χ ² = 0.9448	
c = 14.19492(1) Å				R _{wp} = 7.94		
Atom	Wyckoff position	Atomic position			SOF	B _{iso}
		x/a	y/b	z/c		
O	6c	0	0	0.2421(1)	1	0.53(2)
Ni	3b	0	0	0.5	1	0.21(0)
Li	3a	0	0	0	0.971(4)	1.07(8)
Ni	3a	0	0	0	0.028(7)	1.07(8)

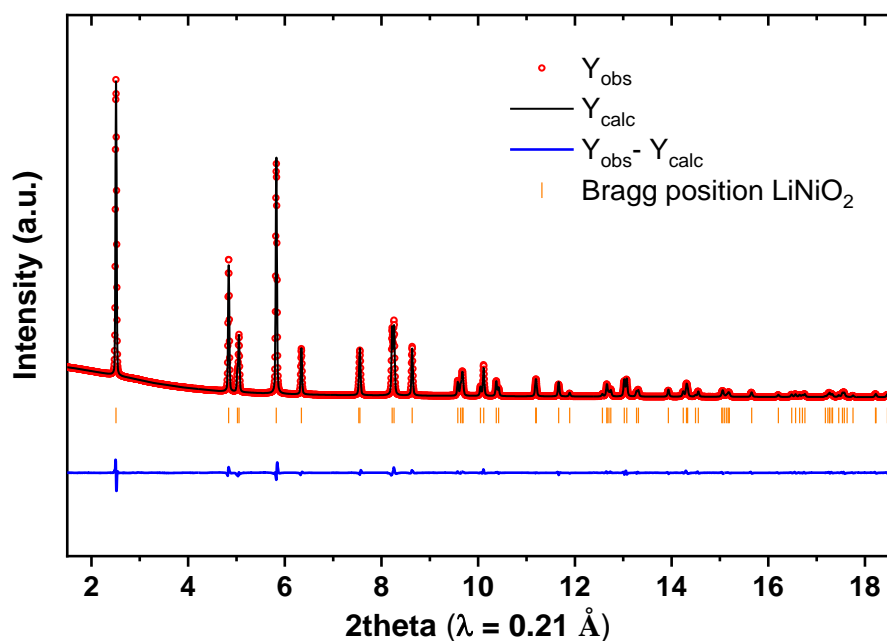


Figure 4.7 The XRD Rietveld refinement pattern of LNO with Li/Ni exchanging with different composition on the Li and Ni sites.

Table 4.4 Detailed information about the refinement in **Figure 4.7**.

LiNiO ₂						
$R\bar{3}m$						
a = 2.87659(9) Å				R _{Bragg} = 2.07		χ ² = 0.8667
c = 14.19485(1) Å				R _{wp} = 7.59		
Atom	Wyckoff position	x/a	y/b	z/c	SOF	B _{iso}
O	6c	0	0	0.2421(5)	1	0.91(7)
Ni	3b	0	0	0.5	0.932(2)	0.19(3)
Li	3a	0	0	0	0.974(9)	1.21(0)
Ni	3a	0	0	0	0.025(2)	1.21(0)
Li	3b	0	0	0.5	0.067(9)	0.19(3)

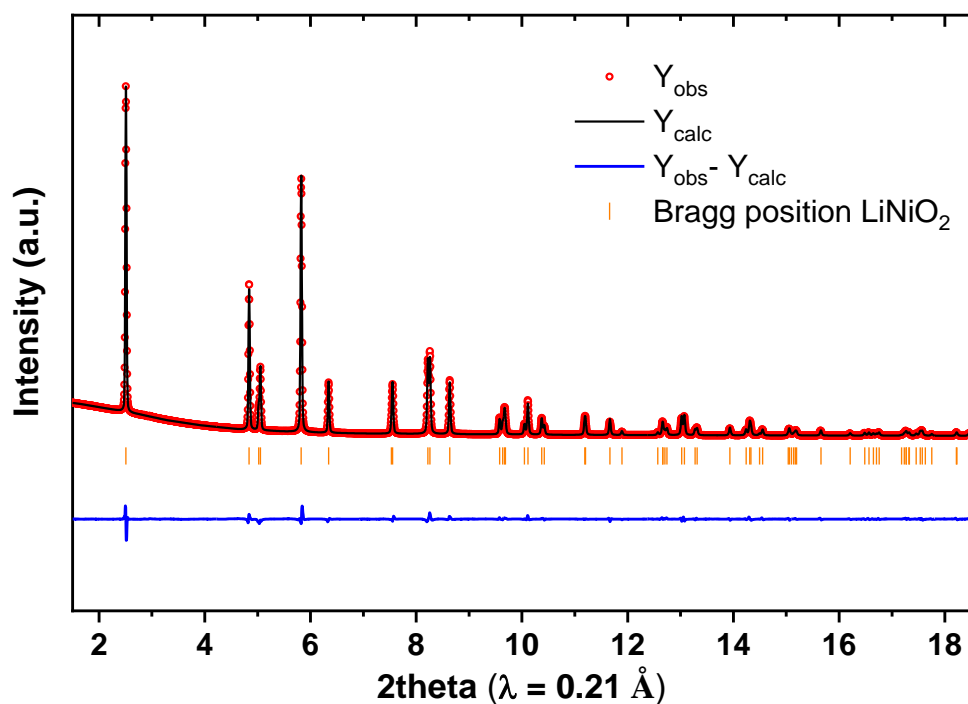


Figure 4.8 The XRD Rietveld refinement pattern of LNO with vacancies in Ni layers.

Table 4.5 Detailed information about the refinement in **Figure 4.8**.

LiNiO ₂						
$R\bar{3}m$						
a = 2.87659(9) Å				R _{Bragg} = 2.06	χ ² = 0.8669	
c = 14.19485(4) Å				R _{wp} = 7.61		
Atom	Wyckoff position	x/a	y/b	z/c	SOF	B _{iso}
O	6c	0	0	0.2421(4)	1	0.91(8)
Ni	3b	0	0	0.5	0.937(7)	0.19(4)
Li	3a	0	0	0	0.975(1)	1.20(4)
Ni	3a	0	0	0	0.025(0)	1.20(4)

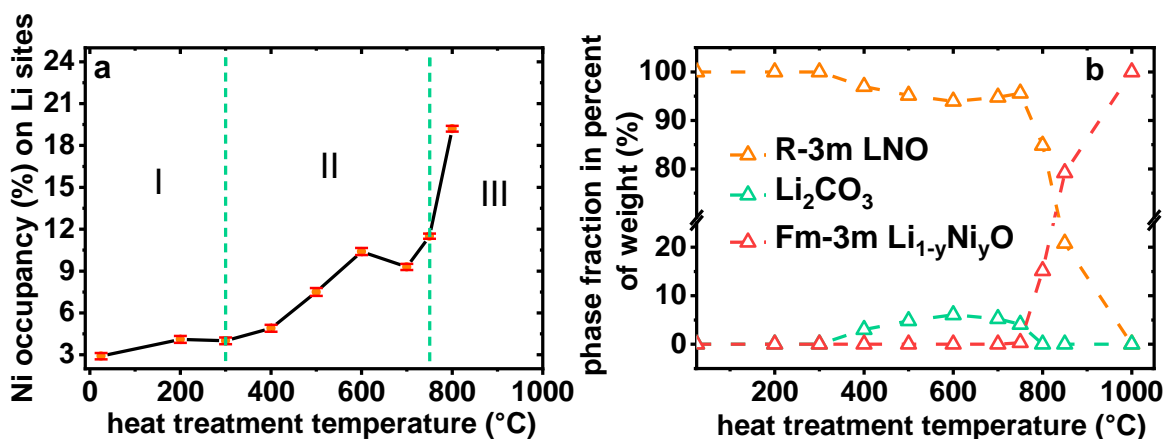


Figure 4.9 (a) The change of Ni occupancy on Li sites (%) from the Rietveld refinement results. 25 °C represents the pristine state. Three regions are labelled I, II, and III. **(b)** The change of phase composition with increasing heat-treatment temperatures.

Regarding the structure of ideal LNO, it has a cubic close-packed (ccp) array of oxygen atoms. The Li and Ni cations are located in alternating layers in the octahedral vacancies of the oxygen latter. Each oxygen has three neighbours of Li and three of Ni, and each cation has six oxygen neighbours. LNO crystallizes with a rhombohedral α -NaFeO₂-type structure (space group of $R\bar{3}m$). However, two kinds of defects can exist: excess Ni ions occupy Li sites and site exchange of small amounts of Li and Ni (Li/Ni exchange). To investigate the exact defect type existing in LNO, Rietveld refinement of the parameters of four different structural models against the SRD data was performed. The first one is the model of Li/Ni exchange (**Figure 4.5**). χ^2 (reduced chi-square) of 0.8913 and an exchange value of 3.0% were obtained. Notice that a value of χ^2 smaller than 1 happens herein because Fullprof refines a structural model against XRD data having a low and noise-free background: If the background is very low compared to the diffraction peaks and if there is no noise in there, it is known that most of the refinement programs like Fullprof, TOPAS, etc. result in χ^2 which is lower than 1. If only Ni located in Li planes is considered, the refinement results χ^2 of 0.9448, and the value for extra Ni was 2.9% (**Figure 4.6**). The formation energy of the Li/Ni exchange is dependent on the total fraction of Ni²⁺. The exchange often happens in LiNi_xCo_yMn_{1-x-y}O₂ materials, since Ni²⁺ ions are needed for charge compensation of Mn⁴⁺. For LiNiO₂, a trace amount of Ni²⁺ makes the exchange energy very large, so the lower χ^2 of the first model only indicates there is possibly some Ni ions in Li planes, rather than the exchange defect being dominant. Another two models were further considered. If the amount of Ni on Li sites and that of Li on Ni sites are not equal, χ^2 was much smaller (0.8667). 2.5% Ni and 6.8% Li are located in Li and Ni layers, respectively

(Figure 4.7). Notice that the scattering power of the Li atom is very weak, so it is difficult to distinguish Li ions and vacancies during this refinement and the value of 6.8% is beyond the actual value.

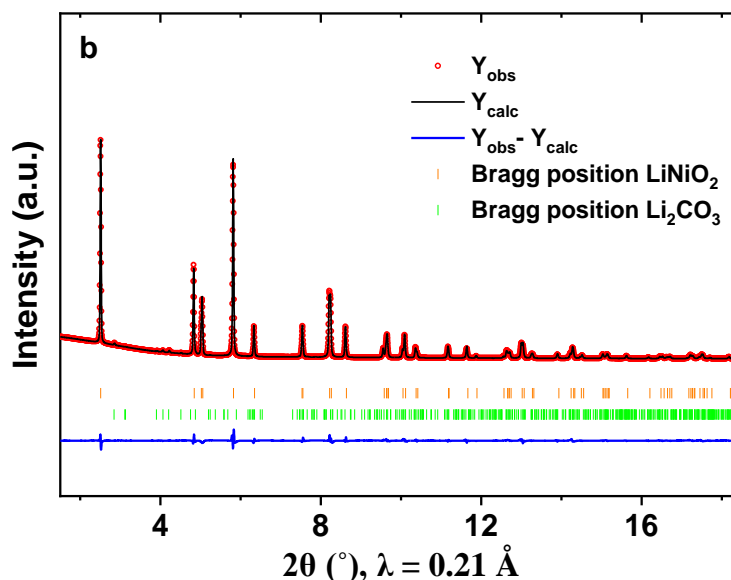


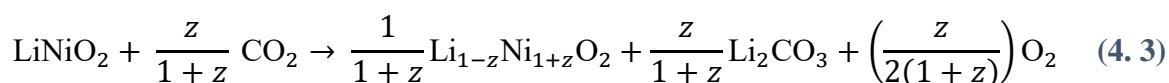
Figure 4.10 XRD Rietveld refinement pattern of LNO-600.

To confirm this, only vacancies without Li in Ni planes were included in the last fitting model (Figure 4.8). Similar results as for the 3rd refinement were obtained with χ^2 of 0.8669, extra Ni value of 2.4%, and vacancy amount of 6.2%. Although higher fitting degrees were acquired for the last two models, the refined results are not meaningful. Extra Ni ions occupying Li sites ($\text{Li}_{1-z}\text{Ni}_{1+z}\text{O}_2$) are considered to be the dominating defect in LNO with a small degree of Li/Ni exchange. All following refinements for layered phases are based on the model of $\text{Li}_{1-z}\text{Ni}_{1+z}\text{O}_2$: oxygen atoms occupy the 6c sites (0, 0, z_{ox}) and lithium and nickel atoms occupy the octahedral sites 3a (0, 0, 0) and 3b (0, 0, 0.5), respectively). Occupancy of Ni on Li site was refined (Li on Ni site was not considered) and all sites are assumed to be fully occupied. The value of Ni occupancy on Li sites and phase fractions for heat-treated samples are displayed in Figure 4.9a, b, respectively. Three regions can be identified, in agreement with the TGA results described above: I) pristine to 300 °C, II) 400 to 750 °C and III) 800 to 1000 °C. In the first region, a slight change of Ni occupancy on the Li sites is found from $2.9 \pm 0.2\%$ for the pristine sample to $4.0 \pm 0.2\%$ for LNO-300, without any new phases being formed. In region II, the Ni occupancy on lithium sites exhibits a significant increase from $4.9 \pm 0.3\%$ for LNO-400 to $10.4 \pm 0.3\%$ for LNO-600.

In this second region Li_2CO_3 is formed, i.e. Li is removed from the main phase. Based on the refinement result, the content of Li_2CO_3 increases from $3.03 \pm 0.58\%$ for LNO-400 to a maximum value of $6.08 \pm 0.52\%$ for LNO-600 and then decreases to $4.07 \pm 0.97\%$ for LNO-750. A representative refinement for LNO-600 containing Li_2CO_3 is displayed in **Figure 4.10**. As reported, LNO reacts with CO_2 at room temperature as well as at high temperatures (900 °C).¹⁰⁴ The reaction is described by the following equation:



This reaction is a thermodynamically favoured reaction and the Ni^{3+} is reduced to Ni^{2+} . The extent of this reaction is strongly affected by reaction temperature, duration, and atmosphere. Equation (4.2) is based on high temperatures (above 650 °C) and a pure CO_2 atmosphere.¹⁰⁴ When the reaction takes place at room temperature and in air, $\text{Li}_{1-z}\text{Ni}_{1+z}\text{O}_2$ rather than NiO would form. The equation then changes to:



Although Eqn. (4.3) looks quite similar to the decomposition reaction (Eqn. (4.2)), the two reactions happen under different conditions. The decomposition of LNO will not occur below 700 °C.⁵¹ We will further discuss this point for the sample LNO-700. The rate of Eqn. (4.3) is very small and it was reported that Li_2CO_3 with an amount of 6.96% was formed after exposure to pure CO_2 for 6 months at room temperature.¹⁰⁴ A similar amount ($6.08 \pm 0.52\%$) was also found in the sample LNO-600, since high temperature (600 °C) and long duration (12 h) have been applied to LNO. For Eqn. (4.3), the weight of $\text{Li}_{1-z}\text{Ni}_{1+z}\text{O}_2$ and Li_2CO_3 is heavier than that of LiNiO_2 , so it should be a mass-gaining reaction. However, the TG curve remains steady in the temperature region of 400-600 °C. The constant mass further reveals the influence of duration on the extent of reaction of Eqn. (4.3). In the TG measurement, the temperature was increased with a rate of 5 °C min^{-1} and in such a short time no significant amount of Li_2CO_3 can be formed. However, in the post-synthesis thermal treatment, Li_2CO_3 was continuously formed during the thermal treatment for 12 h.

With the increase of temperature of thermal treatment, the reaction also proceeds to a gradually larger extent. In addition to the increasing amount of Li_2CO_3 , a larger progress of reaction can also be monitored via the strong off-stoichiometry of $\text{Li}_{1-z}\text{Ni}_{1+z}\text{O}_2$. The

stoichiometry varies from $[\text{Li}_{0.95}\text{Ni}_{0.05}]\text{NiO}_2$ for LNO-400 to $[\text{Li}_{0.90}\text{Ni}_{0.10}]\text{NiO}_2$ for LNO-600. The reaction between LNO and CO_2 also likely occurs even before 400 °C, since an off-stoichiometry of $[\text{Li}_{0.96}\text{Ni}_{0.04}]\text{NiO}_2$ has already been found for LNO-300. Li_2CO_3 is not observed by XRD after heating to 300 °C because of the small content. Although no cubic $\text{Li}_y\text{Ni}_{1-y}\text{O}$ phase is observed in the XRD patterns after heating up to 300°C, the reaction described by Eqn. (4.2) can still occur in thin surface regions. This thin cubic layer will be further discussed in the magnetic measurement and TEM parts described below.

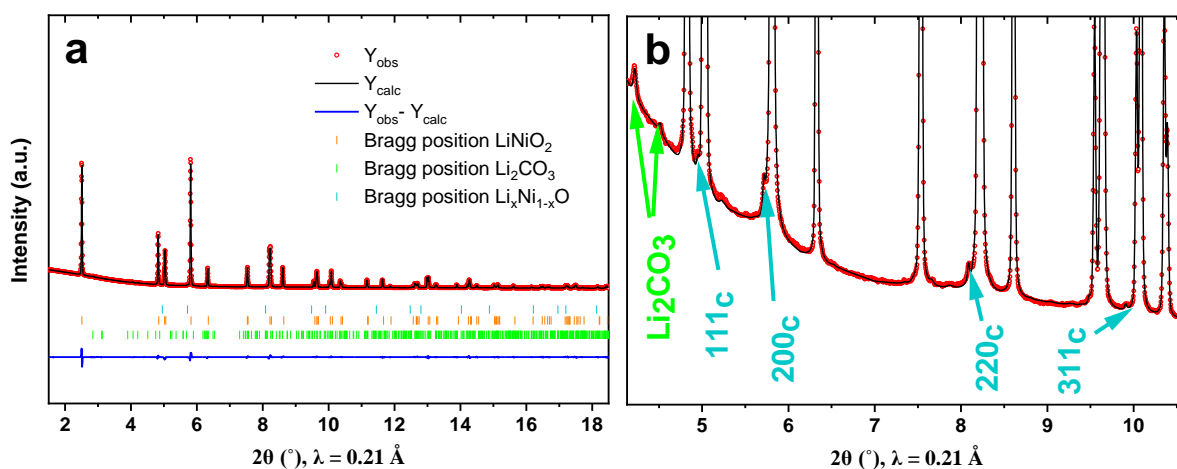


Figure 4.11 (a) XRD Rietveld refinement pattern of LNO-750 and (b) the enlarged view showing the tiny reflections from $\text{Li}_y\text{Ni}_{1-y}\text{O}$ cubic phase.

Interestingly, the off-stoichiometry of LNO-700 ($[\text{Li}_{0.91}\text{Ni}_{0.09}]\text{NiO}_2$) is slightly weaker than that of LNO-600 ($[\text{Li}_{0.90}\text{Ni}_{0.10}]\text{NiO}_2$). This abnormal behaviour is contradictory to the higher reactivity according to Eqn. (4.3) at higher temperatures, but at 700 °C the bulk decomposition of LNO also occurs (following Eqn. (4.1)). This means that part of the formed Li_2O reacts with CO_2 to form Li_2CO_3 and with O_2 to form Li_2O_2 . Li_2O_2 is volatile and could not be observed by XRD. The reaction described by Eqn. (4.3) was partially suppressed, since less Li_2CO_3 ($5.29 \pm 0.63\%$) was found when compared to LNO-600 ($6.08 \pm 0.52\%$). Eqns. (4.1) and (4.3) describe competitive reactions. Although the decomposition of LNO starts at around 700 °C, it proceeds three times quicker at 800 °C.⁴¹ The suppressed reaction described by Eqn. (4.3) and sluggish rate of the reaction described by Eqn. (4.1) jointly induce the weak off-stoichiometry for LNO-

700. As a special sample, LNO-700 will be compared to LNO-600 and the detailed difference in Ni^{2+} location will be analyzed in the NMR and magnetic measurement parts described below.

For LNO-750, as revealed by the Rietveld refinement shown in **Figure 4.11**, the reaction between LNO and CO_2 is further suppressed (indicated by the smaller amount of Li_2CO_3 ($4.07 \pm 0.97\%$)), since the decomposition described by Eqn. (4.1) proceeds at a faster rate at $750\text{ }^\circ\text{C}$. The increased rate of decomposition results in the strongest off-stoichiometry of $[\text{Li}_{0.88}\text{Ni}_{0.12}]\text{NiO}_2$ for LNO-750. The distribution of off-stoichiometry is likely inhomogeneous through the particle, but not observable by the XRD refinement. The strong off-stoichiometry may lead to a fully cubic phase at the surface, as displayed in **Figure 4.11b**. Some tiny reflections belonging to the $\text{Li}_y\text{Ni}_{1-y}\text{O}$ cubic phase appear in addition to the ones from LNO.

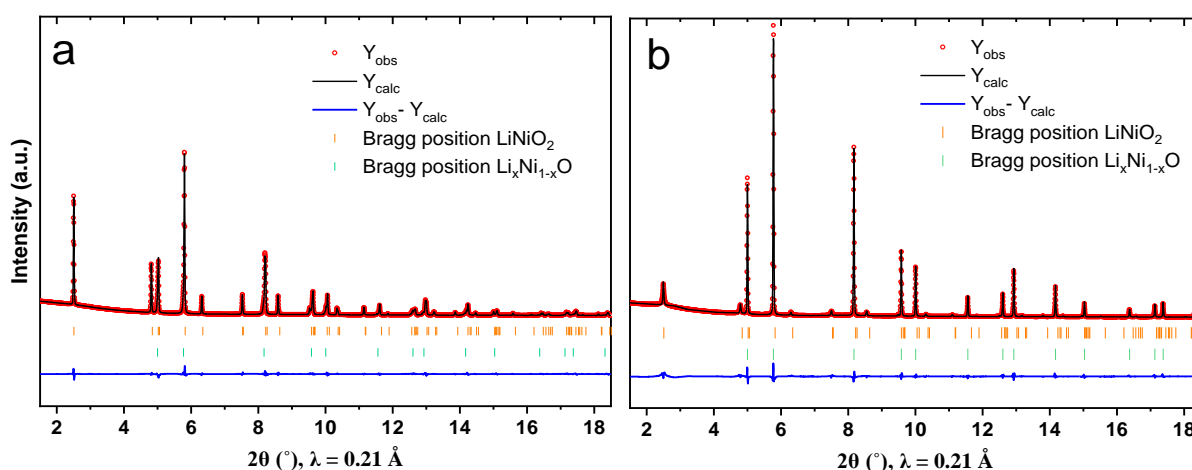


Figure 4.12 XRD Rietveld refinement pattern of (a) LNO-800 and (b) LNO-850.

In the third temperature region (from 800 to $1000\text{ }^\circ\text{C}$, region (III)), Li_2CO_3 disappears and the decomposition proceeds more rapidly. When the temperature of the thermal treatment surpasses $750\text{ }^\circ\text{C}$ (melting point of Li_2CO_3 is $720\text{ }^\circ\text{C}^{105}$) Li_2CO_3 would be completely melted and penetrated into the alumina container used for synthesis. Rietveld refinement against XRD patterns of LNO-800 and LNO-850 are shown in **Figure 4.12**. The cubic phase amounts to $15.2 \pm 0.4\%$ for LNO-800 and $88.3 \pm 1.0\%$ for LNO-850 of the whole sample material. LNO-800 represents the sample with the highest temperature of heat treatment that still allows to determine the off-stoichiometry ($[\text{Li}_{0.81}\text{Ni}_{0.19}]\text{NiO}_2$) in the layered phase. For LNO-850, the fraction of the layered phase is too small to conduct a reliable refinement on the value of z in

$\text{Li}_{1-z}\text{Ni}_{1+z}\text{O}_2$. For LNO-1000, broader reflections compared to those of the LNO phase that can be ascribed to a cubic $\text{Li}_y\text{Ni}_{1-y}\text{O}$ phase were observed. This broadening originates from several modifications of the same phase with slightly different lithium contents and lattice parameters. When doing the refinement, the fitting degree could be further improved when more of these similar models were used (**Figure 4.13**). It could be reasonably assumed that there is a certain lithium concentration gradient in this material. On the contrary, the reflections from NiO are very sharp and can be well described by the single NiO model (NiO is prepared by calcining NiOH directly at 1000 °C, **Figure 4.14**)

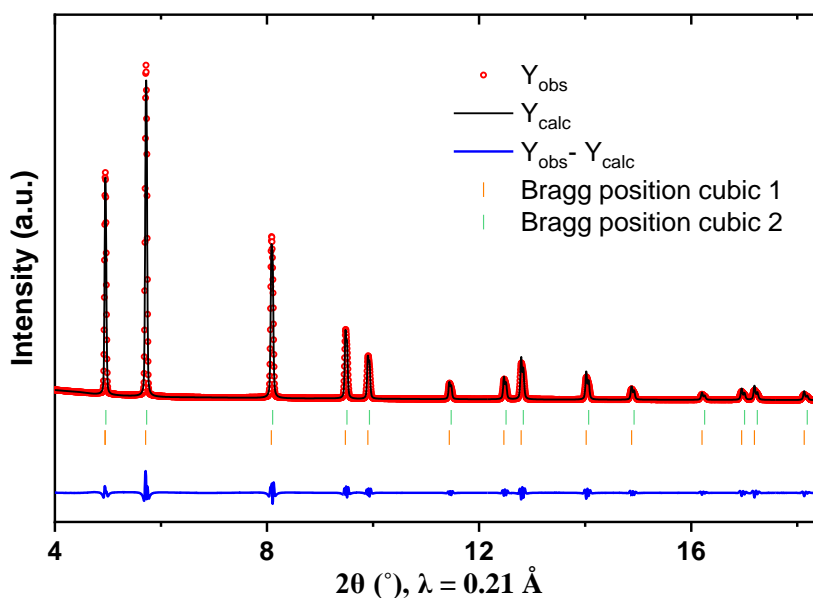


Figure 4.13 The XRD Rietveld refinement pattern of LNO-1000.

To check our assumption and investigate the reversibility of structural changes, an additional series of experiments was performed. Samples heated in air at 400, 600, and 800 °C were reheated in pure oxygen at 700 °C for 12 h. The reheated LNO-400 and LNO-600 samples return to the pristine state with similar Ni occupancy values on Li sites and performance (**Figure 4.15**). The off-stoichiometric $\text{Li}_{1-z}\text{Ni}_{1+z}\text{O}_2$ phase could be recovered with surface Li_2CO_3 decomposing and Li ions entering into the layered lattice again. These findings reveal that there is no lithium evaporation at least until 600 °C. For LNO-800, the phase transition to the cubic structure already happened with severe O and Li loss. As a result, the reheated sample could not recover to the original state. Its capacity is only 140 mAh g^{-1} for the first cycle.

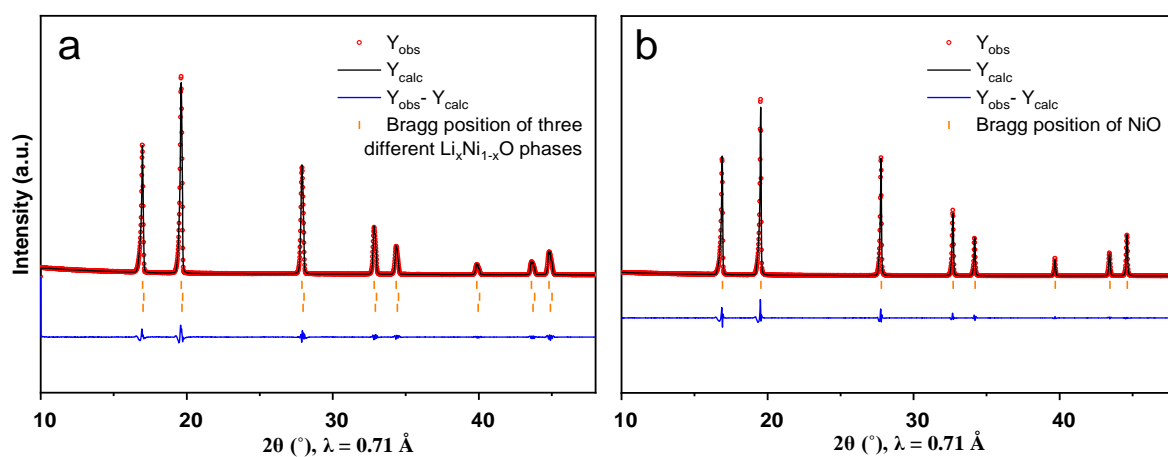


Figure 4.14 The comparison of refinement against XRD patterns of (a) LNO-1000 and (b) $\text{Ni}(\text{OH})_2$ -1000 using a molybdenum source.

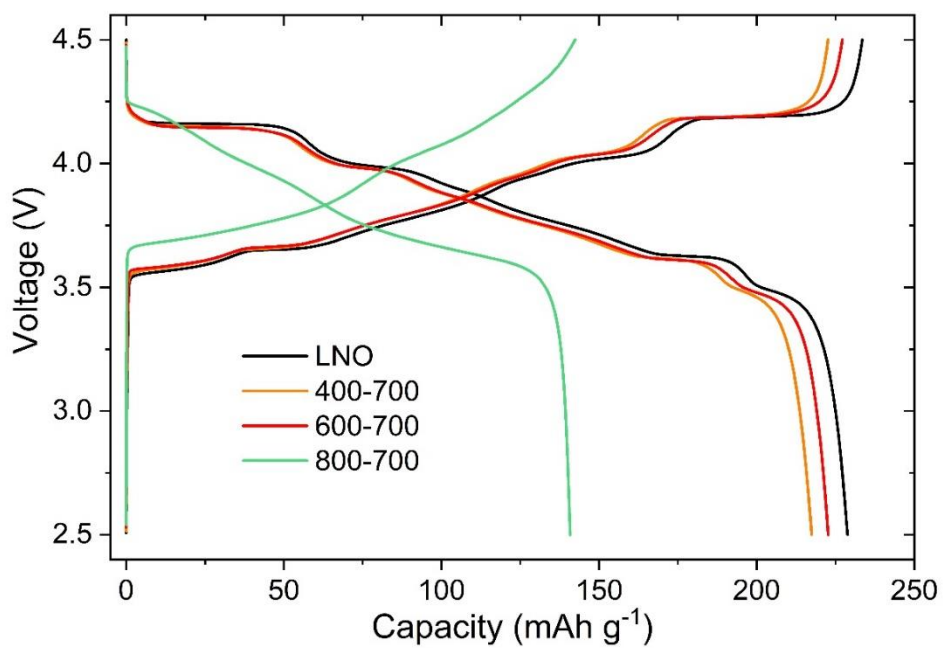


Figure 4.15 The electrochemical performance of LNO-400, 600, and 800 °C samples reheated at 700°C.

4.3.3 *In situ* high-temperature XRD

In situ XRD during heating was performed to trace the structural changes with increasing temperature. Therefore, quartz capillaries were filled with as-prepared LNO powder and were heated from room temperature to 900 °C (**Figure 4.16**). Normally, XRD patterns were collected every 50 °C except for the high-temperature region (750-900 °C), where the interval was set to 25 °C. The change of phase composition is shown in **Figure 4.17** based on the Rietveld refinement against XRD patterns. From room temperature to 600 °C, the original layered phase persists. The lattice parameters keep increasing because of the thermal expansion. When compared with *ex situ* XRD data, z in $\text{Li}_{1-z}\text{Ni}_{1+z}\text{O}_2$ increases at a lower rate (**Figure 4.3.18**) since the temperature was increased at a higher rate (20 °C min^{-1}) for the *in situ* XRD data and the holding time at each temperature is only 10 min. Under these circumstances, only a small amount of LNO could react with CO_2 and therefore Li_2CO_3 could not be observed, unlike in the *ex situ* measurements performed after heating to 400 to 600 °C. At 650 °C, new reflections assigned to Li_4SiO_4 are identified (**Figure 4.3.19a**). This compound is formed by the reaction between SiO_2 from the quartz capillary and Li_2O :

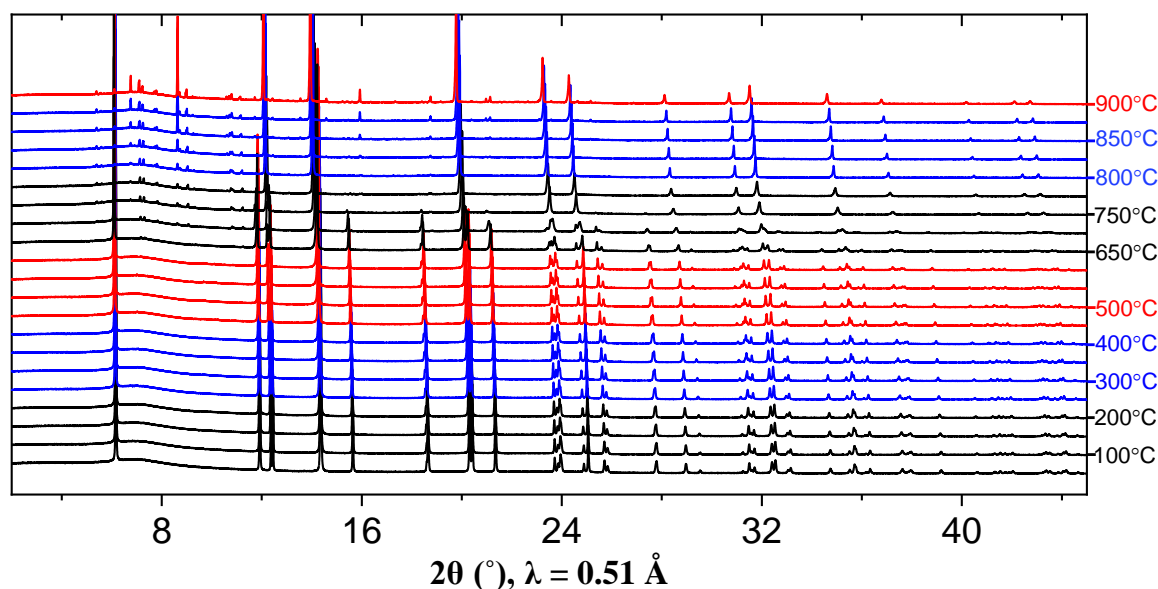


Figure 4.16 *In situ* high temperature XRD of LNO in air from room temperature to 900 °C.

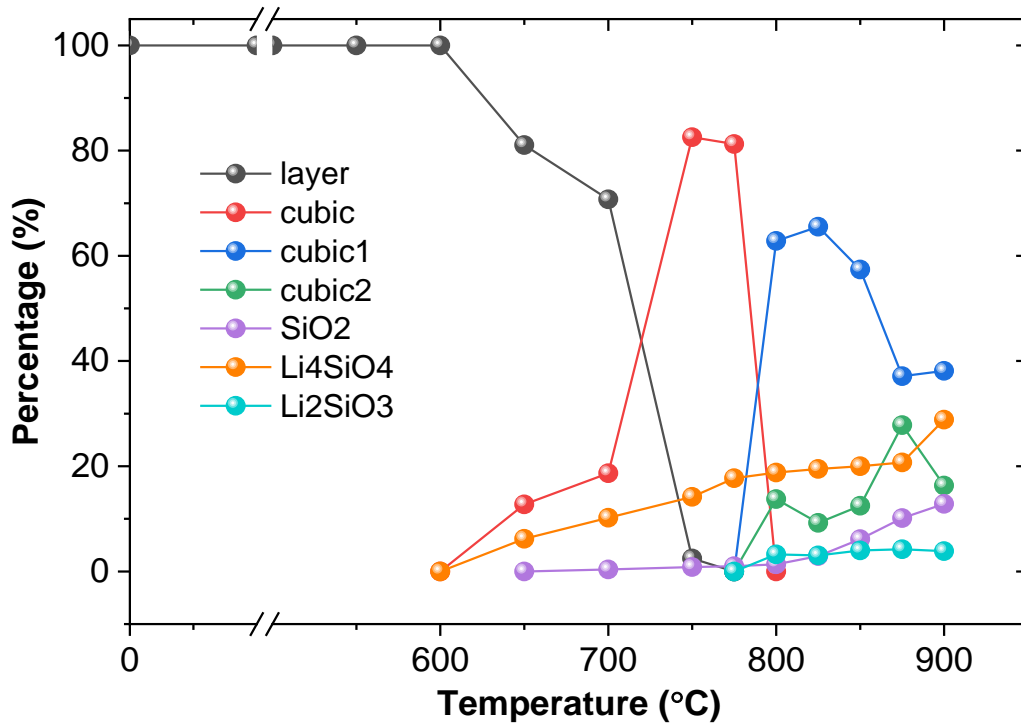


Figure 4.17 The change of phase composition obtained from the refinement against in situ XRD patterns acquired during heating.

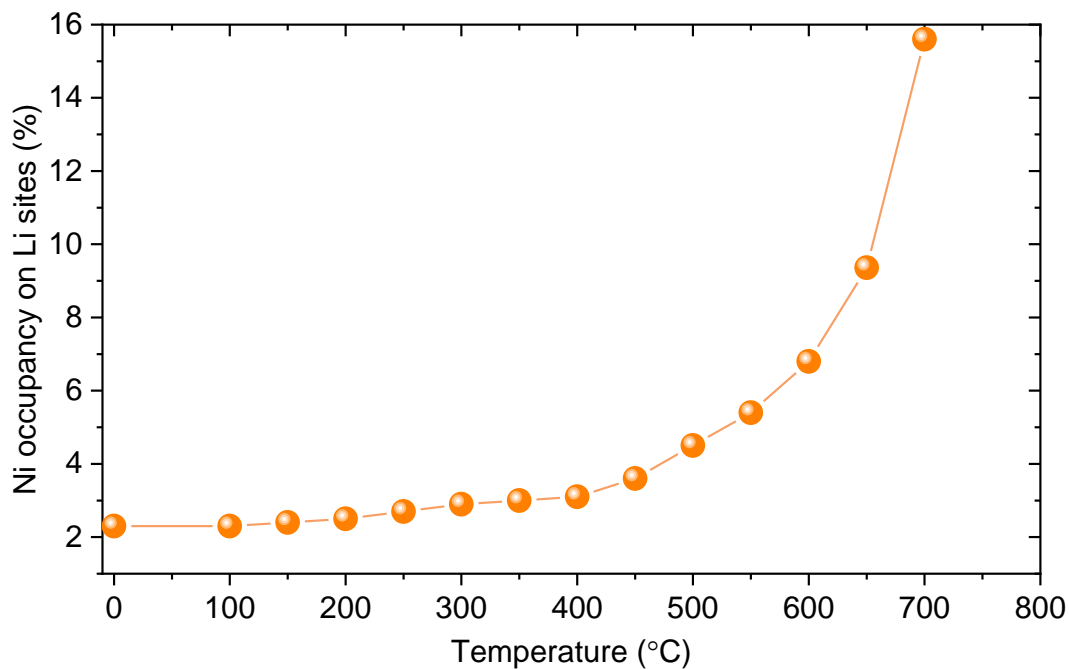


Figure 4.18 The value of Ni occupancy on Li sites obtained from refinement against in situ XRD patterns acquired during heating.

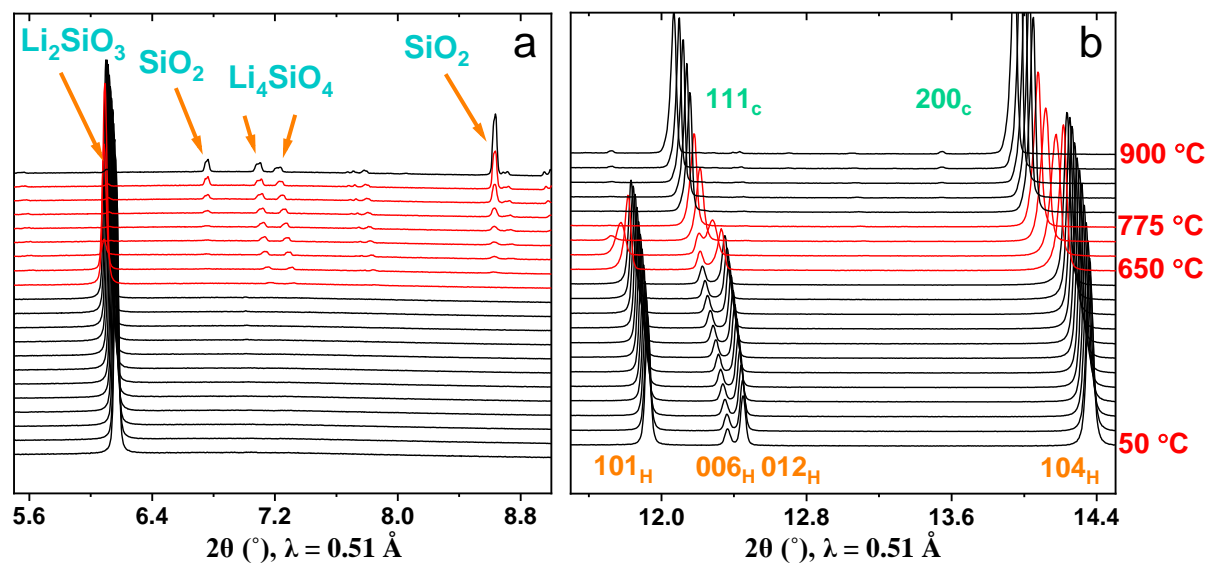


Figure 4.19 (a) Enlarged regions of in situ XRD pattern focusing on the impurities and (b) the change of 101, 006, 012, and 104 reflections during heat treatment. The temperature regions showing impurity formation and phase transition are marked with red color in (a) and (b), respectively.

Meanwhile, the cubic phase $\text{Li}_y\text{Ni}_{1-y}\text{O}$ also appears at 650 °C with a weight fraction of $13.5 \pm 0.3\%$. The indication for the $\text{Li}_y\text{Ni}_{1-y}\text{O}$ phase comes from what looks like an asymmetry of a series of reflections (such as 104) and the disappearance of diffraction splitting (such as 006 and 012). The cubic phase contributes to the 200 reflection at 2θ angles slightly smaller than those of 104 and 111 reflections and results in the merge of the 006 and 012 reflections (**Figure 4.19b**). Note that the formation of Li_4SiO_4 (Eqn. (4.4)) proves that Li_2O is leached out of LNO during decomposition. Meanwhile, the silicate formation (Eqn. (4.4)) also accelerates the decomposition process (Eqn. (4.1)) by continuously consuming the by-product Li_2O . This explains why the $\text{Li}_y\text{Ni}_{1-y}\text{O}$ phase appears much earlier than in the *ex situ* measurement (at 650 °C for *in situ* and at 750 °C for *ex situ* data). At 700 °C, crystalline SiO_2 appears. The lattice parameter of the cubic phase keeps increasing because the Li content in $\text{Li}_y\text{Ni}_{1-y}\text{O}$ is decreasing.⁴¹ Interestingly, at 800 °C the cubic phase divides into two compositions with different Li amounts (**Figure 4.20**). The Li-poor phase should correspond to the outer region of the particles. Another lithium polysilicate (Li_2SiO_3) also forms at this temperature, possibly because there is not enough lithium to form Li_4SiO_4 exclusively. The XRD pattern of LNO-900 with refinement is given in **Figure 4.20** with five phases in total. In summary, the main tendencies of phase transitions are similar to the results obtained from *ex situ* data.

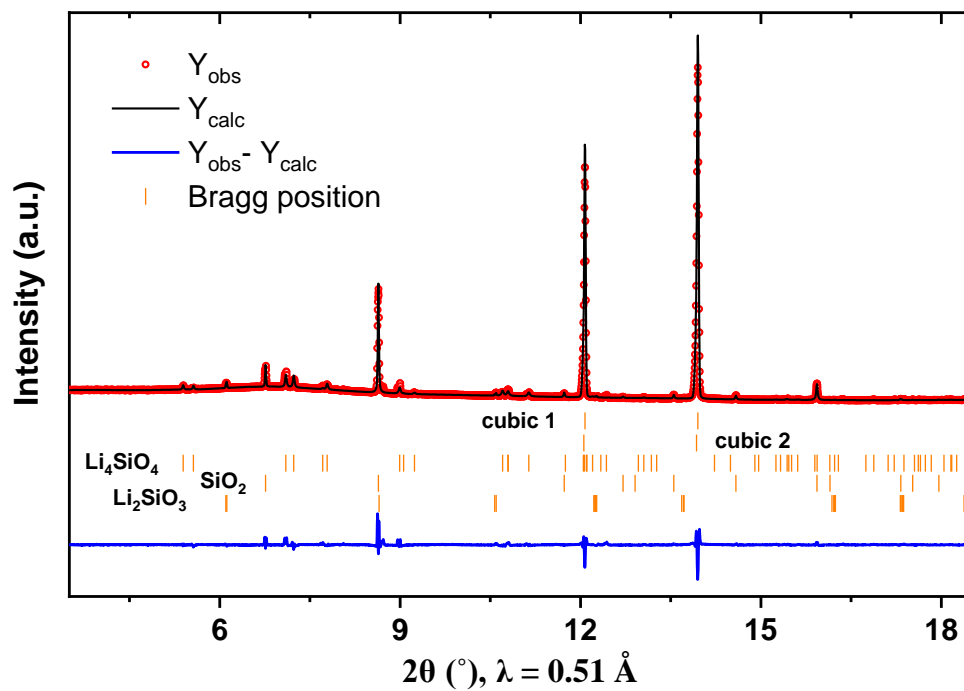


Figure 4.20 The refinement against the XRD pattern of LNO-900 acquired during heating. Five phases are added to fit the pattern.

4.3.4 Ex situ NMR

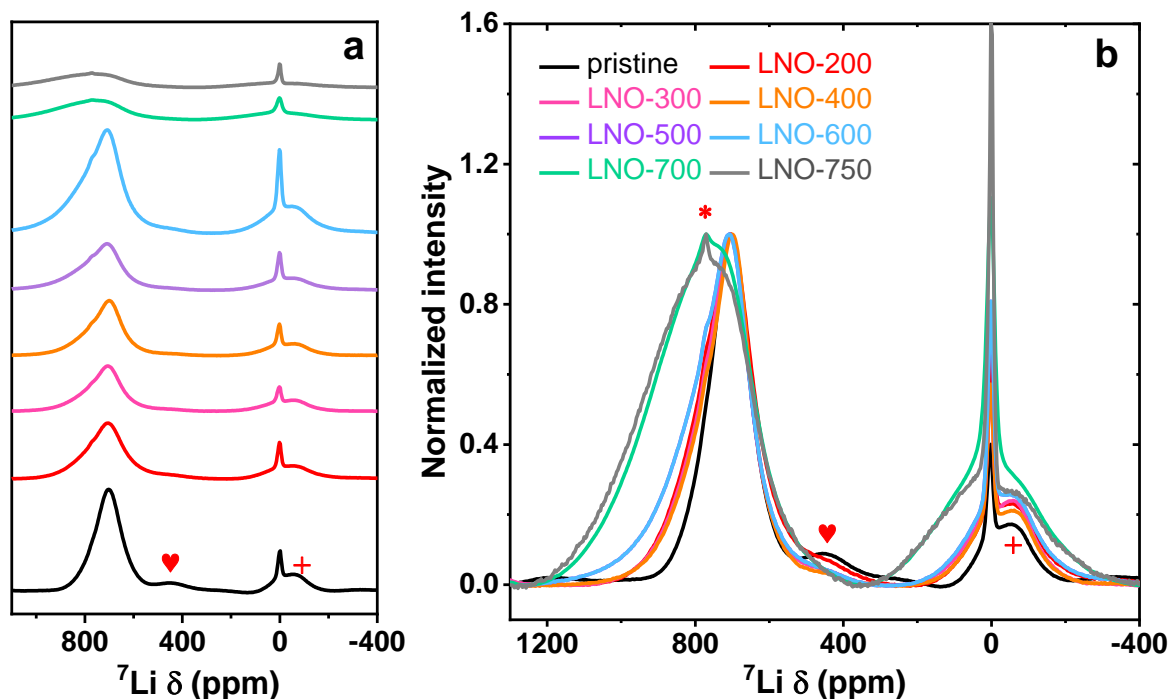


Figure 4.21 ^7Li NMR spectra of pristine LNO and some thermally treated samples. (a) The spectra are stacked with original intensities. The small peak at 425 ppm is labelled with the red heart. (b) The intensity is normalized via the maximum value of the main peak. Asterisks and plus signs indicate the position of spinning sidebands.

Solid state NMR is a very useful tool to investigate the coordination environment of Li. The ^7Li NMR shift or hyperfine shift is influenced by the surrounding paramagnetic TM ions mainly by Fermi-contact interaction.⁷⁵ Paramagnetic ions in the first and the second cation coordination shell of Li will induce different NMR shifts. Two different coordinations are distinguished by the bond angle at the bridging oxygen atoms, namely 90° and 180° bond neighbours. Furthermore, we can expect two paramagnetic species: Ni^{2+} and Ni^{3+} and therefore four different types of bonds for LNO that contribute to the overall NMR shift. Although the exact shift values for each bond contribution are not clear, good estimates can be obtained from results on NCM811: Ni^{2+} (90°): -30 ppm, Ni^{3+} (90°): -15 ppm, Ni^{2+} (180°): 170 ppm, and Ni^{3+} (180°): 110 ppm).⁴⁷ Generally speaking, the reduction of Ni^{3+} to Ni^{2+} will induce a left shift in the spectra.

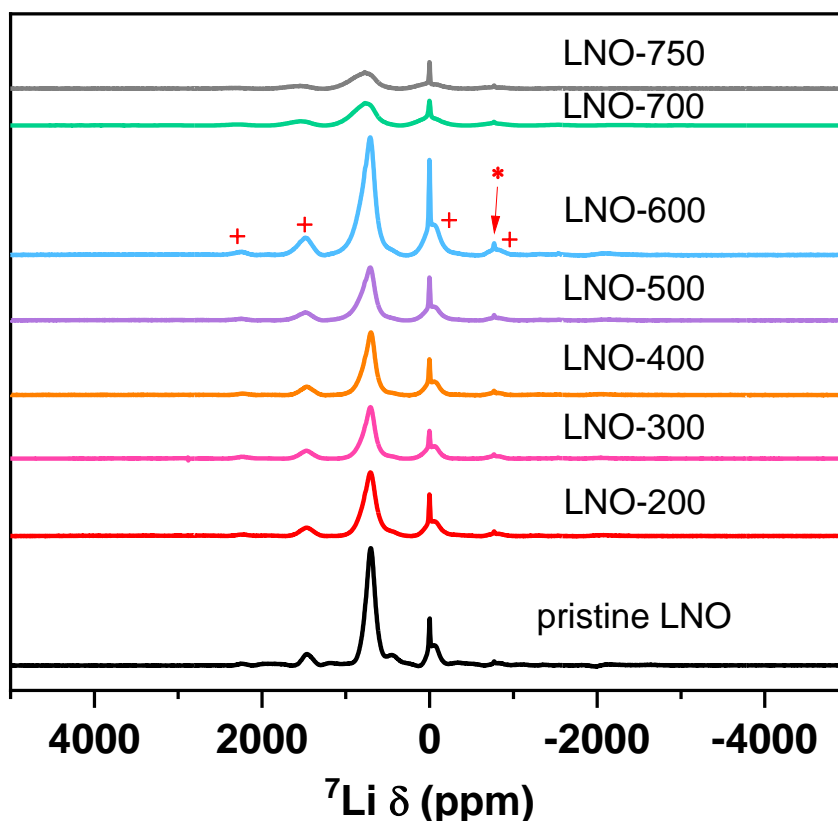


Figure 4.22 The extended range of ${}^7\text{Li}$ MAS NMR spectra including all sidebands. The plus sign denotes the sidebands belonging to the isotropic peak at 700 ppm and the asterisk labels the sidebands belonging to the peak at 0 ppm associated with diamagnetic lithium salts on the surface.

To investigate the change of local environments, *ex situ* ${}^7\text{Li}$ NMR spectra of thermally treated samples were measured (**Figure 4.3.21**). To easily make comparisons on peak shifting, some of the spectra were normalized based on the maximum intensity of the main peaks as shown in **Figure 4.21b**. For pristine LNO, the signal is located at around 700 ppm. This large NMR shift can be explained by the local Li environment consisting of twelve Ni^{3+} next-nearest neighbors, six times linked to Li via 90° oxygen bonds and six times linked to Li via 180° oxygen bonds. For an ideal arrangement with only Ni^{3+} in the structure and no Li-Ni site exchange, this is the only possible environment around Li. After the replacement of small amounts of Ni^{3+} by Ni^{2+} , $a\text{Ni}^{3+}b\text{Ni}^{2+}$ ($a+b = 12$) combinations occur with smaller probability and contribute to the widening of signals. Indeed, the NMR shift for pure Ni^{3+} would be 570 ppm ($6 \times 110 \text{ ppm} + 6 \times (-15 \text{ ppm})$) if expected values from Ni^{3+} in NCM811 are applied. This difference possibly originates from the influence of Mn on the hyperfine shift in NCM811. There is also a small

peak located at 425 ppm labelled with a red heart, which could be ascribed to a Ni-rich rocksalt phase or Li occupancy on Ni sites.³¹ This rock salt phase is electrochemically active and reported to disappear during Li de-intercalation.¹⁰⁶ The sharp, narrow peak at 0 ppm originates from diamagnetic impurities such as LiOH and Li₂CO₃.¹⁰⁷ Two different sets of spinning sidebands are labelled with asterisks and plus signs in the spectra. The plus sign denotes the sidebands belonging to the isotropic peak at 700 ppm and the asterisk labels the sidebands belonging to the peak at 0 ppm associated with diamagnetic lithium salts on the surface. The extended range of ⁷Li MAS NMR spectra including all sidebands is given in **Figure 4.22**.

With increasing heat-treatment temperatures, there is no strong change in the shape of the ⁷Li NMR spectra until 600 °C. However, the NMR peak is already slightly shifted to higher ppm positions for LNO-200. Already for this sample, a slightly peak widening can be found after heat treatment. As discussed in the XRD part, the reaction between LNO and CO₂ could occur slowly even at 200 °C following Eqn. (4.3). When $\frac{z}{2(1+z)}$ mol O₂ is formed, $\frac{2z}{1+z}$ mol Ni³⁺ is reduced to Ni²⁺. This reduced Ni²⁺ could induce changes in the NMR shift (-15 ppm for 1 Ni³⁺ replaced by 1 Ni²⁺ (90°) and +60 ppm for 1 Ni³⁺ replaced by Ni²⁺ (180°)). There are no big changes between the spectra of LNO-200, LNO-300, and LNO-400, in accordance with a slow rate of the reaction described by Eqn. (4.3). The spectra of LNO-500 and LNO-600 look similar, the peaks becoming broader with additional intensity at higher ppm values. As discussed in the XRD part, the increase of Li₂CO₃ content and *z* value in Li_{1-z}Ni_{1+z}O₂ indicate that the reaction described by Eqn. (4.3) proceeds to a larger extent. Some Li ions therefore are surrounded with more reduced Ni²⁺ ions. Meanwhile, the intensity of the peak at around 0 ppm also increases in intensity in the temperature region of 400-600 °C (**Figure 4.21b**), in accordance with the continuous formation of Li₂CO₃ observed with XRD. For LNO-700, the ⁷Li NMR peak shows a further strong broadening toward higher ppm values. Based on the XRD refinement, the off-stoichiometry of LNO-700 ([Li_{0.91}Ni_{0.09}]NiO₂) is very similar to that of LNO-600 ([Li_{0.90}Ni_{0.10}]NiO₂). This means that the Ni occupancy on the Li site is not the reason for the broadening and, on average, left-shift of the NMR peak observed for LNO-700. The broadening could be ascribed to the formation of more Ni²⁺ during LNO decomposition, as evidenced by XAS, see below. Interestingly, based on Eqn. (4.1), half of the reduced Ni²⁺ should occupy the Li vacancies and induce a stronger off-stoichiometry. That is contradictory to the XRD refinement result. Two possible assumptions could explain this inconsistency: (*i*) during the decomposition process, although Li vacancies are formed by the formation of Li₂O, not all of them are occupied by the Ni²⁺ but Ni²⁺ is preferentially found in the Ni layer. There is no clear

correlation between off-stoichiometry of $\text{Li}_{1-z}\text{Ni}_{1+z}\text{O}_2$ and Ni reduction anymore. (ii) Another assumption is that, still in agreement with Eqn. (4.1), Ni^{3+} in the Ni layer is preferentially reduced in the Li-O-Ni 180° configuration. Ni^{2+} (180°) has a larger contribution to the NMR shift than Ni^{2+} (90°). The first assumption is more likely and is investigated in detail by magnetic measurements described below. For LNO-750, the spectrum is almost identical to that of LNO-700 with a slightly broader peak width. The large difference in off-stoichiometry ($[\text{Li}_{0.88}\text{Ni}_{0.12}]\text{NiO}_2$ for LNO-750 and $[\text{Li}_{0.91}\text{Ni}_{0.09}]\text{NiO}_2$ for LNO-700) again is not reflected by the ^7Li NMR spectra. As shown in **Figure 4.23**, the spectrum of LNO-800 has a slightly larger line width compared to that of LNO-750 and shows a clear left shift (from 799 to 946 ppm). This indicates that the decomposition proceeds at a larger rate and extent. The maximum probability of local Li environments has changed to those with more Ni^{2+} for the first time. For LNO-850, extreme broadening and weak NMR signals are observed, since the cubic structure is already present with a weight fraction of $88.3 \pm 1.0\%$. Strongly off-stoichiometric $\text{Li}_{1-z}\text{Ni}_{1+z}\text{O}_2$ with a high amount of Ni^{2+} and thus many different $\text{Ni}^{2+}/\text{Ni}^{3+}$ environments around Li in the remaining layered phase induces enormous broadening. For LNO-1000 that contains exclusively cubic $\text{Li}_y\text{Ni}_{1-y}\text{O}$, as evidenced from XRD, the broad component in the spectrum disappears and a very small peak at 27 ppm remains. In accordance with the XRD refinement, some Li ions in LNO-1000 are retained in the lattice and also a small amount of Ni^{3+} to keep charge neutrality. The disappearance of the broad contribution might just be related to an even stronger broadening caused by more Ni^{2+} . The very small peak at 27 ppm has a larger width than the peaks close to 0 ppm observed for the lower heating temperatures. This might hint at a diamagnetic phase, such as Li_2O , in close proximity to paramagnetic particles like the cubic $\text{Li}_y\text{Ni}_{1-y}\text{O}$. In summary, the change of NMR shifts mainly reflects the Ni reduction process in the layered phase.

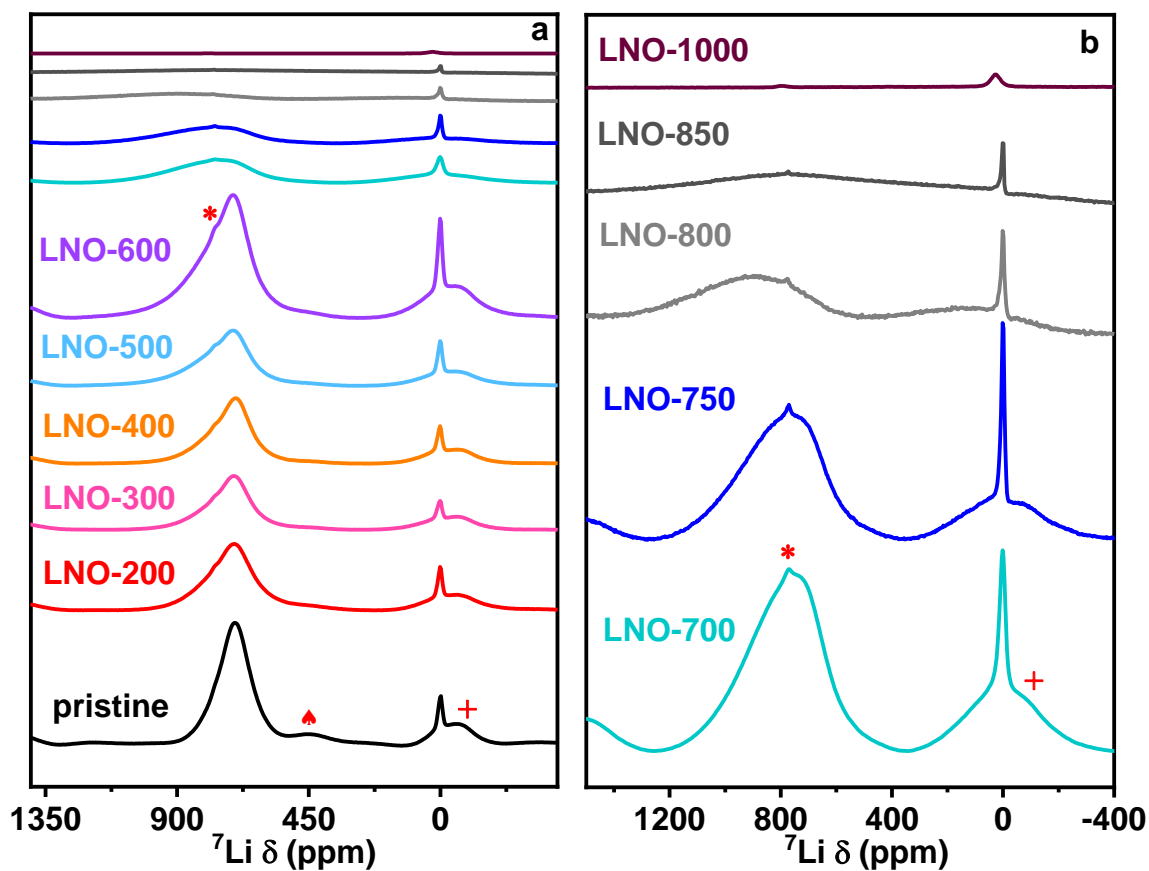


Figure 4.23 (a) NMR spectra of pristine LNO and all thermally treated samples. (b) LNO-700 and LNO-1000 are separately further replotted to show the details. The small peak located at 425 ppm is labelled with a heart. Two different sets of spinning sidebands are labelled with plus and asterisks in the spectra, separately.

4.3.5 Ex situ XAS

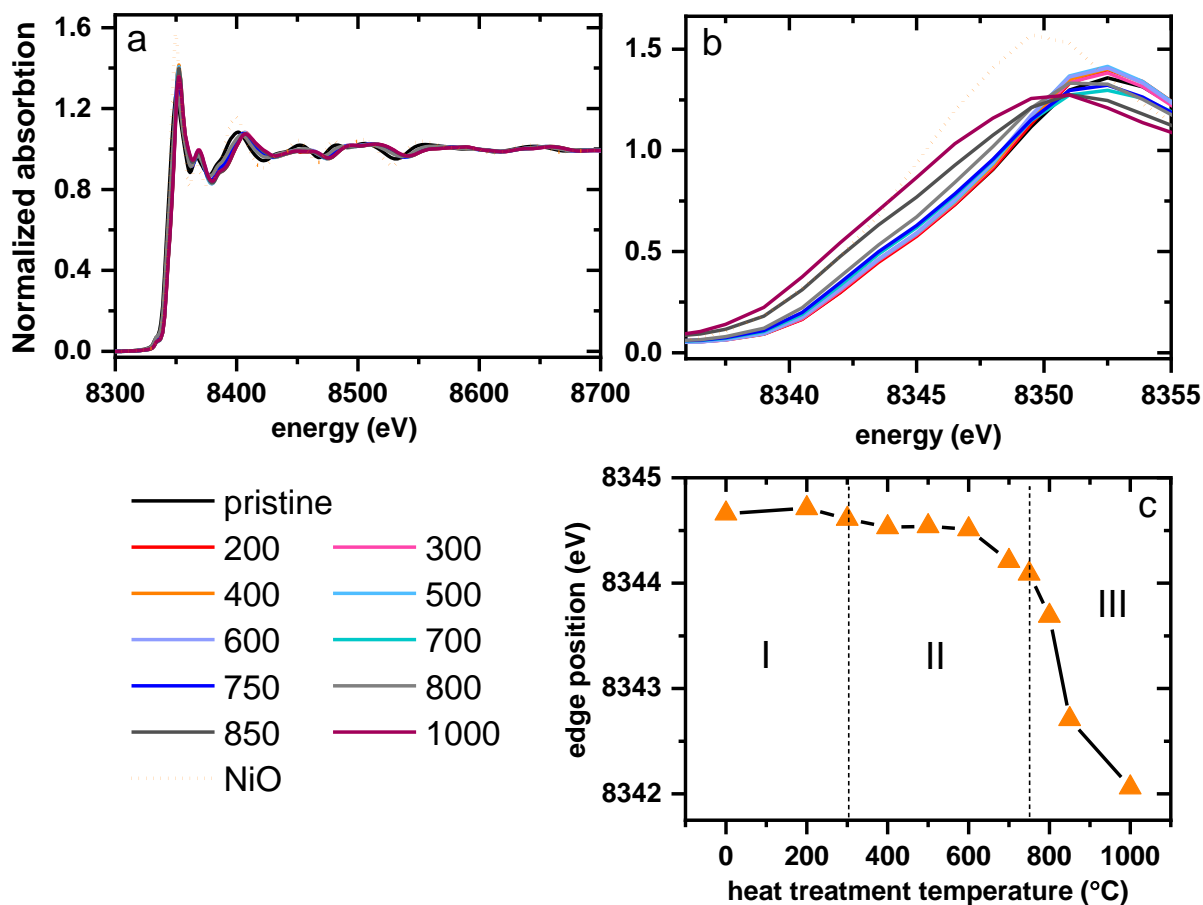


Figure 4.24 Ni K-edge XAS spectra of the pristine and heat-treated LNO samples and (b) the enlarged view of the edge region. (c) the edge position as defined by the energy where the edge crosses the value 0.55.

To capture the Ni reduction process, *ex situ* XAS was performed on LNO and heat-treated samples (**Figure 4.24a, b**). The Ni K absorption edge shifts toward lower energy with increasing heat treatment temperatures, revealing the successive reduction from Ni^{3+} to Ni^{2+} . However, the rate of reduction is not constant. To clearly show the change in rate, the edge position, defined as the position where the normalized spectrum reaches the value 0.55, is plotted as a function of heating temperature in **Figure 4.24c**. From the pristine state to 600 °C, there is only slight changes in the position of the Ni K absorption edge. In this temperature region, LNO reacts with CO_2 and the slight Ni reduction could also be reflected by the increased z value in the $\text{Li}_{1-z}\text{Ni}_{1+z}\text{O}_2$ phase. A more obvious change in edge position occurs between the

spectra of LNO-600 and LNO-700. As suggested by the ^7Li NMR spectra, more Ni^{2+} is formed during the LNO decomposition at 700 °C and a large fraction is located in the Ni layers. When the heating temperature reaches 800 °C, the rate of Ni reduction increases, corresponding to the phase transformation to $15.2 \pm 0.4\%$ $\text{Li}_y\text{Ni}_{1-y}\text{O}$ phase. A strong shift in edge position occurs when comparing the spectra of LNO-800 and LNO-850. Most of the Ni^{3+} has been reduced to Ni^{2+} accompanied by the drastic Li and O loss and phase transition to a large extent ($88.3 \pm 1.0\%$). Finally, a pure $\text{Li}_y\text{Ni}_{1-y}\text{O}$ phase is formed in LNO-1000 with further O loss. There is a difference in the spectra of LNO-1000 and standard NiO samples, since a small amount of Ni^{3+} is still maintained to keep the charge neutrality. In summary, a massive reduction of Ni ions is the driving force for the phase transitions.

4.3.6 Magnetic measurements

Ni ions in hypothetical stoichiometric LNO are exclusively present as Ni^{3+} ions with d^7 electronic configuration. In octahedral coordination the crystal field splitting results in $(t_{2g})^6(e_g)^1$ occupation with one unpaired electron ($S = 1/2$) that corresponds to an effective paramagnetic spin-only magnetic moment of $\mu_{\text{eff}}^{\text{Ni}^{3+}} = 2\sqrt{1/2(1/2 + 1)}\mu_B = 1.73\mu_B$ and a spin-only z-component magnetic moment of $\mu_z^{\text{Ni}^{3+}} = 2 \cdot S \mu_B = 1 \mu_B$. Reduction to Ni^{2+} leads to $(t_{2g})^6(e_g)^2$ electronic configuration with two unpaired electrons coupled to $S = 1$ that corresponds to an effective paramagnetic spin-only magnetic moment of $\mu_{\text{eff}}^{\text{Ni}^{2+}} = 2.83\mu_B$ and a spin-only z-component magnetic moment of $\mu_z^{\text{Ni}^{2+}} = 2 \mu_B$. As can be inferred from the ZFC/FC curves all shown individually in **Figure 4.25** (FC curves are put together in **Figure 4.26a**) all samples, except for LNO-1000, exhibit a (predominantly) Langevin paramagnetic region at higher temperature that is caused by localized magnetic moments formed by the unpaired electrons of the Ni d electrons. It is characterized by a Curie-Weiss behaviour with inverse dependence of magnetization on temperature. LNO-1000 exclusively consists of cubic NiO phase that orders antiferromagnetically at high Néel temperature $T_N = 524 \text{ K}^{107}$ and therefore does not show paramagnetic behaviour within the investigated temperature region. At lower temperatures a bifurcation of the ZFC and FC branches, indicative for the presence of a ferrimagnetic order (see discussion below) can be observed with a strong dependence of the temperature of bifurcation on the temperature of heat treatment. For LiNiO_2 in the pristine state the horizontal FC branch rather points to the existence of a spin glass behaviour.¹⁰⁸ The evolution of the parameters extracted from the magnetization measurements can be subdivided into the same three regions according to the temperatures of heat treatment as introduced above. As a first parameter of interest, the temperature T_B as onset of a bifurcation of the ZFC and FC curve, arbitrarily defined here as the temperature where the difference of the magnetic susceptibilities of the ZFC and the FC curves exceeds $2 \cdot 10^{-7} \text{ m}^3 \text{ mol}^{-1}$, was determined and is plotted in **Figure 4.26b**. In region (I) T_B is comparably small with values slightly varying around 10 K. Region (II) is characterized by a significant increase of T_B with maximal values for LNO-500 and LNO-600 and a decrease again for LNO-700 and LNO-750. Region (III) is characterized by a tremendous increase of T_B for LNO-800 again. **Figure 4.26c** presents the field scans measured at 2 K and 300 K up to $7 \cdot 10^4 \text{ Oe}$ (a series of the individual field scans at 2 K to illustrate more clearly the evolution of the coercivity fields is given in **Figure 4.27**).

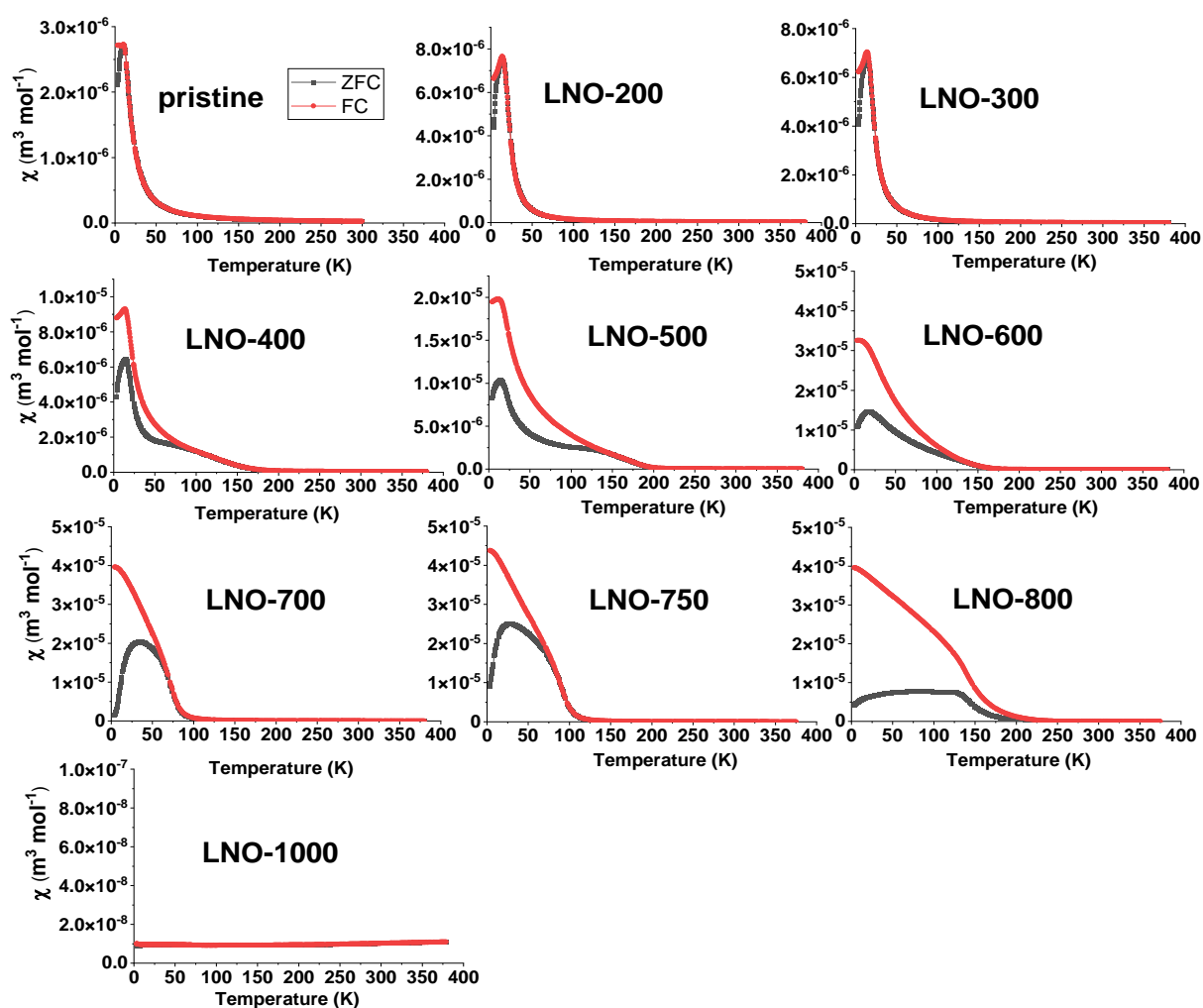


Figure 4.25 ZFC/FC curves of pristine and heat-treated samples measured at 5000 Oe.

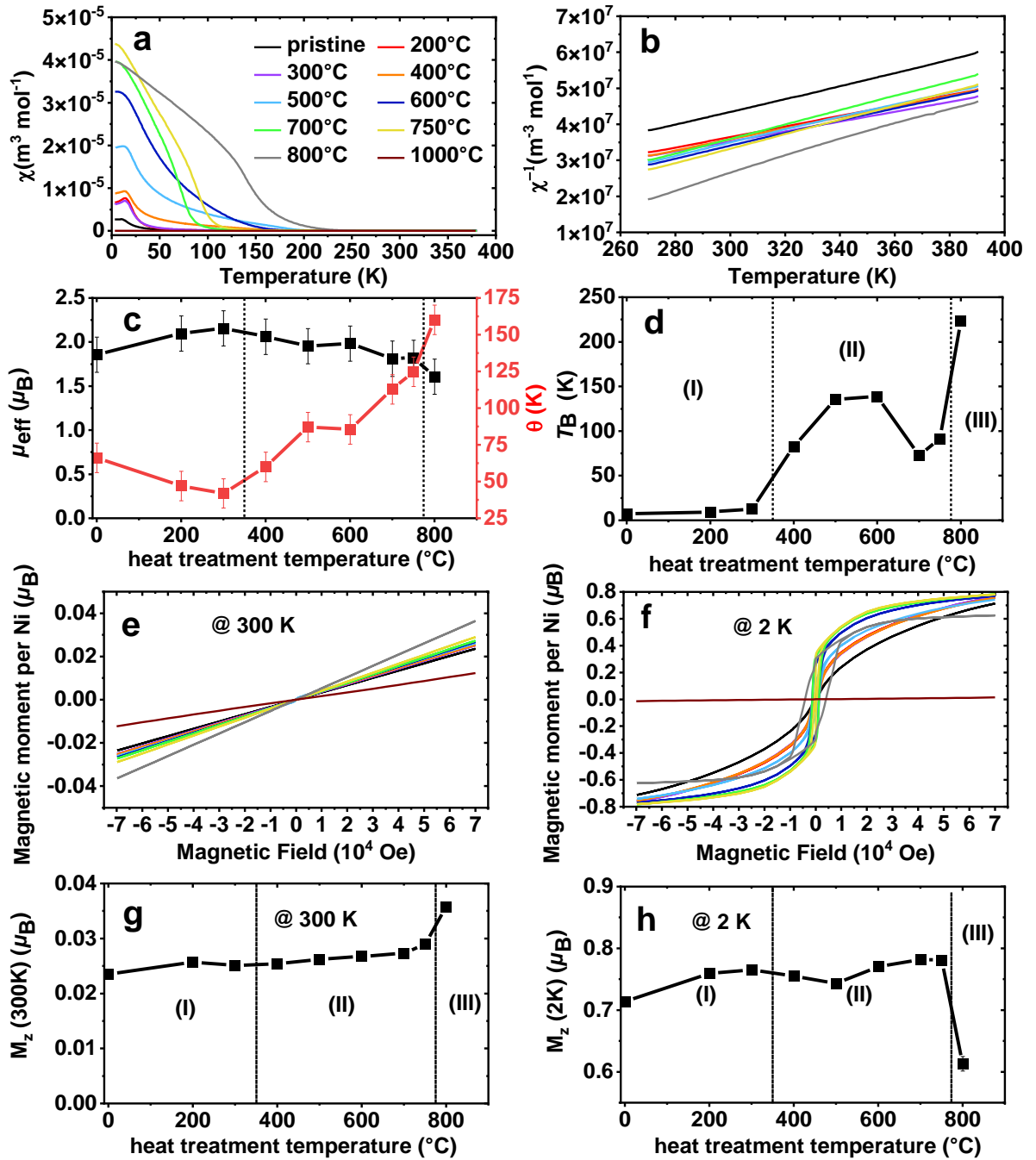


Figure 4.26 (a) FC curves and (b) the change of parameter T_B of the pristine and heat-treated samples. (c) The field scans measured at 300 K up to $7 \cdot 10^4$ Oe and (d) the corresponding z-component magnetization M_z (300K). (e) The field scans measured at 2 K up to $7 \cdot 10^4$ Oe and (f) the corresponding z-component magnetization M_z (2K). (g) The high-temperature inverse susceptibility χ^{-1} measured at 5000 Oe where the part from 340 K to 390 K was used for Curie-Weiss fits and (h) the effective paramagnetic moments μ_{eff} in units of Bohr's magneton μ_B , and Weiss constant θ .

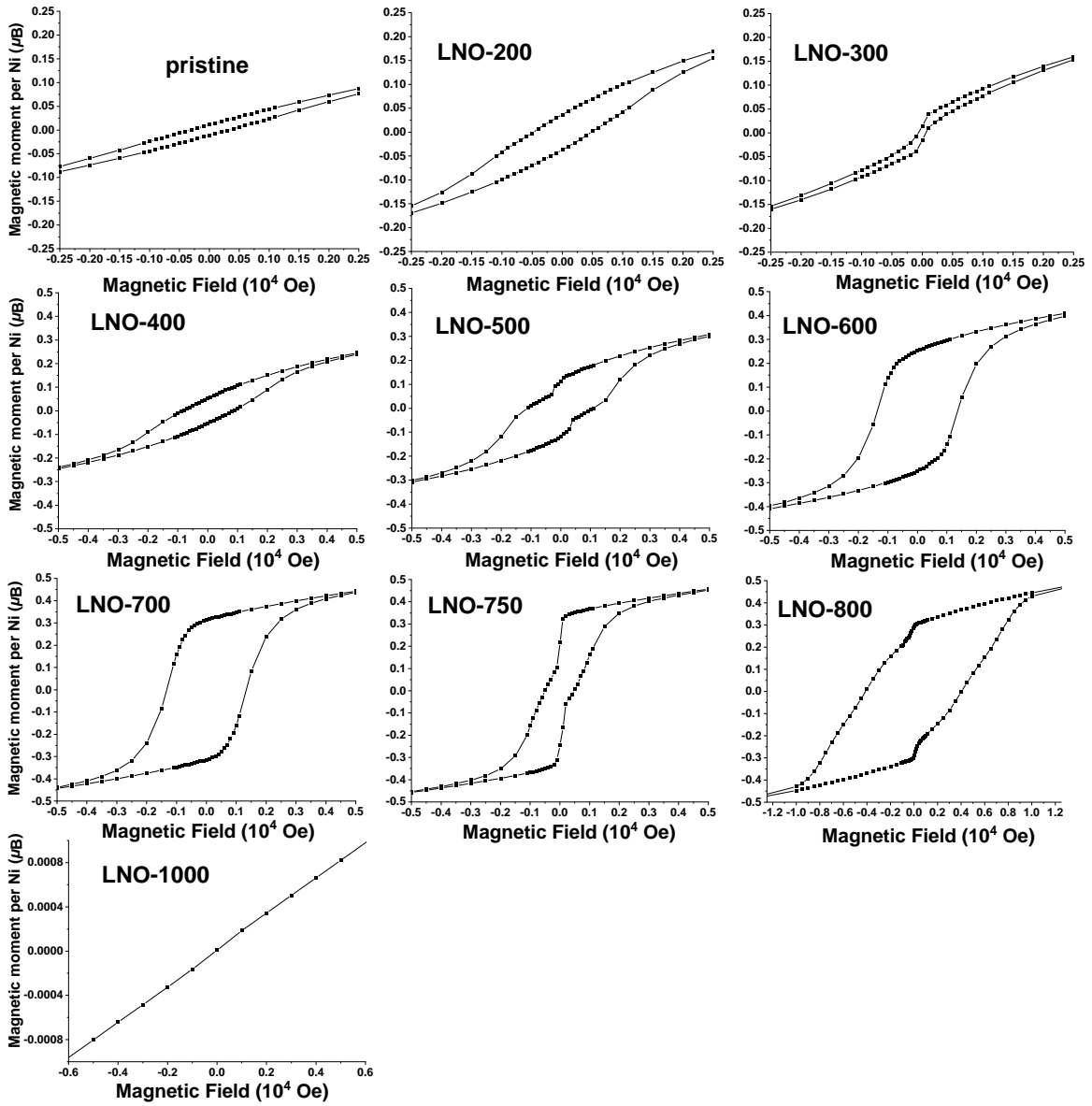


Figure 4.27 Individual field scans at 2 K to illustrate more clearly the evolution of the coercivity fields.

The parameters of interest obtained from these field scans are: (i) the z -component magnetization $M_z(300\text{K})$ measured at $7 \cdot 10^4$ Oe and 300 K (**Figure 4.26d**), (ii) the z -component magnetization $M_z(2\text{K})$ measured at $7 \cdot 10^4$ Oe and 2 K (**Figure 4.26e, f**), and (iii) the coercivity field $CF(2\text{K})$ extracted from the field scans at 2 K (**Figure 4.28**). The higher the temperature of the magnetization measurements the weaker is the influence of magnetic exchange coupling, anisotropies, and other forms of magnetic interactions, i.e. the values of magnetization are closer to those of the free ion case. Therefore, $M_z(300\text{K})$ can be considered to return information

about the magnetic moment per Ni ion in the first place, whereas $M_z(2K)$ more strongly includes effects of interactions of magnetic ions that strongly depend on structural features. $M_z(300K)$ only slightly increases with temperature of heat treatment up to 750 °C (see **Figure 4.26d**) revealing a slightly increasing magnetic moment per Ni on average. For LNO-800, $M_z(300K)$ is considerably larger and decreases drastically again for LNO-1000 since here we have strong antiferromagnetic order present even at 300 K. $M_z(2K)$ is also varying only slightly for temperatures up to 750 °C showing a local minimum for LNO-500 (see **4.26f**). All $M_z(2K)$ values do not exceed $0.8 \mu_B$ per Ni ion and remain well below the expected spin-only saturation z -magnetization of $1 \mu_B$ expected for a free Ni^{2+} ion that would be reached at 2 K and $7 \cdot 10^4$ Oe in the free ion case. This means that some sort of antiferromagnetic sub-lattice coupling and/or anisotropies play a major role here by reducing the observed ordered magnetic moment. $M_z(2K)$ for LNO-1000 is close to zero due to the antiferromagnetic order that is established almost completely at low temperature. The evolution of the coercivity fields $CF(2K)$ as shown in **Figure 4.28** is analogous to that of the evolution of T_B . $CF(2K)$ values up to 300 °C are comparably small and are close to zero for LNO-300. In region (II) the values are increasing first and then decreasing again, very similar to the values of T_B . Again, region (III) (LNO-800) has a characteristic very high value of coercivity. The hysteresis curve of LNO-1000 consisting only of antiferromagnetic NiO does not show any coercivity.

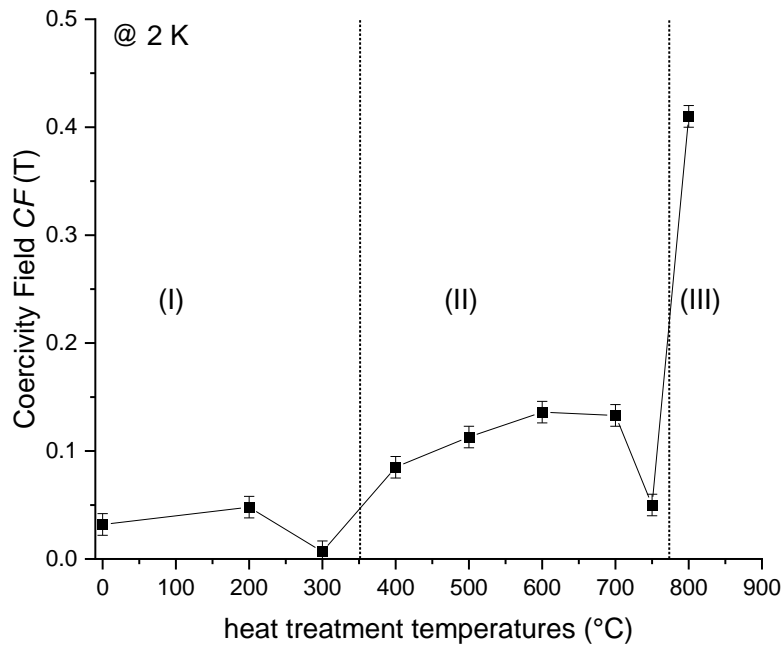


Figure 4.28 The coercivity field $CF(2K)$ extracted from the field scans at 2 K.

The effective paramagnetic moments μ_{eff} in units of Bohr's magneton μ_B and Weiss constant θ were supposed to be extracted from the paramagnetic regions of the high temperature magnetic measurements. Hysteresis measurements at 300 K and 390 K with maximum fields of 5000 Oe and magnetization vs. temperature scans between 270 K and 390 K at 5000 Oe are presented in detail in **Figure 4.29, 4.30**. It should be emphasized that extraction of the paramagnetic parameters, especially the effective paramagnetic moments μ_{eff} in units of Bohr's magneton μ_B is not straight forward for the given series of samples and the obtained values need to be considered very critically. As can clearly be inferred from **Figure 4.31**, only the inverse susceptibility of the pristine sample (and to some extent also those of LNO-200 and LNO-300) exhibits a clear linear region characteristic of the paramagnetic state at higher temperatures. The other curves are bent more or less even up to 390 K, i.e. in addition to the purely paramagnetic behaviour of the majority of Ni ions there is an additional very small contribution from a magnetically ordered phase. As revealed by the high-temperature hysteresis measurements (**Figure 4.29**) several samples exhibit a very small contribution from an additional ferromagnetic phase (deviation from pure linear behaviour around origin) that is equally strong at 300 K and 390 K. The fact that these features are equally strong at these high temperatures points to the existence of a small amount of a reported ferromagnetic monoclinic

NiO phase with $T_c = 808 \text{ K}^{109}$ and a saturation magnetization of about 2.5 Gauss per gram at 300 K^{109} that is supposed to have formed at the surface during the heat treatment (see also TEM results). 5.0(1) wt.% of this ferromagnetic NiO phase can explain the residual magnetization as determined from a linear fit from 2 to $1 \cdot 10^4 \text{ Oe}$ of the field scan at 300 K for LNO-400, for instance, that shows that effect comparably strongly. These features are not ascribed to the ferrimagnetic clusters that are supposed to have formed within the bulk that are also induced by the heat treatment, but that have much lower ordering temperatures as revealed by the evolution of T_B . Even these weak contributions from the a small amount of ferromagnetic NiO phase that have been formed at the surface with an approximately constant magnetization over temperature easily might falsify the determined values of paramagnetic effective moments that are based on a Curie-Weiss behaviour with magnetization proportional to the inverse temperature. The different evolution of the inverse susceptibility curves χ^{-1} in detail obtained at 5000 Oe (**Figure 4.32**) and at $5 \cdot 10^4 \text{ Oe}$ (**Figure 4.26g**), respectively, in the high temperature region below 390 K is very indicative of the presence of some non-paramagnetic contributions to the signal as discussed above. The fact that these contributions play a less pronounced role at higher applied field, since all non-paramagnetic contributions are constantly saturated, motivated us to remeasure this high-temperature region at a higher field of $5 \cdot 10^4 \text{ Oe}$. The linear part (with all the limitations discussed above) from 340 K to 390 K of the susceptibility curves χ^{-1} have been used for a fit by a Curie-Weiss behaviour: $\chi^{-1} = \left(\frac{C}{T-\theta}\right)^{-1}$, with Curie-Weiss constant C , temperature T , Weiss constant θ . From the Curie constant C the effective paramagnetic moments μ_{eff} in units of Bohr's magneton μ_B have been determined and are plotted in **Figure 4.26h** together with the Weiss constant θ . The error bars are not simply determined as a statistical error according to the linear fitting, but include a measure for the uncertainty due to the slight bending of the χ^{-1} curves, i.e. slightly different values could be obtained by changing the temperature region for the linear fitting. Considering these limitations there is no clear trend observable for the evolution of the paramagnetic effective moment μ_{eff} that evolves around approximately $2 \mu_B$ what is the reported value for LiNiO_2 in literature.^{110,111} Since the spin-only paramagnetic moment of Ni^{3+} is $1.73 \mu_B$ some additional contribution to the spin-only moment from orbital momentum contributions for instance are present here. The Weiss constant θ are slightly decreasing in region (I), but are then constantly increasing up to LNO-800 indicating an increasing ferromagnetic mean field coupling.

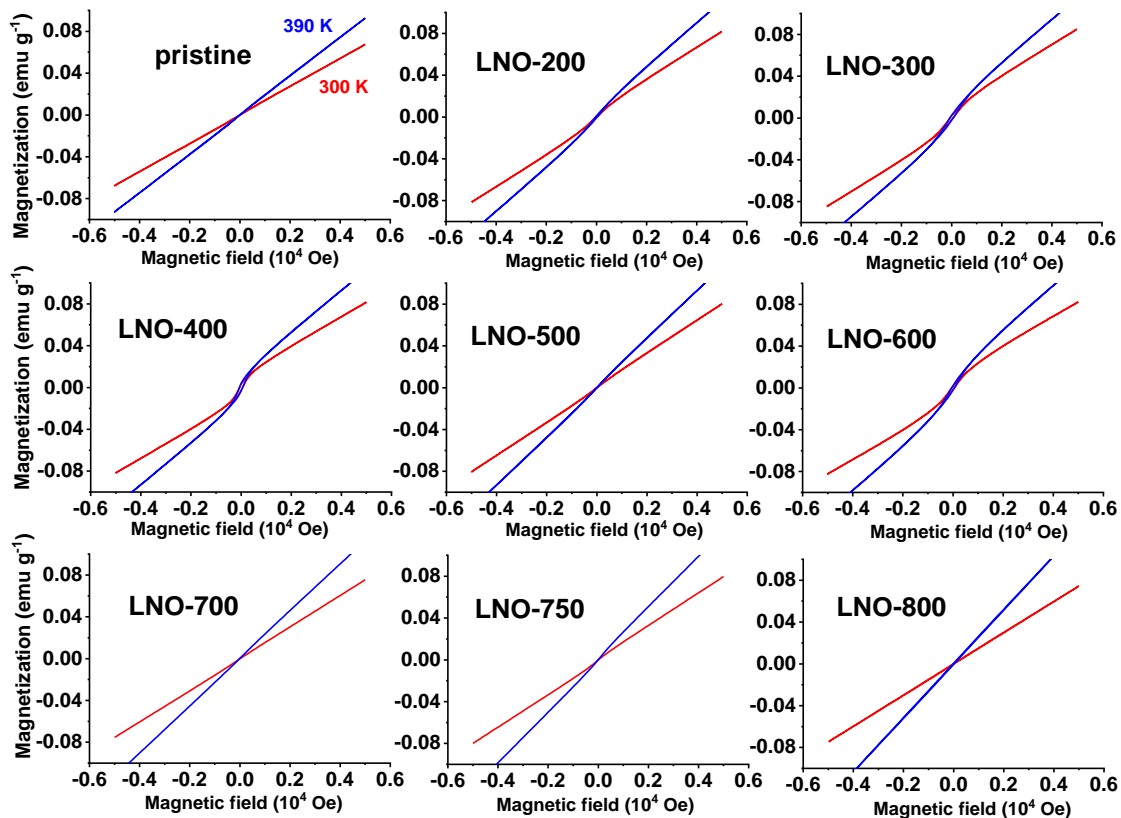


Figure 4.29 Hysteresis measurements at 300 K and 390 K with maximum fields of 5000 Oe.

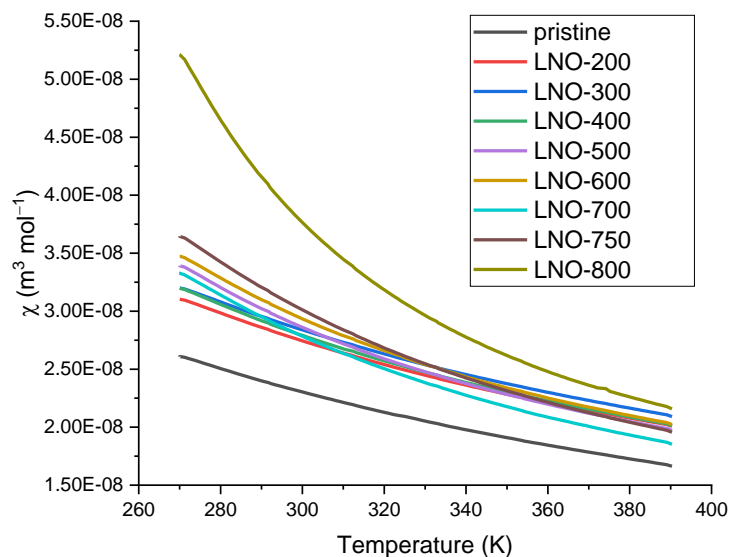


Figure 4.30 Magnetization vs. temperature measurement at high temperature from 270 K to 390 K measured at a field of 5000 Oe.

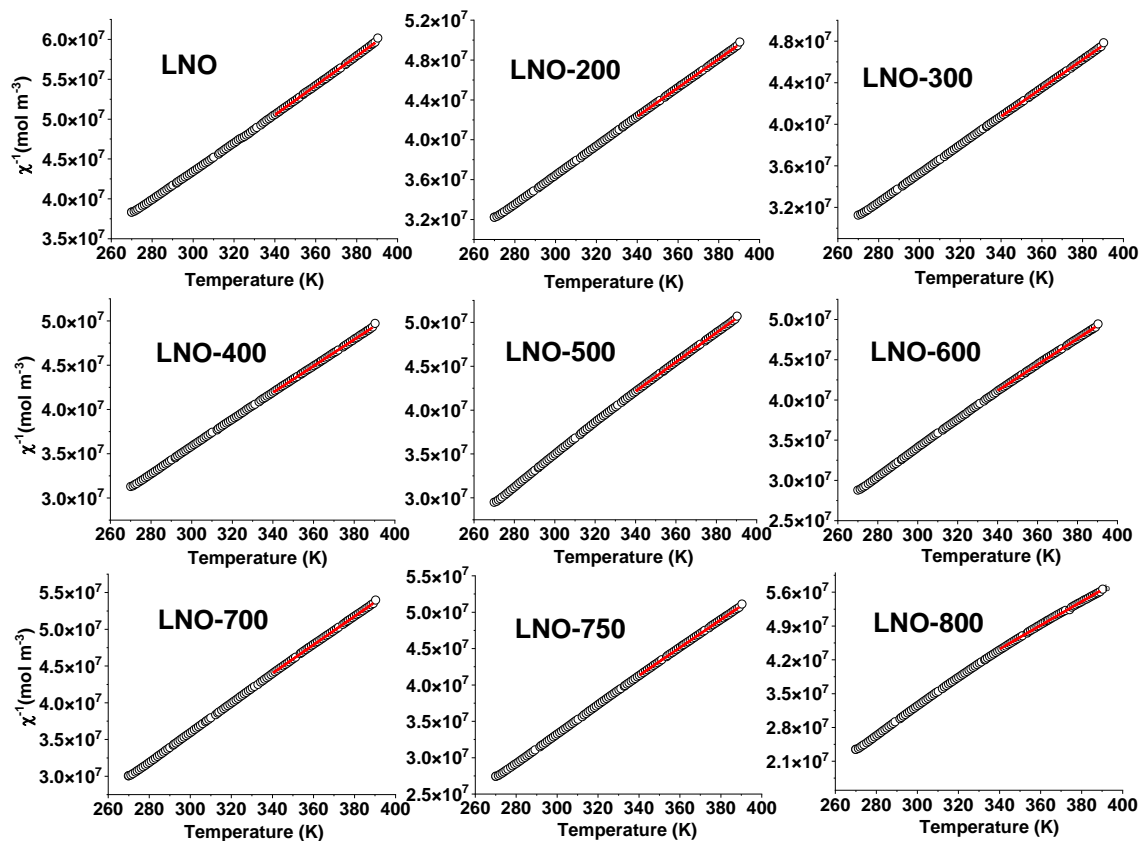


Figure 4.31 Curie-Weiss fits to the 340 K to 390 K temperature region of the inverse susceptibility χ^{-1} .

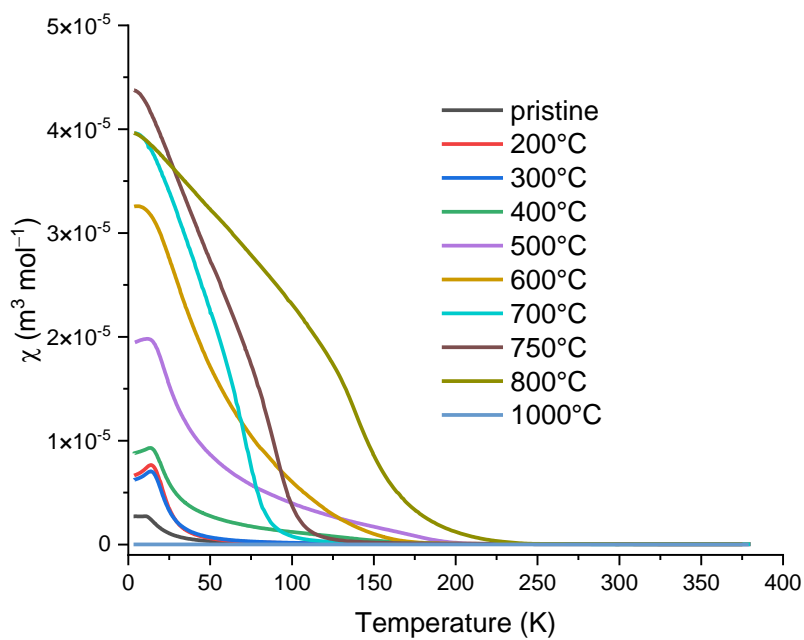


Figure 4.32 The inverse susceptibility curves χ^{-1} obtained at 5000 Oe.

Overall the observed evolution of magnetic properties can be correlated as follows with structural changes as induced by the heat treatment: Up to 300°C (region (I)) there are only minor effects on the magnetic properties. All determined values only change slightly compared to those of the ‘pristine’ state. A slight increase of $M_z(300K)$ and μ_{eff} indicates a somewhat increasing magnetic moment that could be explained by a corresponding reduction of some Ni^{3+} to Ni^{2+} as also revealed by XAS and corresponds well with the slow reaction kinetics between LNO and CO_2 as outlined above. In region (II) with heat treatments from 400 °C to 750 °C the magnetic properties change more drastically: $M_z(300K)$, as the most trustful parameter for average magnetization value per Ni ion, does still exhibit only a very slight increase with heat treatment temperature that is in agreement with the results from XAS measurements. Whereas the average magnetic moment of the Ni ions only slightly increases in region (II), many other parameters extracted from the magnetic measurements that are related to the magnetic coupling of the Ni ions and therefore are connected to the spatial distribution of the Ni ions within the layered structure change significantly. The ferromagnetic mean-field coupling parametrized by Weiss constant θ is monotonically increasing with thermal treatment temperature. This is in agreement with the observation that more and more Ni ions are located on a Li site as inferred from the XRD measurements. It is supposed that the increasing but small number of Ni^{2+} ions are located in the Li layer (ionic radii of Ni^{2+} and Li^+ are very similar). Whereas the Ni ions in the Ni layer exhibit a ferromagnetic intralayer coupling, there is only a very weak and somewhat frustrated coupling between these Ni-layers. However, as soon as Ni^{2+} enters the Li layer these Ni^{2+} couple antiferromagnetically with the Ni^{2+} in the neighboring Ni-layers resulting in ferrimagnetically ordered clusters and effective ferromagnetic mean-field coupling as parametrized by the Weiss constant θ . As a consequence, also the temperature where a magnetic ordering sets in shifts to higher temperatures as confirmed by the evolution of T_B . The coercivity field at 2 K $CF(2K)$ also increases concomitant with T_B which might be related to an increasing number of lattice defects that hinder more effectively the ferrimagnetic domain wall movement. However, T_B and $CF(2K)$ are significantly reduced again for LNO-750, i.e. in detail there seems to exist some concurring and partially opposing effects leading to local maxima/minima in the evolution of the parameters. This is supposed to be connected with the point when more and more Ni^{2+} ions are finally also incorporated into the Ni-layer: around 700 °C decomposition of LNO within the bulk occurs and a large part of Ni^{2+} ions remains in the Ni-layer rather than to occupy Li vacancies in the Li-Layer (small value of z in $\text{Li}_{1-z}\text{Ni}_{1+z}\text{O}_2$ in XRD compared with that of 600 °C, but large amount of reduced Ni^{2+} in Ni layers suggested from NMR and XAS). The highest observed value for the coercivity field $CF(2K)$ for LNO-800 can be explained by

a pronounced hindering of magnetic domain wall movement due to the multi-phase nature of this sample consisting of LNO and (Li,Ni)O phase. LNO-1000 on the other side has dramatically changed by losing a lot of oxygen and a transformation from LNO to the $\text{Li}_y\text{Ni}_{1-y}\text{O}$ phase that orders antiferromagnetically and exhibits a totally different magnetic behaviour compared with the temperature-treated LNO sample series.

4.3.7 TEM

High-resolution STEM was performed to get more insights into local changes of the crystal structure. For pristine LNO, small particles (several hundred nm) were used and the layered structure can be clearly identified by the electron diffraction (**Figure 4.33a**) and high-resolution high-angle annular dark-field (HAADF) imaging (**Figure 4.33b**). The d spacing of 4.73 Å corresponds to the (003) atomic plane in the rhombohedral phase. Based on the EELS spectrum imaging data and more exactly on the Ni L3-edge chemical shift mapping, Ni reduction already happens on the LNO particle surface, proving the existence of off-stoichiometric $\text{Li}_{1-z}\text{Ni}_{1+z}\text{O}_2$ phase (**Figure 4.34**). This is shown by the Ni L3 edge 1 eV shift towards lower energies (855 eV for bulk and 854 eV for surface) and also by the diminishing of the O K-edge pre-peak in the surface regions (**Figure 4.34c**). After the heat treatment at 200 °C, the image contrast on the particle surface has changed both in parallel (**Figure 4.33c**) and normal (**Figure 4.33d**) to (003) direction. In the HAADF regime, the contrast is proportional to the atomic number ($\sim Z^{1.7}$).¹¹² When Ni^{2+} migrates to Li sites, the increasing of Z leads to an increased contrast in the regions marked by yellow boxes. The slightly stronger off-stoichiometric $\text{Li}_{1-z}\text{Ni}_{1+z}\text{O}_2$ phase is formed through the reaction between LNO and CO_2 (Eqn. (4.3)).

When the heat-treatment temperature is 400 °C, an obviously thicker $\text{Li}_{1-z}\text{Ni}_{1+z}\text{O}_2$ phase was observed along the particle surface in **Figure 4.33e**. In some regions the cubic structure could be recognized (such as the one in **Figure 4.33f**) in HAADF images, which is in accordance with the ferromagnetic NiO phase in the magnetic measurement. This cubic phase is formed from the $\text{Li}_{1-z}\text{Ni}_{1+z}\text{O}_2$ phase with extremely strong off-stoichiometry. The off-stoichiometry in the bulk (observed by XRD) and at the surface (observed by TEM) before 700 °C are both induced by the reaction between LNO and CO_2 (Eqn. (4.3)). At the surface the reaction proceeds to a larger extent because of the direct contact between LNO and CO_2 . In the bulk the reaction also occurs possibly by the migration of Li from the bulk to the Li vacancies at the surface, otherwise the off-stoichiometry would not be observed by XRD. An inhomogeneous distribution of z in $\text{Li}_{1-z}\text{Ni}_{1+z}\text{O}_2$ could therefore exist, but not confirmed neither by XRD nor TEM images.

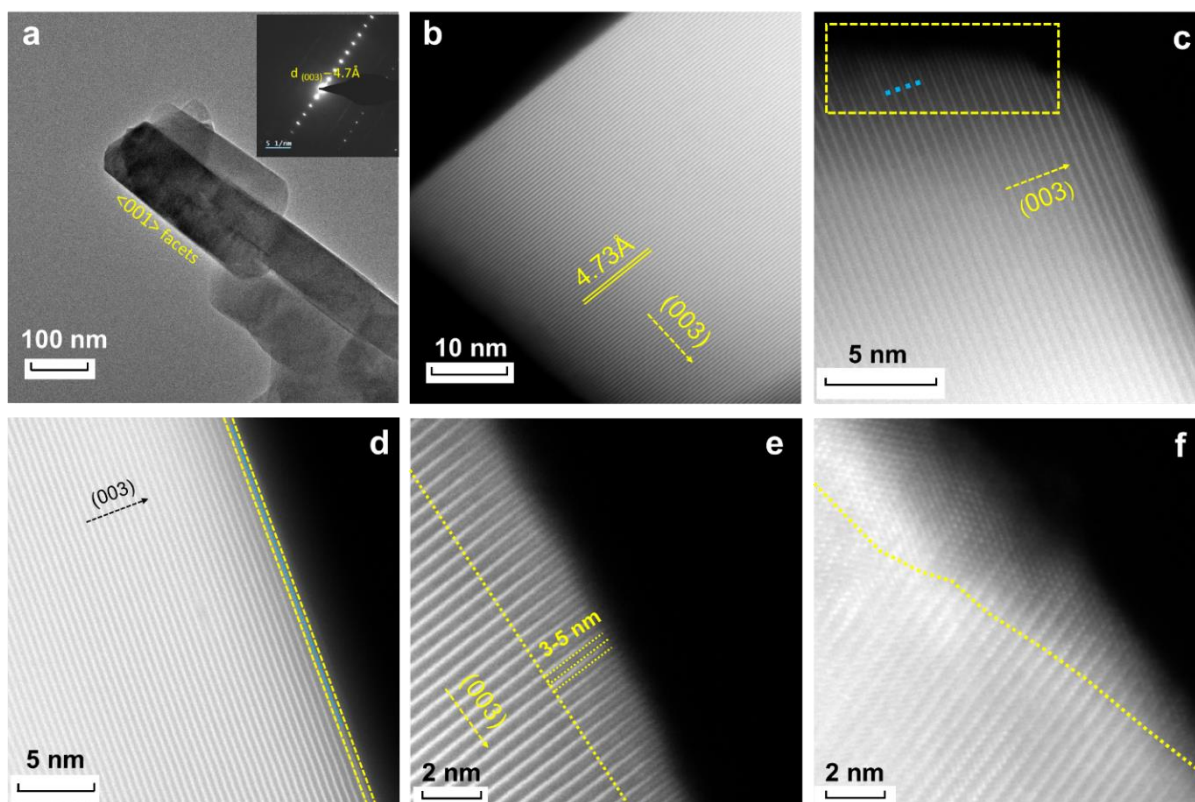


Figure 4.33 (a) low-magnification TEM image of LNO particles with the corresponding electron diffraction pattern shown as the inset; (b) high-magnification TEM image of LNO with interplanar spacing of (003) being labelled; HAADF image of LNO-200 with the strongly off-stoichiometric $\text{Li}_{1-z}\text{Ni}_{1+z}\text{O}_2$ region (c) parallel and (d) normal to (003) direction marked by the yellow boxes; The blue dots denote the Ni^{2+} migrating to Li sites with increased intensity on Li column. HAADF image of LNO-400 with (e) the strongly off-stoichiometric $\text{Li}_{1-x}\text{Ni}_{1+x}\text{O}_2$ region and (f) thin cubic phase on particle surface.

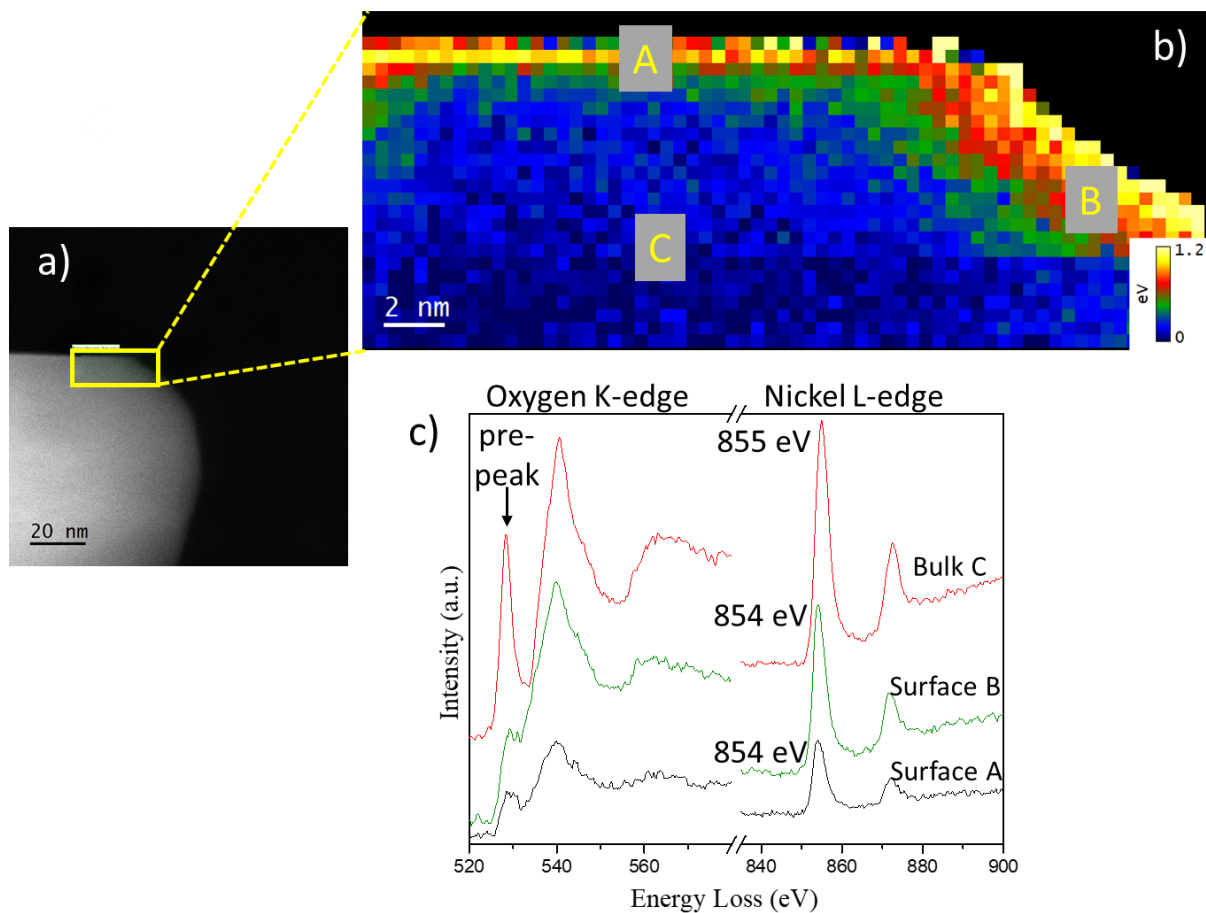


Figure 4. 34 (a) STEM image of an LNO particle, (b) Ni L-edge chemical shift mapping of the yellow area in (a) and (c) corresponding EELS spectra from different locations revealing a reduced oxidation state of Ni at the surface.

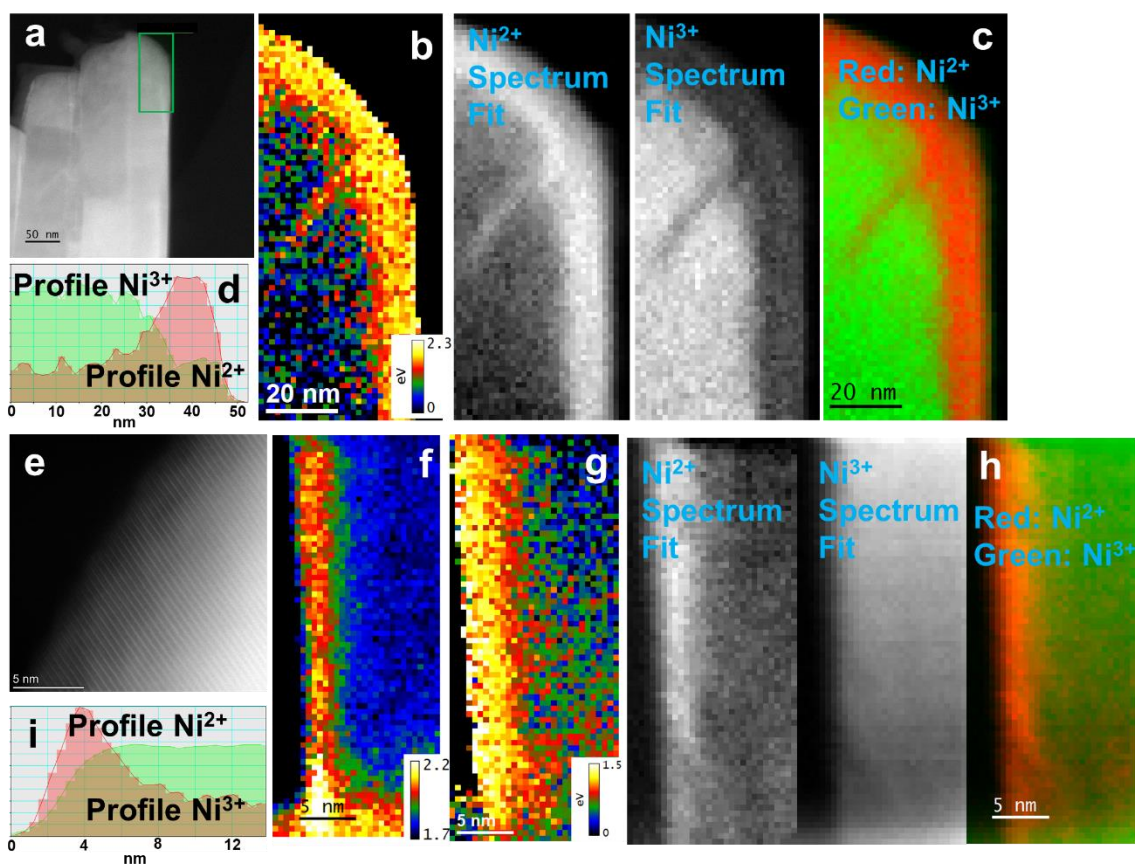


Figure 4.35 (a) low-magnification TEM image of LNO-400, (b) the corresponding EEL spectra-based Ni L-edge chemical shift, (c) Ni oxidation state mapping marked with the green rectangle in (a) and (d) the profile of the bulk and surface fitting, revealing the concentration of $\text{Ni}^{2+}/\text{Ni}^{3+}$. EEL spectra-based analyses on LNO-700: (e) High-magnification TEM image, (f) Ni M-edge/Li K-edge ratio mapping, (g) Ni L-edge chemical shift mapping and (h) the mapping of $\text{Ni}^{2+}/\text{Ni}^{3+}$ distribution. (i) shows the relative concentration of $\text{Ni}^{2+}/\text{Ni}^{3+}$.

To further investigate the structural change in LNO-400, electron energy loss spectroscopy spectrum imaging mapping (EELS-SI) was performed (**Figure 4.35**). Corresponding spectra of O K-edge and Ni L-edge at the surface and in the bulk are provided in **Figure 4.36**. The Ni L-edge chemical shift map of the selected green region (**Figure 4.35a**) is shown in **Figure 4.35b**. The yellow region at the surface shows that a large amount of Ni ions has an oxidation state lower than 3+. This area is larger than that in the HAADF image, since only higher occupancy of Ni on lithium sites could induce obvious contrast change in STEM. The yellow-coded region (thickness of 10-12 nm) covers a wider range of off-stoichiometry in $\text{Li}_{1-z}\text{Ni}_{1+z}\text{O}_2$ or NiO phase. As discussed in the NMR part, the gradual Ni reduction corresponds to the increase of z in Li_{1-}

$z\text{Ni}_{1+z}\text{O}_2$ before thermal treatment at 700 °C. The inhomogeneous distribution of Li could therefore also be reflected in **Figure 4.35b**. **Figure 4.35c** shows the Ni oxidation state mapping based on the multiple linear least squares (MLLS) fitting of the 520-950 eV spectral region, including both O K-edge and Ni white lines. The thickness of the reduced Ni layer increases to about 15 nm, since a wider range of off-stoichiometry in $\text{Li}_{1-z}\text{Ni}_{1+z}\text{O}_2$ phase is revealed by this method. The pure red colour at the surface corresponds to the ferromagnetic NiO phase found in the magnetic measurements. The profile of the bulk and surface fitting is shown in **Figure 4.35d**, revealing the proportion of Ni^{2+} and Ni^{3+} in the two regions approximately. Small amounts of Ni^{2+} ions still exist in the bulk, in accordance with the off-stoichiometry of LNO observed by XRD.

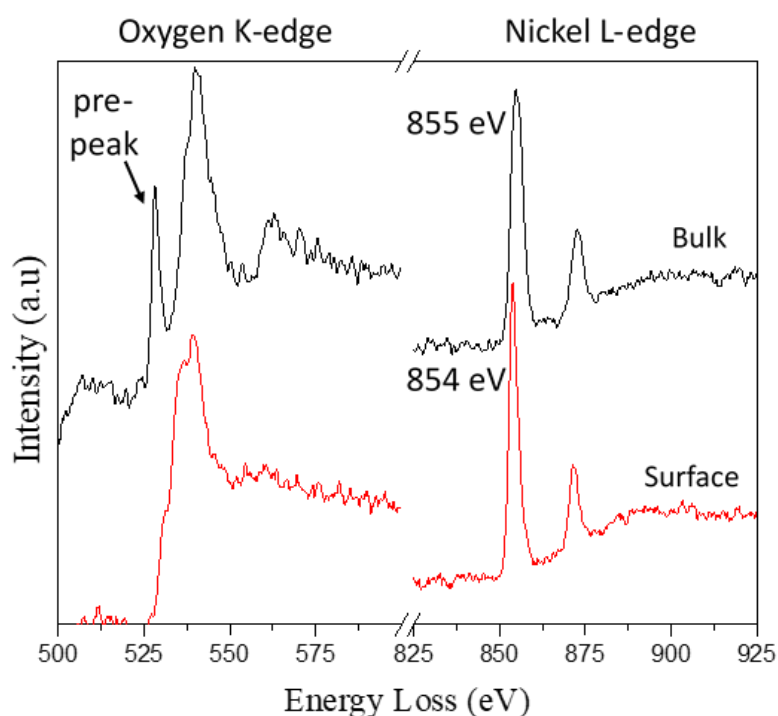


Figure 4.36 Corresponding spectra of O K-edge and Ni L-edge on surface and bulk from the green area in **Figure 4.35a**.

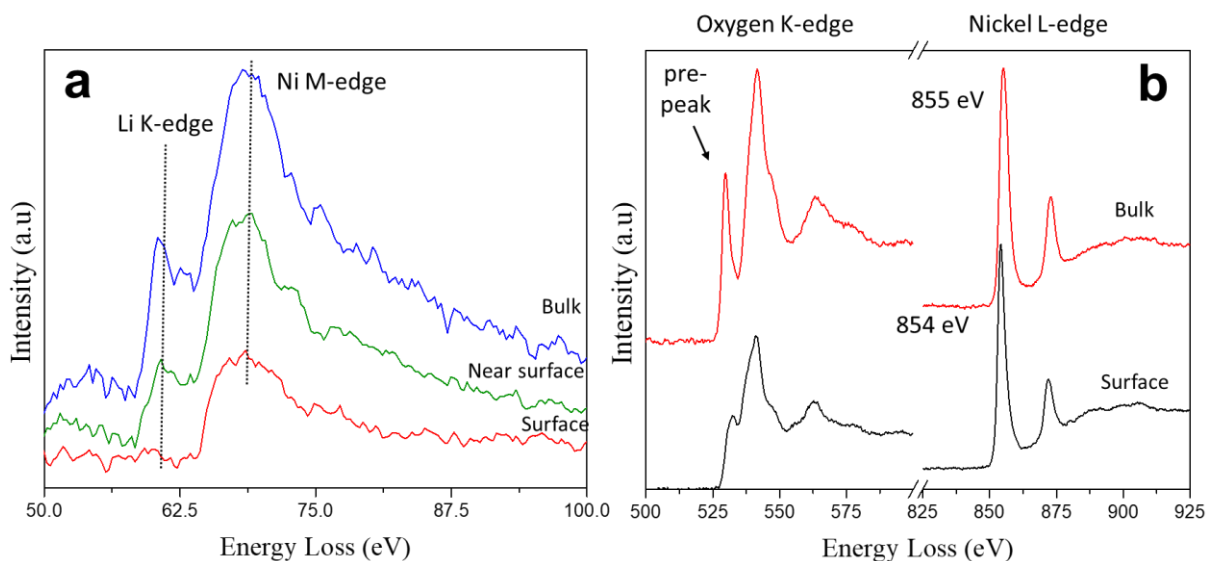


Figure 4.37 Corresponding to the spectra of O K-edge and Ni M/L-edge on surface and bulk as shown in **Figure 4.35f, g**.

Figure 4.35e shows the HAADF image of the LNO-700. To clearly investigate the structural change in this sample, EELS-SI was also performed with Li K-edge, Ni M/L-edge spectra are shown in **Figure 4.37**. Ni M-edge/Li K-edge map was firstly plotted to evaluate the Li loss situation at the particle surface in **Figure 4.35f**. There is a Li-poor region at the surface with a thickness of 3-4 nm and a thin transitional area (dark green area) with medium concentration of Li. As discussed in the XRD part, the decomposition of LNO happens at 700 °C but at slow rate and inhomogeneously. The Li-poor region corresponds to the area with the strongest off-stoichiometry discussed in the XRD part. A large amount of Li ions has been lost and the vacancies are occupied by Ni ions. A small extent of Li/Ni mixing (Li also migrates to Ni layers) could happen in this area, but no evidence was found to prove this. The neighboring Li transitional area represents the weaker off-stoichiometry in $\text{Li}_{1-z}\text{Ni}_{1+z}\text{O}_2$ and also the intermediate states of different decomposition extents between bulk and surface. The information about the Ni oxidation state could be acquired from **Figure 4.35g**, the Ni L-edge chemical shift map of the same area. When compared with the thickness of regions with reduced Ni for LNO-400, it is even getting thinner at 700 °C. As discussed in the XRD part, Eqns. (4.1) and (4.3) described competitive reactions. The reaction of Eqn. (4.3) is therefore suppressed and that of Eqn. (4.1) proceeds at a sluggish rate. The actual extent of Ni reduction at the surface of LNO-700 is, therefore, smaller than that of LNO-400. **Figure 4.35h** shows the Ni oxidation state mapping based on the MLLS fitting of the O K-edge. The corresponding intensity profile

is provided in **Figure 4.35i**. Results similar to those of **Figure 4.35f** could be obtained. There is a maximum concentration of Ni^{2+} at the surface, corresponding to the Li poor and Li transitional regions in **Figure 4.35e**. Although not obvious in **Figure 4.35g**, a certain concentration of Ni^{2+} still exists behind the maximum and decreases slowly into the bulk. This portion of Ni^{2+} corresponds to the ones located at Li sites and Ni sites, induced by the bulk decomposition of LNO. In summary, TEM analysis mainly reveals the reactions at the surface, but that does not mean reactions according to Eqns. (4.1) and (4.3) happen exclusively in surface regions. The off-stoichiometry in $\text{Li}_{1-z}\text{Ni}_{1+z}\text{O}_2$ exists both in the bulk and at the surface, but with different degrees. Extremely large z in $\text{Li}_{1-z}\text{Ni}_{1+z}\text{O}_2$ or phase transitions to the cubic phase happen earlier at the surface, but in a limited and ultra-small area.

4.4 Conclusion

Pristine LiNiO₂ experiences several reaction regions under post-synthesis thermal treatment in air at various temperatures. Firstly, in region I from the pristine state to 300 °C, LiNiO₂ reacts with CO₂ at an extremely low rate, forming a weakly off-stoichiometric Li_{1-z}Ni_{1+z}O₂ phase. In the second region (400 to 750 °C), the rate of the reaction gradually increases, and also the *z* value in Li_{1-z}Ni_{1+z}O₂ increases until 600 °C. As one product, more and more Li₂CO₃ is observed by XRD. At 700 °C, LiNiO₂ decomposition occurs at a sluggish rate, and the reaction between LiNiO₂ and CO₂ is suppressed. The decomposition corresponds to the increasing rate of Ni reduction and a larger content of reduced Ni²⁺ staying in the Ni layers rather than being replaced to the Li vacancies. At 750 °C, cubic Li_{1-y}Ni_yO is first detected by XRD. In the third region (800-1000 °C), the cubic phase quickly dominates the material and the phase transition is accompanied by huge oxygen and lithium loss. The extent of both reactions may not be homogeneous through the material and a larger extent is found in the surface region. An ultrathin layer of ferromagnetic cubic phase therefore appears below 750 °C, verified by magnetic and TEM measurements. When the off-stoichiometry of Li_{1-z}Ni_{1+z}O₂ is not strong (namely for heat treatments between 200-400 °C), the electrochemical performance of LiNiO₂ could be improved with respect to the cycling stability. **Table 4.5** summarizes the representative relevant information of thermally treated samples. We believe the post-synthesis thermal treatment could be an easy method to obtain better performance of LiNiO₂ and also for other Ni-based cathodes.

Table 4.6 Summary of relevant information of thermally treated samples. The decrease of edge position in XPS corresponds to the continuous reduction of Ni. The temperature T_B in PPMS indicates the number of Ni^{2+} ions located in the Li layers, corresponding to the value in the fourth column, i.e. the value of Ni located in the Li layers obtained by Rietveld refinement. The last column shows the values of capacity retention when cells containing corresponding materials as cathodes were cycled between 2.5-4.5 V at 0.1 C.

Name	Heat treatment 12 h in air	Phase composition	Ni located in the Li layers	weight of Li_2CO_3 (%)	Edge position in XPS (eV)	T_B (K) in PPMS	Capacity retention after 50 cycles
pristine		$R\bar{3}m$	$2.9 \pm 0.2\%$	0	8344.66	7.35	60.8%
LNO-200	200°C	$R\bar{3}m$	$4.1 \pm 0.2\%$	0	8344.71	9.23	64.7%
LNO-300	300°C	$R\bar{3}m$	$4.0 \pm 0.2\%$	0	8344.61	12.76	63.0%
LNO-400	400°C	$R\bar{3}m$	$4.9 \pm 0.3\%$	3.0%	8344.53	82.9	97.6%
LNO-500	500°C	$R\bar{3}m$	$7.5 \pm 0.3\%$	4.8%	8344.54	135.7	
LNO-600	600°C	$R\bar{3}m$	$10.4 \pm 0.3\%$	6.1%	8344.51	138.8	
LNO-700	700°C	$R\bar{3}m$	$9.3 \pm 0.2\%$	5.3%	8344.21	72.6	
LNO-750	750°C	99% $R\bar{3}m$ 1% $Fm\bar{3}m$	$11.5 \pm 0.2\%$	4.1%	8344.09	91.4	
LNO-800	800°C	85% $R\bar{3}m$ 15% $Fm\bar{3}m$	$19.2 \pm 0.2\%$	0	8343.69	223	
LNO-850	850°C	21% $R\bar{3}m$ 79% $Fm\bar{3}m$		0	8342.71		
LNO-1000	1000°C	$Fm\bar{3}m$		0	8342.06		

Chapter 5 Conclusion and outlook

In the present thesis, I mainly focus on the new insights into structural changes of LiNiO_2 . Much of our understanding of the structure evolution of LiNiO_2 comes from classic but well-established techniques. With the continuous improvements in characterization methods, new studies of subtle structural changes, particularly the Li/vacancy ordering and thermal stabilities at low temperatures, can be conducted. This knowledge is essential for the understanding of stable delithiated Li_xNiO_2 phases and the adjustment of electrochemical performance. As today's Li-ion battery research is pushing to cathodes with extremely higher Ni content, the revisit of LiNiO_2 is of vital importance and also fits to the interests from both industry and academia.

Regarding the first part, *ex situ* ^6Li and *in situ* ^7Li NMR spectroscopy is applied to monitor lithium mobility in LiNiO_2 during Li-ion (de)intercalation. Experimental NMR shifts are compared with the calculated shifts, which are based on the theoretical Li/vacancy ordering models. The observed shifts are in good agreement with estimated values. Two phenomena are most interesting and obvious. A considerable line broadening is first observed at SoC 20%. The rate of Li hopping decreases just before the ordering structure $\text{Li}_{0.75}\text{NiO}_2$ appears. This first Li/vacancy ordering structure can strengthen the Jahn-Teller effect, thus distorting the layered structure and decreasing the Li hopping rate. For the last three SoC states (75%, 80% and 85%), the NMR peak positions remain at higher ppm positions. This suggests that the remaining Ni^{3+} is located preferentially in the vicinity of the remaining Li ions, fitting well with the calculation model $\text{Li}_{0.25}\text{NiO}_2$: each Li ion is surrounded by six Ni^{3+} with the $180^\circ \text{Li}_A\text{-O-TM-O-Li}_B$ configuration. Such a special Li-ordered and $\text{Ni}^{3+}/\text{Ni}^{4+}$ -ordered structure corresponds to the single H2 phase and appears to be the necessary preparation step for H2-H3 phase transition. GITT and XAS measurements were also conducted to monitor changes of Li mobility and oxidation state of Ni.

Based on the understanding of Li/vacancy ordering structures of LiNiO_2 , further studies on the Li hopping in doped LiNiO_2 can be conducted. The Li/vacancy ordering can be disrupted by the dopants in the Li layers, causing a solid-solution de(inter)calation mechanism rather than multiple two-phase reactions. This behavior will be understood from the perspective of "quasi" Li-ordered structures. For example, $\text{Li}_{0.25}\text{NiO}_2$ ordered structure determines the nature of the single H2 phase for LiNiO_2 . For doped LiNiO_2 , the system still tries to install the characteristic sequence of Li ordering distribution, however some sites are occupied by dopants and a "quasi"

ordered structure would form instead. The dopants would partly disrupt the ordering and narrow the miscibility gap between H2 and H3, thereby mitigating or eliminating the phase transitions. In summary, building the connection between phase transitions and Li-ordered structures is essential to the exploration of the minimum dopant content required to stabilize the Ni-rich cathode, i.e. understanding the trade-off between capacity and stability.

Regarding the second part, LiNiO₂ is investigated with respect to the subtle structural and electronic changes induced by a thermal treatment in air after synthesis in pure oxygen. These structural evolutions can also be regarded as the reflection of thermal instabilities of LiNiO₂ at low temperatures. Combination of thermogravimetry, synchrotron XRD/XAS, ⁷Li MAS NMR spectroscopy, magnetic measurements, and TEM is applied to identify such subtle changes. These measurements reveal that Ni migration to the Li layer already starts at 200°C, later followed by reactions with CO₂. With the heat treatment temperature increasing, strong off-stoichiometric Li_{1-z}Ni_{1+z}O₂ phases and Li₂CO₃ have been obtained. At 700°C, bulk decomposition occurs at a sluggish rate, suppressing the reactions with CO₂. The decomposition corresponds to the increasing rate of Ni reduction and preference of Ni²⁺ for occupying the Ni sites. The extent of both reactions may not be homogeneous through the material, a larger reaction rate is instead found at the surface. In addition, mild thermal treatment at 360-380°C can improve the electrochemical performance of LiNiO₂ since a ferromagnetic cubic phase in the surface region can serve as a protection layer.

We believe the insight provided here is the first step towards possible understanding of the post-synthesis treatment. When targeting compounds with Ni content larger than 95%, similar mechanism behind treatment as that of LiNiO₂ can be expected. This work can thus provide useful guidance for further studies on surface modification of Ni-rich cathode materials. The presence of a cubic phase at surface may serve as the protection layer, improving the structural stability profoundly. A disordered rock salt phase may be formed after treatment when specific dopants are introduced into the LiNiO₂ structure. Such compounds are structurally related to LiNiO₂ and are reported to effectively conduct lithium. Noticeable achievements have shown that such compounds can provide stabilization without sacrificing large amount of energy density. Combination of the two fields, i.e. post-synthesis treatment and disordered rock salts phase, can be a promising topic for future research. I believe that ultimate Ni-rich cathode material can finally be commercialized by trying new strategies continuously.

Reference

1. Ryu, H. H.; Sun, H. H.; Myung, S. T.; Yoon, C. S.; Sun, Y. K. Reducing Cobalt from Lithium-Ion Batteries for the Electric Vehicle Era. *Energy Environ. Sci.* **2021**, *14* (2), 844–852.
2. Kim, J.; Lee, H.; Cha, H.; Yoon, M.; Park, M.; Cho, J. Prospect and Reality of Ni-Rich Cathode for Commercialization. *Adv. Energy Mater.* **2018**, *8* (6), 1702028.
3. Liu, W.; Oh, P.; Liu, X.; Lee, M. J.; Cho, W.; Chae, S.; Kim, Y.; Cho, J. Nickel-Rich Layered Lithium Transition-Metal Oxide for High-Energy Lithium-Ion Batteries. *Angew. Chemie Int. Ed.* **2015**, *54* (15), 4440–4457.
4. Li, W.; Erickson, E. M.; Manthiram, A. High-Nickel Layered Oxide Cathodes for Lithium-Based Automotive Batteries. *Nat. Energy* **2020**, *5* (1), 26–34.
5. Muralidharan, N.; Self, E. C.; Dixit, M.; Du, Z.; Essehli, R.; Amin, R.; Nanda, J.; Belharouak, I.; Muralidharan, N.; Dixit, M.; Du, Z.; Essehli, R.; Amin, R.; Belharouak, I.; Self, E. C.; Nanda, J. Next-Generation Cobalt-Free Cathodes – A Prospective Solution to the Battery Industry’s Cobalt Problem. *Adv. Energy Mater.* **2022**, *12* (9), 2103050.
6. Ben-Kamel, K.; Amdouni, N.; Groult, H.; Mauger, A.; Zaghbi, K.; Julien, C. M. Structural and Electrochemical Properties of LiMoO₂. *J. Power Sources* **2012**, *202*, 314–321.
7. Xu, J.; Lin, F.; Doeff, M. M.; Tong, W. A Review of Ni-Based Layered Oxides for Rechargeable Li-Ion Batteries. *J. Mater. Chem. A* **2017**, *5* (3), 874–901.
8. De Biasi, L.; Kondrakov, A. O.; Geßwein, H.; Brezesinski, T.; Hartmann, P.; Janek, J. Between Scylla and Charybdis: Balancing among Structural Stability and Energy Density of Layered NCM Cathode Materials for Advanced Lithium-Ion Batteries. *J. Phys. Chem. C* **2017**, *121* (47), 26163–26171.
9. Li, W.; Song, B.; Manthiram, A. High-Voltage Positive Electrode Materials for Lithium-Ion Batteries. *Chem. Soc. Rev.* **2017**, *46* (10), 3006–3059.
10. Peljo, P.; Girault, H. H. Electrochemical Potential Window of Battery Electrolytes: The HOMO-LUMO Misconception. *Energy Environ. Sci.* **2018**, *11* (9), 2306–2309.
11. Bazant, M. Z. Theory of Chemical Kinetics and Charge Transfer Based on Nonequilibrium Thermodynamics. *Acc. Chem. Res.* **2013**, *46* (5), 1144–1160.
12. Dreyer, W.; Jamnik, J.; Guhlke, C.; Huth, R.; Moškon, J.; Gaberšček, M. The Thermodynamic Origin of Hysteresis in Insertion Batteries. *Nat. Mater.* **2010**, *9* (5), 448–453.
13. Dyer, L. D.; Borie, B. S.; Smith, G. P. Alkali Metal-Nickel Oxides of the Type MNiO₂. *J. Am. Chem. Soc.* **1954**, *76* (6), 1499–1503.
14. Xu, C.; Reeves, P. J.; Jacquet, Q.; Grey, C. P.; Xu, C.; Reeves, P. J.; Jacquet, Q.; Grey, C. P. Phase Behavior during Electrochemical Cycling of Ni-Rich Cathode Materials for Li-Ion Batteries. *Adv. Energy Mater.* **2021**, *11* (7), 2003404.
15. Claude, D.; Peres, J. P.; Rougier, A.; Demourgues, A.; Weill, F.; Chadwick, A.;

- Broussely, M.; Perton, F.; Biensan, P.; Willmann, P. On the Behavior of the Li_xNiO_2 System: An Electrochemical and Structural Overview. *J. Power Sources* **1997**, *68* (1), 120–125.
16. Koyama, Y.; Arai, H.; Tanaka, I.; Uchimoto, Y.; Ogumi, Z. Defect Chemistry in Layered LiMO_2 (M = Co, Ni, Mn, and $\text{Li}_{1/3}\text{Mn}_{2/3}$) by First-Principles Calculations. *Chem. Mater.* **2012**, *24* (20), 3886–3894.
 17. Pouillier, C.; Suard, E.; Delmas, C. Structural Characterization of $\text{Li}_{1-z}\text{Ni}_{1+z}\text{O}_2$ by Neutron Diffraction. *J. Solid State Chem.* **2001**, *158* (2), 187–197.
 18. Rossen, E.; Jones, C. D. W.; Dahn, J. R. Structure and Electrochemistry of $\text{Li}_x\text{Mn}_y\text{Ni}_{1-y}\text{O}_2$. *Solid State Ionics* **1992**, *57* (3–4), 311–318.
 19. Rougier, A.; Delmas, C.; Chouteau, G. Magnetism of $\text{Li}_{1-z}\text{Ni}_{1+z}\text{O}_2$: A Powerful Tool for Structure Determination. *J. Phys. Chem. Solids* **1996**, *57* (6–8), 1101–1103.
 20. Yamaura, K.; Takano, M.; Hirano, A.; Kanno, R. Magnetic Properties of $\text{Li}_{1-x}\text{Ni}_{1+x}\text{O}_2$ ($0 \leq x \leq 0.08$). *J. Solid State Chem.* **1996**, *127* (1), 109–118.
 21. Anderson, P. W. Resonating Valence Bonds: A New Kind of Insulator? *Mater. Res. Bull.* **1973**, *8* (2), 153–160.
 22. Rougier, A.; Gravereau, P.; Delmas, C. Optimization of the Composition of the $\text{Li}_{1-z}\text{Ni}_{1+z}\text{O}_2$ Electrode Materials: Structural, Magnetic, and Electrochemical Studies. *J. Electrochem. Soc.* **1996**, *143* (4), 1168–1175.
 23. Levi, E.; Levi, M. D.; Salitra, G.; Aurbach, D.; Oesten, R.; Heider, U.; Heider, L. Electrochemical and In-Situ XRD Characterization of LiNiO_2 and $\text{LiCo}_{0.2}\text{Ni}_{0.8}\text{O}_2$ Electrodes for Rechargeable Lithium Cells. *Solid State Ionics* **1999**, *126* (1–2), 97–108.
 24. Yang, X. Q.; Sun, X.; McBreen, J. New Findings on the Phase Transitions in $\text{Li}_{1-x}\text{NiO}_2$: In Situ Synchrotron X-Ray Diffraction Studies. *Electrochem. commun.* **1999**, *1* (6), 227–232.
 25. Whittingham, M. S. Lithium Batteries and Cathode Materials. *Chem. Rev.* **2004**, *104* (10), 4271–4301.
 26. Thackeray, M. M. Manganese Oxides for Lithium Batteries. *Prog. Solid State Chem.* **1997**, *25* (1–2), 1–71.
 27. Li, H.; Zhang, N.; Li, J.; Dahn, J. R. Updating the Structure and Electrochemistry of Li_xNiO_2 for $0 \leq x \leq 1$. *J. Electrochem. Soc.* **2018**, *165* (13), A2985–A2993.
 28. Delmas, C.; Ménétrier, M.; Croguennec, L.; Levasseur, S.; Pérès, J. P.; Pouillier, C.; Prado, G.; Fournès, L.; Weill, F. Lithium Batteries: A New Tool in Solid State Chemistry. *Int. J. Inorg. Mater.* **1999**, *1* (1), 11–19.
 29. Li, W.; Reimers, J. N.; Dahn, J. R. In Situ X-Ray Diffraction and Electrochemical Studies of $\text{Li}_{1-x}\text{NiO}_2$. *Solid State Ionics* **1993**, *67* (1–2), 123–130.
 30. Dokko, K.; Nishizawa, M.; Horikoshi, S.; Itoh, T.; Mohamedi, M.; Uchida, I. In Situ Observation of LiNiO_2 Single-Particle Fracture during Li-Ion Extraction and Insertion. *Electrochem. Solid-State Lett.* **2000**, *3* (3), 125–127.
 31. Li, H.; Hua, W.; Liu-Théato, X.; Fu, Q.; Desmau, M.; Missyul, A.; Knapp, M.; Ehrenberg, H.; Indris, S. New Insights into Lithium Hopping and Ordering in LiNiO_2 Cathodes during Li (De)Intercalation. *Chem. Mater.* **2021**, *33* (24), 9546–9559.

32. Arroyo Y De Dompablo, M. E.; Ceder, G. On the Origin of the Monoclinic Distortion in Li_xNiO_2 . *Chem. Mater.* **2003**, *15* (1), 63–67.
33. Whitfield, P. S.; Davidson, I. J.; Cranswick, L. M. D.; Swainson, I. P.; Stephens, P. W. Investigation of Possible Superstructure and Cation Disorder in the Lithium Battery Cathode Material $\text{LiMn}_{1/3}\text{Ni}_{1/3}\text{Co}_{1/3}\text{O}_2$ Using Neutron and Anomalous Dispersion Powder Diffraction. *Solid State Ionics* **2005**, *176* (5–6), 463–471.
34. Liu, H.; Liu, H.; Seymour, I. D.; Chernova, N.; Wiaderek, K. M.; Trease, N. M.; Hy, S.; Chen, Y.; An, K.; Zhang, M.; Borkiewicz, O. J.; Lapidus, S. H.; Qiu, B.; Xia, Y.; Liu, Z.; Chupas, P. J.; Chapman, K. W.; Whittingham, M. S.; Grey, C. P.; Meng, Y. S. Identifying the Chemical and Structural Irreversibility in $\text{LiNi}_{0.8}\text{Co}_{0.15}\text{Al}_{0.05}\text{O}_{2-a}$ Model Compound for Classical Layered Intercalation. *J. Mater. Chem. A* **2018**, *6* (9), 4189–4198.
35. Friedrich, F.; Strehle, B.; Freiberg, A. T. S.; Kleiner, K.; Day, S. J.; Erk, C.; Piana, M.; Gasteiger, H. A. Capacity Fading Mechanisms of NCM-811 Cathodes in Lithium-Ion Batteries Studied by X-Ray Diffraction and Other Diagnostics. *J. Electrochem. Soc.* **2019**, *166* (15), A3760.
36. Mock, M.; Bianchini, M.; Fauth, F.; Albe, K.; Sicolo, S. Atomistic Understanding of the LiNiO_2 – NiO_2 Phase Diagram from Experimentally Guided Lattice Models. *J. Mater. Chem. A* **2021**, *9* (26), 14928–14940.
37. Dahn, J. R.; von Sacken, U.; Michal, C. A. Structure and Electrochemistry of $\text{Li}_{1-y}\text{NiO}_2$ and a New Li_2NiO_2 Phase with the $\text{Ni}(\text{OH})_2$ Structure. *Solid State Ionics* **1990**, *44* (1–2), 87–97.
38. Van Der Ven, A.; Thomas, J. C.; Xu, Q.; Swoboda, B.; Morgan, D. Nondilute Diffusion from First Principles: Li Diffusion in Li_xTiS_2 . *Phys. Rev. B - Condens. Matter Mater. Phys.* **2008**, *78* (10), 104306.
39. Van Der Ven, A.; Ceder, G. Lithium Diffusion in Layered Li_xCoO_2 . *Electrochem. Solid-State Lett.* **2000**, *3* (7), 301–304.
40. Kang, K.; Ceder, G. Factors That Affect Li Mobility in Layered Lithium Transition Metal Oxides. *Phys. Rev. B - Condens. Matter Mater. Phys.* **2006**, *74* (9), 094105.
41. Bianchini, M.; Fauth, F.; Hartmann, P.; Brezesinski, T.; Janek, J. An in Situ Structural Study on the Synthesis and Decomposition of LiNiO_2 . *J. Mater. Chem. A* **2020**, *8* (4), 1808–1820.
42. Goodenough, J. B.; Wickham, D. G.; Croft, W. J. Some Magnetic and Crystallographic Properties of the System $\text{Li}_{1+x}\text{Ni}_{1-x}\text{O}$. *J. Phys. Chem. Solids* **1958**, *5* (1–2), 107–116.
43. Shannon, R. D. Revised Effective Ionic Radii and Systematic Studies of Interatomic Distances in Halides and Chalcogenides. *acta crystallographica Sect. A* **1976**, *32* (5), 751–767.
44. Yamada, S.; Fujiwara, M.; Kanda, M. Synthesis and Properties of LiNiO_2 as Cathode Material for Secondary Batteries. *J. Power Sources* **1995**, *54* (2), 209–213.
45. Delmas, C.; Ménétrier, M.; Croguennec, L.; Saadoune, I.; Rougier, A.; Pouillier, C.; Prado, G.; Grune, M.; Fournes, L. An Overview of the $\text{Li}(\text{Ni},\text{M})\text{O}_2$ Systems: Syntheses, Structures and Properties. *Electrochim. Acta* **1999**, *45* (1–2), 243–253.

46. Lin, S. P.; Fung, K. Z.; Hon, Y. M.; Hon, M. H. Crystallization Kinetics and Mechanism of the $\text{Li}_x\text{Ni}_{2-x}\text{O}_2$ ($0 < x \leq 1$) from Li_2CO_3 and NiO. *J. Cryst. Growth* **2002**, *234* (1), 176–183.
47. Kim, U. H.; Jun, D. W.; Park, K. J.; Zhang, Q.; Kaghazchi, P.; Aurbach, D.; Major, D. T.; Goobes, G.; Dixit, M.; Leifer, N.; Wang, C. M.; Yan, P.; Ahn, D.; Kim, K. H.; Yoon, C. S.; Sun, Y. K. Pushing the Limit of Layered Transition Metal Oxide Cathodes for High-Energy Density Rechargeable Li Ion Batteries. *Energy Environ. Sci.* **2018**, *11* (5), 1271–1279.
48. Chang, C. C.; Scarr, N.; Kumta, R. N. Synthesis and Electrochemical Characterization of LiMO_2 (M=Ni, $\text{Ni}_{0.75}\text{Co}_{0.25}$) for Rechargeable Lithium Ion Batteries. *Solid State Ionics* **1998**, *112* (3–4), 329–344.
49. Kalaiselvi, N.; Raajaraajan, A. V.; Sivagaminathan, B.; Renganathan, N. G.; Muniyandi, N.; Ragavan, M. Synthesis of Optimized LiNiO_2 for Lithium Ion Batteries. *Ionics (Kiel)*. **2003**, *9* (5), 382–387.
50. Song, M. Y.; Kwon, I. H.; Park, H. R.; Mumm, D. R. Electrochemical Properties of Lithium Nickel Oxide Synthesized by the Combustion Method in an O_2 Stream. *Ceram. Int.* **2012**, *38* (3), 2443–2448.
51. McCalla, E.; Carey, G. H.; Dahn, J. R. Lithium Loss Mechanisms during Synthesis of Layered $\text{Li}_x\text{Ni}_{2-x}\text{O}_2$ for Lithium Ion Batteries. *Solid State Ionics* **2012**, *219*, 11–19.
52. Blomgren, G. E. The Development and Future of Lithium Ion Batteries. *J. Electrochem. Soc.* **2017**, *164* (1), A5019–A5025.
53. Myung, S. T.; Maglia, F.; Park, K. J.; Yoon, C. S.; Lamp, P.; Kim, S. J.; Sun, Y. K. Nickel-Rich Layered Cathode Materials for Automotive Lithium-Ion Batteries: Achievements and Perspectives. *ACS Energy Lett.* **2017**, *2* (1), 196–223.
54. Yoon, C. S.; Kim, U. H.; Park, G. T.; Kim, S. J.; Kim, K. H.; Kim, J.; Sun, Y. K. Self-Passivation of a LiNiO_2 Cathode for a Lithium-Ion Battery through Zr Doping. *ACS Energy Lett.* **2018**, *3* (7), 1634–1639.
55. Keeler, J. *Understanding NMR Spectroscopy*; John Wiley and Sons, Chichester, 1st edition, 2015.
56. Duer, M. J. *Introduction to Solid-State NMR Spectroscopy*; Blackwell publishing, Oxford, 2004.
57. Kurland, R. J.; McGarvey, B. R. Isotropic NMR Shifts in Transition Metal Complexes: The Calculation of the Fermi Contact and Pseudocontact Terms. *J. Magn. Reson.* **1970**, *2* (3), 286–301.
58. Bertini, I.; Luchinat, C.; Parigi, G. Magnetic Susceptibility in Paramagnetic NMR. *Prog. Nucl. Magn. Reson. Spectrosc.* **2002**, *40*, 249–273.
59. Delmas, C.; Carlier, D.; Ceder, G.; Ménétrier, M.; Grey, C. P. Understanding the NMR Shifts in Paramagnetic Transition Metal Oxides Using Density Functional Theory Calculations. *Phys. Rev. B* **2003**, *67* (17), 174103.
60. Lee, Y. J.; Wang, F.; Grey, C. P. ^6Li and ^7Li MAS NMR Studies of Lithium Manganate Cathode Materials. *J. Am. Chem. Soc.* **1998**, *120* (48), 12601–12613.
61. Grey, C. P.; Dupré, N. NMR Studies of Cathode Materials for Lithium-Ion

- Rechargeable Batteries. *Chem. Rev.* **2004**, *104* (10), 4493–4512.
62. Middlemiss, D. S.; Ilott, A. J.; Clément, R. J.; Strobridge, F. C.; Grey, C. P. Density Functional Theory-Based Bond Pathway Decompositions of Hyperfine Shifts: Equipping Solid-State NMR to Characterize Atomic Environments in Paramagnetic Materials. *Chem. Mater.* **2013**, *25* (9), 1723–1734.
 63. Arai, H.; Okada, S.; Ohtsuka, H.; Ichimura, M.; Yamaki, J. Characterization and Cathode Performance of $\text{Li}_{1-x}\text{Ni}_{1+x}\text{O}_2$ Prepared with the Excess Lithium Method. *Solid State Ionics* **1995**, *80* (3–4), 261–269.
 64. Peres, J. P.; Demourgues, A.; Delmas, C. Structural Investigations on $\text{Li}_{0.65-z}\text{Ni}_{1+z}\text{O}_2$ Cathode Material: XRD and EXAFS Studies. *Solid State Ionics* **1998**, *111* (1–2), 135–144.
 65. Peres, J. P.; Weill, F.; Delmas, C. Lithium/Vacancy Ordering in the Monoclinic Li_xNiO_2 ($0.50 \leq x \leq 0.75$) Solid Solution. *Solid State Ionics* **1999**, *116* (1–2), 19–27.
 66. Arroyo y de Dompablo, M. E.; Ceder, G. First-Principles Calculations on Li_xNiO_2 : Phase Stability and Monoclinic Distortion. *J. Power Sources* **2003**, *119–121*, 654–657.
 67. Arroyo y de Dompablo, M. E.; Van der Ven, A.; Ceder, G. First-Principles Calculations of Lithium Ordering and Phase Stability on Li_xNiO_2 . *Phys. Rev. B* **2002**, *66* (6), 064112.
 68. Yan, W.; Yang, S.; Huang, Y.; Yang, Y.; Guohui Yuan. A Review on Doping/Coating of Nickel-Rich Cathode Materials for Lithium-Ion Batteries. *J. Alloys Compd.* **2020**, *819*, 153048.
 69. Mu, L.; Zhang, R.; Kan, W. H.; Zhang, Y.; Li, L.; Kuai, C.; Zydlewski, B.; Rahman, M. M.; Sun, C. J.; Sainio, S.; Avdeev, M.; Nordlund, D.; Xin, H. L.; Lin, F. Dopant Distribution in Co-Free High-Energy Layered Cathode Materials. *Chem. Mater.* **2019**, *31* (23), 9769–9776.
 70. Peres, J. P.; Weill, F.; Delmas, C. Lithium/Vacancy Ordering in the Monoclinic Li_xNiO_2 ($0.50 \leq x \leq 0.75$) Solid Solution. *Solid State Ionics* **1999**, *116* (1–2), 19–27.
 71. Marks, T.; Trussler, S.; Smith, A. J.; Xiong, D.; Dahn, J. R. A Guide to Li-Ion Coin-Cell Electrode Making for Academic Researchers. *J. Electrochem. Soc.* **2011**, *158* (1), A51.
 72. Bielecki, A.; Burum, D. P. Temperature Dependence of ^{207}Pb MAS Spectra of Solid Lead Nitrate. An Accurate, Sensitive Thermometer for Variable-Temperature MAS. *J. Magn. Reson. Ser. A* **1995**, *116* (2), 215–220.
 73. Herklotz, M.; Weiß, J.; Ahrens, E.; Yavuz, M.; Mereacre, L.; Kiziltas-Yavuz, N.; Dräger, C.; Ehrenberg, H.; Eckert, J.; Fauth, F.; Giebeler, L.; Knapp, M. A Novel High-Throughput Setup for in Situ Powder Diffraction on Coin Cell Batteries. *J. Appl. Crystallogr.* **2016**, *49* (1), 340–345.
 74. Verma, A.; Smith, K.; Santhanagopalan, S.; Abraham, D.; Yao, K. P.; Mukherjee, P. P. Galvanostatic Intermittent Titration and Performance Based Analysis of $\text{LiNi}_{0.5}\text{Co}_{0.2}\text{Mn}_{0.3}\text{O}_2$ Cathode. *J. Electrochem. Soc.* **2017**, *164* (13), A3380–A3392.
 75. Märker, K.; Reeves, P. J.; Xu, C.; Griffith, K. J.; Grey, C. P. Evolution of Structure and Lithium Dynamics in $\text{LiNi}_{0.8}\text{Mn}_{0.1}\text{Co}_{0.1}\text{O}_2$ (NMC811) Cathodes during Electrochemical Cycling. *Chem. Mater.* **2019**, *31* (7), 2545–2554.

76. Peres, J. P.; Delmas, C.; Rougier, A.; Broussely, M.; Pertion, F.; Biensan, P.; Willmann, P. The Relationship between the Composition of Lithium Nickel Oxide and the Loss of Reversibility during the First Cycle. *J. Phys. Chem. Solids* **1996**, *57* (6–8), 1057–1060.
77. Arai, H.; Okada, S.; Ohtsuka, H.; Ichimura, M.; Yamaki, J. Characterization and Cathode Performance of $\text{Li}_{1-x}\text{Ni}_{1+x}\text{O}_2$ Prepared with the Excess Lithium Method. *Solid State Ionics* **1995**, *80* (3–4), 261–269.
78. Chazel, C.; Ménétrier, M.; Croguennec, L.; Delmas, C. Coupled Ion/Electron Hopping in Li_xNiO_2 : A ^7Li NMR Study. *Inorg. Chem.* **2006**, *45* (3), 1184–1191.
79. Ohzuku, T.; Ueda, A.; Nagayama, M. Electrochemistry and Structural Chemistry of LiNiO_2 (R-3m) for 4 Volt Secondary Lithium Cells. *J. Electrochem. Soc.* **1993**, *140* (7), 1862–1870.
80. Yoon, C. S.; Jun, D. W.; Myung, S. T.; Sun, Y. K. Structural Stability of LiNiO_2 Cycled above 4.2 V. *ACS Energy Lett.* **2017**, *2* (5), 1150–1155.
81. de Biasi, L.; Schiele, A.; Roca-Ayats, M.; Garcia, G.; Brezesinski, T.; Hartmann, P.; Janek, J. Phase Transformation Behavior and Stability of LiNiO_2 Cathode Material for Li-Ion Batteries Obtained from In Situ Gas Analysis and Operando X-Ray Diffraction. *ChemSusChem* **2019**, *12* (10), 2240–2250.
82. Yoon, C. S.; Jun, D. W.; Myung, S. T.; Sun, Y. K. Structural Stability of LiNiO_2 Cycled above 4.2V. *ACS Energy Lett.* **2017**, *2* (5), 1150–1155.
83. Grenier, A.; Reeves, P. J.; Liu, H.; Seymour, I. D.; Märker, K.; Wiaderek, K. M.; Chupas, P. J.; Grey, C. P.; Chapman, K. W. Intrinsic Kinetic Limitations in Substituted Lithium-Layered Transition-Metal Oxide Electrodes. *J. Am. Chem. Soc.* **2020**, *142* (15), 7001–7011.
84. Carlier, D.; Ménétrier, M.; Delmas, C. ^7Li MAS NMR Study of Electrochemically Deintercalated $\text{Li}_x\text{Ni}_{0.30}\text{Co}_{0.70}\text{O}_2$ Phases: Evidence of Electronic and Ionic Mobility, and Redox Processes. *J. Mater. Chem.* **2001**, *11* (2), 594–603.
85. Chazel, C.; Ménétrier, M.; Croguennec, L.; Delmas, C. $^{6,7}\text{Li}$ NMR Study of the $\text{Li}_{1-z}\text{Ni}_{1+z}\text{O}_2$ Phases. *Magn. Reson. Chem.* **2005**, *43* (10), 849–857.
86. Chen, Z.; Lu, Z.; Dahn, J. R. Staging Phase Transitions in Li_xCoO_2 . *J. Electrochem. Soc.* **2002**, *149* (12), A1604.
87. Croguennec, L.; Pouillier, C.; Mansour, A. N.; Delmas, C. Structural Characterisation of the Highly Deintercalated $\text{Li}_x\text{Ni}_{1.02}\text{O}_2$ Phases (with $X \leq 0.30$). *J. Mater. Chem.* **2001**, *11* (1), 131–141.
88. Yang, J.; Xia, Y. Suppressing the Phase Transition of the Layered Ni-Rich Oxide Cathode during High-Voltage Cycling by Introducing Low-Content Li_2MnO_3 . *ACS Appl. Mater. Interfaces* **2016**, *8* (2), 1297–1308.
89. Schweikert, N.; Hofmann, A.; Schulz, M.; Scheuermann, M.; Boles, S. T.; Hanemann, T.; Hahn, H.; Indris, S. Suppressed Lithium Dendrite Growth in Lithium Batteries Using Ionic Liquid Electrolytes: Investigation by Electrochemical Impedance Spectroscopy, Scanning Electron Microscopy, and *in Situ* ^7Li Nuclear Magnetic Resonance Spectroscopy. *J. Power Sources* **2013**, *228*, 237–243.
90. Bhattacharyya, R.; Key, B.; Chen, H.; Best, A. S.; Hollenkamp, A. F.; Grey, C. P. In Situ NMR Observation of the Formation of Metallic Lithium Microstructures in

- Lithium Batteries. *Nat. Mater.* **2010**, 9 (6), 504–510.
91. Trease, N. M.; Köster, T. K. J.; Grey, C. P. *In Situ* NMR Studies of Lithium Ion Batteries. *Electrochem. Soc. Interface* **2011**, 20 (3), 69–73.
 92. Bianchini, M.; Schiele, A.; Schweidler, S.; Sicolo, S.; Ois Fauth, F.; Suard, E.; Indris, S.; Mazilkin, A.; Nagel, P.; Schuppler, S.; Merz, M.; Hartmann, P.; Brezesinski, T.; Rgen Janek, J. From LiNiO₂ to Li₂NiO₃: Synthesis, Structures and Electrochemical Mechanisms in Li-Rich Nickel Oxides. **2020**, 32 (21), 9211–9227.
 93. Pickering, I. J.; George, G. N.; Lewandowski, J. T.; Jacobson, A. J. Nickel K-Edge X-Ray Absorption Fine Structure of Lithium Nickel Oxides. *J. Am. Chem. Soc.* **1993**, 115 (10), 4137–4144.
 94. Liu, X.; Wang, D.; Liu, G.; Srinivasan, V.; Liu, Z.; Hussain, Z.; Yang, W. Distinct Charge Dynamics in Battery Electrodes Revealed by *in Situ* and Operando Soft X-Ray Spectroscopy. *Nat. Commun.* **2013**, 4 (1), 1–8.
 95. Mansour, A. N.; Yang, X. Q.; Sun, X.; McBreen, J.; Croguennec, L.; Delmas, C. *In Situ* X-Ray Absorption Spectroscopy Study of Li_(1-z)Ni_(1+z)O₂ (z ≤ 0.02) Cathode Material. *J. Electrochem. Soc.* **2000**, 147 (6), 2104.
 96. Shannon, R. D. Revised Effective Ionic Radii and Systematic Studies of Interatomic Distances in Halides and Chalcogenides. *Acta Cryst* **1976**, 32, 751.
 97. Kang, K.; Ceder, G. Factors That Affect Li Mobility in Layered Lithium Transition Metal Oxides. *Phys. Rev. B* **2006**, 74 (9), 094105.
 98. Kalyani, P.; Kalaiselvi, N. Various Aspects of LiNiO₂ Chemistry: A Review. *Sci. Technol. Adv. Mater.* **2005**, 6 (6), 689–703.
 99. Das, H.; Urban, A.; Huang, W.; Ceder, G. First-Principles Simulation of the (Li-Ni-Vacancy)O Phase Diagram and Its Relevance for the Surface Phases in Ni-Rich Li-Ion Cathode Materials. *Chem. Mater.* **2017**, 29 (18), 7840–7851.
 100. Dahn, J. R.; Fuller, E. W.; Obrovac, M.; von Sacken, U. Thermal Stability of Li_xCoO₂, Li_xNiO₂ and λ-MnO₂ and Consequences for the Safety of Li-Ion Cells. *Solid State Ionics* **1994**, 69 (3–4), 265–270.
 101. McCalla, E.; Carey, G. H.; Dahn, J. R. Lithium Loss Mechanisms during Synthesis of Layered Li_xNi_{2-x}O₂ for Lithium Ion Batteries. *Solid State Ionics* **2012**, 219, 11–19.
 102. Rodríguez-Carvajal, J. Recent Advances in Magnetic Structure Determination by Neutron Powder Diffraction. *Phys. B Condens. Matter* **1993**, 192 (1–2), 55–69.
 103. Dyer, L. D.; Borie, B. S.; Smith, G. P. Alkali Metal-Nickel Oxides of the Type MNiO₂. *J. Am. Chem. Soc.* **1954**, 76 (6), 1499–1503.
 104. Liu, H.; Yang, Y.; Zhang, J. Reaction Mechanism and Kinetics of Lithium Ion Battery Cathode Material LiNiO₂ with CO₂. *J. Power Sources* **2007**, 173 (1), 556–561.
 105. Kim, J. W.; Lee, H. G. Thermal and Carbothermic Decomposition of Na₂CO₃ and Li₂CO₃. *Metall. Mater. Trans. B 2001 321* **2001**, 32 (1), 17–24.
 106. Grenier, A.; Reeves, P. J.; Liu, H.; Seymour, I. D.; Märker, K.; Wiaderek, K. M.; Chupas, P. J.; Grey, C. P.; Chapman, K. W. Intrinsic Kinetic Limitations in Substituted Lithium-Layered Transition-Metal Oxide Electrodes. *J. Am. Chem. Soc.* **2020**, 142 (15), 7001–7011.

107. Srinivasan, G.; Seehra, M. S. Magnetic Susceptibilities, Their Temperature Variation, and Exchange Constants of NiO. *Phys. Rev. B* **1984**, *29* (11), 6295–6298.
108. Shirakami, T.; Takematsu, M.; Hirano, A.; Kanno, R. Spin Glass-like Magnetic Properties of LiNiO₂. *Mater. Sci. Eng. B* **1998**, *54* (1–2), 70–72.
109. Shimomura, Y.; Kojima, M.; Saito, S. Crystal Structure of Ferromagnetic Nickel Oxide. *J. Phys. Soc. Japan* **1956**, *11* (11), 1136–1146.
110. Sugiyama, J.; Ikedo, Y.; Mukai, K.; Nozaki, H.; Månsson, M.; Ofer, O.; Harada, M.; Kamazawa, K.; Miyake, Y.; Brewer, J. H.; Ansaldo, E. J.; Chow, K. H.; Watanabe, I.; Ohzuku, T. Low-Temperature Magnetic Properties and High-Temperature Diffusive Behavior of LiNiO₂. *Phys. Rev. B* **2010**, *82* (22), 224412.
111. Julien, C. M.; Ait-Salah, A.; Mauger, A.; Gendron, F. Magnetic Properties of Lithium Intercalation Compounds. *Ionics (Kiel)*. **2006**, *12* (1), 21–32.
112. Nellist, P. D. The Principles of STEM Imaging. *Scanning Transm. Electron Microsc.* **2011**, 91–115.

Publications

Publications during PhD study:

1. **Li, H.**; Hua, W.; Liu-Théato, X.; Fu, Q.; Desmau, M.; Missyul, A.; Knapp, M.; Ehrenberg, H.; Indris, S. New Insights into Lithium Hopping and Ordering in LiNiO₂ Cathodes during Li (De)Intercalation. *Chem. Mater.* **2021**, 33 (24), 9546–9559.
2. Liu-Théato, X.; Indris, S.; Hua, W.; **Li, H.**; Knapp, M.; Melinte, G.; Ehrenberg, H. Self-Standing, Collector-Free Maricite NaFePO₄/Carbon Nanofiber Cathode Endowed with Increasing Electrochemical Activity. *Energy and Fuels* **2021**, 35 (22), 18768–18777.
3. Hua, W.; Wang, S.; Wang, K.; Missyul, A.; Fu, Q.; Dewi Darma, M. S.; **Li, H.**; Baran, V.; Liu, L.; Kübel, C.; Binder, J. R.; Knapp, M.; Ehrenberg, H.; Indris, S. Li⁺/Na⁺ Ion Exchange in Layered Na_{2/3}(Ni_{0.25}Mn_{0.75})O₂: A Simple and Fast Way to Synthesize O3/O2-Type Layered Oxides. *Chem. Mater.* **2021**, 33 (14), 5606–5617.

Previous Publications during master study:

1. **Li, H.**; Zhou, P.; Liu, F.; Li, H.; Cheng, F.; Chen, J. Stabilizing Nickel-Rich Layered Oxide Cathodes by Magnesium Doping for Rechargeable Lithium-Ion Batteries. *Chem. Sci.* **2019**, 10 (5), 1374–1379.
2. Zhang, Y.; **Li, H.**; Liu, J.; Liu, J.; Ma, H.; Cheng, F. Enhancing LiNiO₂ Cathode Materials by Concentration-Gradient Yttrium Modification for Rechargeable Lithium-Ion Batteries. *J. Energy Chem.* **2021**, 63, 312–319.
3. Zhang, Y.; **Li, H.**; Liu, J.; Zhang, J.; Cheng, F.; Chen, J. LiNi_{0.90}Co_{0.07}Mg_{0.03}O₂ Cathode Materials with Mg-Concentration Gradient for Rechargeable Lithium-Ion Batteries. *J. Mater. Chem. A* **2019**, 7 (36), 20958–20964.
4. Cui, H.; **Li, H.**; Liu, J.; Zhang, Y.; Cheng, F.; Chen, J. Surface Modification of Li-Rich Manganese-Based Cathode Materials by Chemical Etching. *Inorg. Chem. Front.* **2019**, 6 (7), 1694–1700.
5. Chen, X.; Wang, L.; **Li, H.**; Cheng, F.; Chen, J. Porous V₂O₅ Nanofibers as Cathode Materials for Rechargeable Aqueous Zinc-Ion Batteries. *J. Energy Chem.* **2019**, 38, 20–25.